Bringing Near-Field Scanning Microwave Microscopy into the Quantum Regime

By

Shaun Geaney

Department of Physics
Royal Holloway, University of London

This dissertation is submitted for the degree of
Doctor of Philosophy

September, 2019

To my Nana,

who sadly passed during the writing of this work.

Declaration

I, Shaun Geaney, hereby declare that this thesis and the work presented in it is entirely my own. Where I have consulted the work of others, this is clearly stated.

Shaun Geaney

September, 2019

Acknowledgements

First of all, I would like to thank my supervisor, Dr. Sebastian de Graaf, for his excellent support, sharing his knowledge and, most importantly, teaching me the most valuable lesson that any postgraduate in experimental physics can learn in the lab: if something doesn't work, first check that it is turned on.

I would also like to thank my other supervisors, Prof. Alexander Tzalenchuk and Prof. Phil Meeson, who always challenged me and gave excellent suggestions and guidance during my research and thesis write-up.

A huge thank you to Tobias Lindström, Jonathan Burnett, Teresa Hönigl-Decrinis and David Cox for answering my questions, giving advice and fabricating my samples or FIB etching my resonator probes.

I would also like to give a big thank you to Mariam for spending her valuable and precious lunchtime with me and for the great laughs and chats we had. Another big thank you to Ailsa, who showed me the true value of sneaking off for a tea or coffee in the afternoon to 'clear the mind'. More big thanks also deserve to go to Minal, Chloe, Connor, Ilana, Kavya, Rob and John.

To my mum and family, despite saying that you weren't sure what it is that I was doing, you still supported me all the way through. Thank you!

Another massive thank you too, in no particular order: Wambler, Ste, Kenny, Tikhoze, Nikhita, Alistair, Joe, Beth, Mike, Richard, Jody, Camila, Jack, George, Will, Patrick, Josh, Elly, Reuben, Rachel, Laura, Claire, Laurence, Phil, Ryan and Sam. For all the fun PhD-distracting times and many pints at the pub, cheers! Let us have more great times together!

Finally a big thanks to Lizzie for putting up with me during the stressful writing and viva-prep times and, most importantly, making me some absolutely cracking scran throughout when I didn't have the time. Thank you!

Abstract

Near-field scanning microwave microscopy (NSMM) is a widely used scanning probe microscopy (SPM) technique. It can non-intrusively probe the material properties of a sample at the nano-scale using microwave frequency radiation. The rapid development of nanotechnology, materials and surface science underpinned by scanning probe techniques drives the demand for ever more versatile and non-invasive nano-scale analysis tools. Specifically, the development of solid-state quantum technologies has created a need for nano-scale measurement techniques that operate in the same regime as these quantum devices. However, there are very few nano-scale characterisation tools that are capable of quantum coherent interaction with samples. In particular, all NSMMs so far operate in the 'classical' regime, at high powers. To reach the quantum limit for NSMM we require (i) temperatures that are lower than the photon energy, $k_bT \ll \hbar\omega$ and (ii) ultra-low power such that the average photon number $\langle n \rangle \sim 1$, as is necessary for coherent interaction with a quantum system without saturating it.

This work presents an ultra-low power cryogenic NSMM integrated with an atomic force microscope (AFM), to enable precise distance control. A high-quality 6 GHz superconducting resonator is used as the microwave probe. This resonator is micro-machined so that it also forms the scanning tip of the AFM. We show that the microscope is capable of obtaining nano-scale dielectric contrast down to the single microwave photon regime, up to 10^9 times lower power than in typical NSMMs. The microscope was designed in-house in a dilution refrigerator operating at 10 mK with a customised suspension system to minimise the effects of external mechanical vibrations. In this thesis, we evaluate the performance of this NSMM. We also discuss the remaining challenges towards developing an NSMM capable of quantum coherent interaction, an enabling tool for the development of quantum technologies in the microwave regime.

Contents

List of Figures

List of Tables

List of Abbreviations

AC	—	Alternating current
AFM	—	Atomic force microscopy
BCS	—	Bardeen-Cooper-Schrieffer (theory)
CPB	—	Cooper pair box
CPW	—	Coplanar waveguide
CuBe	—	Copper-beryllium
DAQ	—	Data acquisition
DC	—	Direct current
DR	—	Dilution refrigerator
FIB	—	Focused ion beam
FM	—	Frequency modulation
GTM	—	General tunnelling model
HEMT	—	High-electron-mobility transistor
LC	—	Inductor-capacitor (circuit)
LHe	—	Liquid helium
LN2	—	Liquid nitrogen
MIKD	—	Microwave kinetic inductance detector
NIST	—	National Institute of Standards and Technology
NPL	—	National Physical Laboratory
NSMM	—	Near-field scanning microwave microscope
PCB	—	Printed circuit board
PDH	—	Pound-Drever-Hall (locking)
PID	—	Proportional-integral-derivative (controller)
PLL	—	Phase-locked loop
PM	—	Phase modulation
PSD	—	Power spectral density
PT	—	Pulse tube
QED	—	Quantum electrodynamics
RLC	—	Resistor-inductor-capacitor (circuit)
RWA	—	Rotating wave approximation
STEM	—	Scanning tunnelling electron microscope
SEM	—	Scanning electron microscope
SNR	—	Signal-to-noise ratio
SPM	—	Scanning probe microscopy
SQUID	—	Superconducting quantum interference device
STM	—	Standard tunnelling model
TLS	—	Two-level system
VCO	—	Voltage controlled oscillator
VNA	—	Vector network analyser
YAG	—	Yttrium-aluminium-garnet
YBCO	—	Yttrium-barium-copper-oxide
YIG	—	Yttrium-iron-garnet (filter)

Chapter 1

Introduction

Quantum technologies have progressed rapidly over the past few years. Many governments, large businesses and start-ups have invested heavily in the development and commercialisation of these technologies. Quantum technologies make use of phenomena that exploit quantum mechanical effects such as superposition of quantum states, quantum tunnelling and quantum entanglement. The use cases of quantum technologies include quantum key distribution for secure private communication between two users [1]; the use of highly accurate atomic clocks as sensitive gravimeters is another area of research and investment [2]; arguably the most publicised application of quantum technologies is quantum computing.

Certain tasks or problems can be significantly sped up with the use of quantum computers [3]. For example, Shor's algorithm [4] has the potential, in the long-term, to crack encryption protocols that rely on the difficulty of factorising large prime numbers. Even in the short-term quantum computing is being applied to medicine for the discovery of new pharmaceutical drugs [5] and to solve optimisation problems that are infeasible on a classical computer [6]. Looking at these examples, it is easy to see why the development of quantum computing is of great research and industrial interest. Although quantum processors currently exist, they possess a relatively small number of quantum bits, or 'qubits', and so do not currently possess the computing power to attempt these problems. A truly large-scale quantum computer is needed to perform such tasks and to be able to reliably out-perform classical computers. How does one implement such a quantum computer? There are multiple examples of implementations of qubits such as using the left or right circularly polarised states of a photon, strings of trapped ions, doped solid-state devices and quantum dots [3]. As well as these, and more pertinent to this thesis, superconducting qubits have also shown great promise. Companies such as Google [7], IBM [8] and Rigetti Computing [9] are all

working on developing superconducting quantum processors. One advantage with superconducting qubits is that they form a macroscopic quantum state whereby the qubit parameters are dictated by macroscopically measured quantities such as capacitance and inductance of a superconducting circuit. Fabricating superconducting qubits can be done using well-known lithographic techniques for patterning superconducting materials onto a substrate. These properties are exploited to create a solid-state superconducting quantum processor. Each implementation of a qubit has their advantages and disadvantages, usually linked with coupling multiple qubits together or fragile qubit states that are particularly vulnerable to decoherence. If a quantum computer is to successfully be constructed, it needs to (i) be a scalable physical system with well-characterised qubits and (ii) have qubits with long relevant coherence times [10].

Current superconducting quantum processor architectures are difficult to scale, leading to decoherence and dephasing of the qubits. This loss of information has been attributed to qubits coupling to uncontrolled degrees of freedom in their environment [11]. Other works have found that this decoherence mainly originates from coupling to defects that exist in the materials used to fabricate superconducting qubits. These defects behave as quantum two-level systems (TLS) with randomly fluctuating transition energies. They are a significant source of loss and contribute to noise in superconducting circuits [12]. These TLS defects have been extensively studied but their origin remains unknown. The behaviour of ensembles of material TLS defects, and their contribution to $1/f$ noise, have been measured and individual TLS defects can be coupled to using a qubit or a superconducting resonator. However, their exact location cannot be determined nor their atomic origin [13]. Individual superconducting qubits have been developed to have relatively long coherence times, but scaling up the number of qubits and coupling them together reduces the overall coherence time of the coupled system. Even for systems of coupled qubits with relatively long coherence times, the random fluctuations in TLS energy cause fluctuations in coherence times and excitation energy in otherwise 'good' qubit systems. It is, therefore, necessary to locate and identify the origin and locations of these material TLS defects to achieve long and stable coherence times for a robust universal quantum computer.

To gain further information and improve the coherence times of qubits we need

a tool that can coherently couple to and locate individual defects. Despite the increase in research amongst academia and industry to develop quantum technologies, the availability of such tools for coherent materials characterisation of quantum circuits remains limited. Specifically for superconducting quantum circuits, such a tool would need to operate in the microwave domain as the typical transition frequency of superconducting qubits is of the order of gigahertz. The tool would need to be non-invasive so that it does not damage or destroy a sample under test. It is the lack of this necessary diagnostic technology that motivates the need for a novel microscope that can coherently couple to quantum systems. Near-field scanning microwave microscopy (NSMM) is a well-established classical technique that lends itself to this purpose.

The overall aim of this project is to design an NSMM that will be capable of reaching the quantum regime. The microscope will employ techniques that non-intrusively probe dielectric samples containing quantum two-level systems at the nano-scale using microwave frequency photons. A classical NSMM typically consists of an atomic force microscopy (AFM) component used to obtain the topography of the sample, and to maintain a constant tip-sample separation as is required for the microwave readout. Once positioned above the material, the NSMM tip will transmit a pulsed or continuous microwave signal. The tip itself can function as a transmission-detection microwave antenna or just as a transmitter, together with a separate detector to receive the reflected microwaves. The microwave signal will interact with the sample causing changes in the amplitude, frequency and phase of the microwave signal to yield information about the conductivity, polarisation and dielectric constant of the material [14, 15]. The primary aim of this project is to extend this classical idea of the NSMM technique and bring it to the quantum limit. In the quantum limit, we can use the NSMM to study qubits and, more importantly, individual TLS defects, at the nanoscale.

To be able to achieve the goal of an NSMM that can coherently couple to individual quantum systems, some significant challenges will need to be overcome. In this thesis, we aim to address some of these challenges. Firstly, the resonator must be operated at sufficiently low powers such that, on average, only a single photon occupies the resonator probe ($\langle n \rangle \sim 1$). This ensures that an ensemble of material TLS defects are not saturated by large numbers of photons and increases the

likelihood of coherently coupling to an individual material TLS defect. Secondly, the NSMM must operate at ultra-low temperatures, on the order of a few millikelvin. This is a requirement for coherent interactions with material TLS defects as $k_B T \ll E_{\mathrm{TLS}} \sim \hbar\omega_r$, where E_{TLS} is the energy splitting of a TLS and ω_r is the resonant frequency of the NSMM probe. This ensures minimal thermal excitation, such that the majority of material TLS defects are in their ground state. For a probe frequency of $\omega_r/2\pi = 6$ GHz, this requires that $T \ll 300$ mK. This will be achieved by placing the NSMM within a dilution refrigerator (DR), leading on to the third challenge. Nanometer-scale distance control between the probe tip and sample surface is necessary to achieve stable and coherent coupling. The NSMM must be mechanically isolated so that disturbances from external mechanical vibrations are reduced, particularly so given the choice of a BlueFors LD-400 series refrigerator that uses a pulse tube (PT) to cool to 4 K. The rotational frequency of the PT motor is a major source of external mechanical disturbance, whose effect on the experiment needs to be minimised [16]. Our solution is to suspend the NSMM on springs within the DR that will be capable of damping such external disturbances. Finally, the superconducting resonator probe must have a high-Q factor, greater than the strength of coupling between the probe and a TLS, to ensure that the probe is in the strong coupling regime and can dispersively couple to a two-level quantum system [17]. In this thesis, we achieve single photon regime scanning using a high-Q resonator and demonstrate a suspension system with mechanical stability comparable to that of state-of-the-art scanning probe microscopes.

Chapter 2

Two-Level Quantum Systems

In this chapter, we will consider the physics that describes a generic two-level quantum system. This formalism can then be applied to various examples of two-level systems that appear in the field of superconducting quantum devices research. Examples of such systems include superconducting qubits, the basic building block of a superconducting quantum computer and material two-level system (TLS) defects that are of unknown origin and exist in amorphous materials used in the fabrication of quantum circuits. We move on to discussing how these defects have a detrimental effect on superconducting quantum devices, as well as how they cause frequency noise. We discuss analysis techniques used to understand noise data and their understanding through power laws. This will be relevant to understanding results that appear later in this thesis. Throughout the rest of this thesis, we will employ the convention of using the abbreviation 'TLS' to refer to the material defects that are attributed to causing decoherence in quantum circuits and use the full terms 'two-level system' or 'two-level quantum system' when referring to a general two-level system such as a qubit.

2.1 General Two-State Quantum Systems

Any quantum system with only two distinguishable states, or where the other higher-level states are energetically far from the lowest two states, can be considered as a two-level quantum system. Any two-level system can be written as $|\psi\rangle = \alpha\,|0\rangle + \beta\,|1\rangle$, where $\{|0\rangle, |1\rangle\}$ is the set of linearly independent vectors that span the 2-dimensional Hilbert space and α and β are normalised constants. Operators in this space are 2×2 matrices where the identity matrix $\hat{I}$ and the Pauli matrices $\hat{\sigma}_{x,y,z}$ form the full basis of Hermitian operators in this space. A generic two-level quantum system can be depicted on a Bloch sphere, as shown in Fig. 2.1.

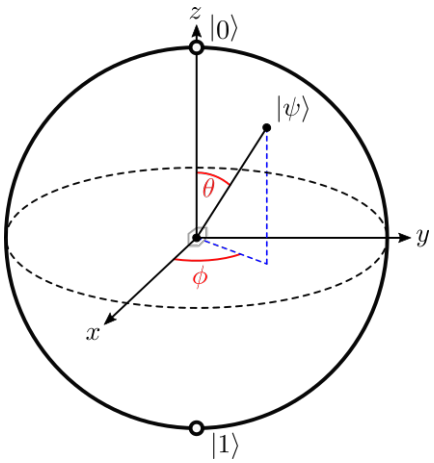

Figure 2.1: Diagram of the Bloch sphere, a geometric representation of a true two-level quantum system. This depicts the state $|\psi\rangle$ in terms of the linearly independent basis states $|0\rangle$ and $|1\rangle$ that form the full 2-dimensional space.

The angles θ and ϕ are defined in spherical polar coordinate system, such that $|\psi\rangle = \cos(\theta/2)\,|0\rangle + \sin(\theta/2)e^{i\phi}\,|1\rangle$. Operators acting on the state $|\psi\rangle$ rotate it about the Bloch sphere. Changes in the amplitude or phase of this state can be caused by interactions with the environment, leading to the decoherence of the state [18].

A two-level system can be excited with an RF pulse causing a transition from the ground to the first excited state. This assumes that the two-level system is in its ground state to begin with, which is achievable if the system is sufficiently cooled enough to a temperature significantly below the energy of the first excited state with respect to the ground state. For a typical superconducting quantum system, this means a non-isolated two-level system can interact with its environment which can cause a rotation of the state vector around the Bloch sphere. The Hamiltonian that describes an individual two-level system is given by

$$\hat{H} = -\tfrac{1}{2}(\delta E\hat{\sigma}_z + \Delta\hat{\sigma}_x), \tag{2.1}$$

where $\delta E = E_e - E_g$, the difference between the uncoupled first excited and ground states, respectively, and Δ is the coupling between the energy levels. When substituting this into the time-independent Schrödinger Equation, we get the eigenvalues $E_{1,2} = \pm\sqrt{\delta E^2 + \Delta^2}$ that correspond to the coupled energy levels. A generic

two-level sytem can have energy eigenvalues that can correspond to any value of frequency. Though typically qubits and material TLS defects will have an energy gap that corresponds to frequencies on the order of gigahertz. This means that these types of two-level quantum systems can be excited with the use of microwave photons [19].

2.2 Superconducting Qubits

In this section, we first briefly introduce superconductivity and some of its more relevant concepts to the work described in this thesis. We then introduce the necessary concepts to be able to understand some basic physics for superconducting qubits and their design. The reason for this is that later on in the thesis we discuss the design of a sample to be scanned with the NSMM that consists of qubit arrays. The idea behind this is to create a number of 'artificial' TLS defects with known parameters such as the transition frequency and the dimensions of the structure. The objective with this sample is to attempt a scan in the single photon regime while coherently coupling to one of the qubits in the array. This would provide proof of concept of using NSMM for coherent interaction with a TLS in the sample, on a controlled and well defined two-level system. Once this is achieved, the NSMM can be used to search for unknown material TLS defects in a sample.

2.2.1 Superconductivity

A material is said to be in the superconducting state when, in the absence of an applied magnetic field, it exhibits two properties: perfect conductivity and perfect diamagnetism. This first means that the resistivity of the material is zero. The latter means that magnetic fields are expelled from the superconductor. This is known as the Meissner effect [20]. The superconducting state only exists below some critical temperature T_c. The Bardeen–Cooper–Schrieffer (BCS) theory has had success in describing conventional superconductivity. It is worth noting that exotic materials have been used to demonstrate high-T_c superconductivity but in this thesis, we focus on conventional superconductors. BCS Theory introduces the idea of weakly bound electron pairs with a binding energy $2\Delta \approx 3.5 k_B T_c$. The

bound electrons have equal and opposite momenta and spin and are commonly referred to as 'Cooper-pairs' [21].

An important effect, known as the Josephson effect, occurs when two superconductors are separated by a weak link or a thin electrically insulating region, known as a Josephson junction. The supercurrent I_s, and the voltage V, across such a junction are,

$$I_s = I_0 \sin(\Delta\varphi) \quad \text{and} \quad V = \frac{\hbar}{2e}\frac{\partial}{\partial t}(\Delta\varphi). \tag{2.2}$$

I_0 is a critical current parameter of the Josephson junction. Exceeding this critical current destroys the coherence across the junction. The term $\Delta\varphi$, is the phase difference of the wavefunctions of the two superconductors [22]. Josephson junctions are useful circuit elements in quantum circuits and quantum computing since they provide the necessary non-linear inductance that is needed to remove the degeneracy in the energy level splitting in superconducting qubits. This macroscopic coherence that manifests in Josephson junction circuits means that it is possible to fabricate superconducting quantum circuits using standard lithography methods. The low loss properties of superconductors are critical in the field and in the work presented in this thesis.

2.2.2 The Charge and Transmon Qubit

Broadly speaking, superconducting qubits can be categorised into three main species: the charge qubit, the flux qubit and the phase qubit. Many review articles exist discussing in detail each type of qubit [23–25], though here we are only interested in a basic understanding of the transmon - an extension to the charge qubit. One of the first experiments demonstrating a charge qubit was performed by Nakamura *et. al.* [26]. A charge qubit (see Fig. 2.2(a)) consists of a superconducting island known as a Cooper-pair box (CPB) connected to another superconducting electrode via a Josephson junction, and a gate voltage V_g, can be applied to the island via a capacitor C_g. The gate voltage 'pumps' Cooper-pairs from the superconducting island across the junction. A second Josephson junction can be added in parallel with the first to create a superconducting quantum interference device

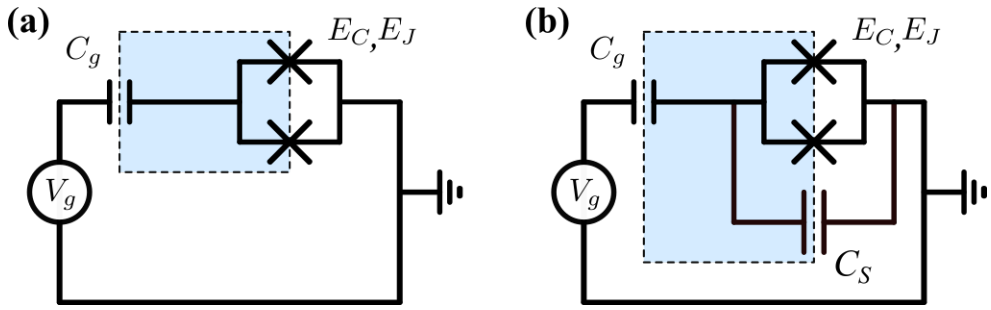

Figure 2.2: Circuit diagram for **(a)** a flux tunable charge qubit and **(b)** a flux tunable transmon qubit. The dashed blue region shows the CPB island where Cooper-pairs tunnel through the SQUID loop with Coulomb energy.

(SQUID) loop. This loop allows for the qubit transition energy to be tuned with the use of a magnetic field. Figure 2.2(a) shows a circuit diagram of a flux tunable charge qubit.

The Hamiltonian for the charge qubit system can be written in terms of two energy parameters: the Coulomb energy E_C (the electrostatic energy for a Cooper-pair), expressed as $E_C = (2e)^2/2C$, where e is the elementary charge and C is the total capacitance of the qubit circuit, including the bias capacitance, and the Josephson energy which is $E_J = I_c\Phi_0/2\pi$ where I_c is the critical current of the junction and Φ_0 is the magnetic flux quantum. The Josephson energy can also be expressed as $E_J = R_Q\Delta/2R_N$, where $R_Q = h/4e^2$ is the resistance quantum for a Cooper pair and R_N is the normal state resistance. Δ is the superconducting energy gaps as described by the BCS theory of superconductivity[1]. The Hamiltonian can then be written as

$$\hat{H} = E_C(\hat{n} - n_g)^2 - E_J \cos\hat{\phi}. \tag{2.3}$$

Here, $n_g = C_gV_g/2e$ is known as the offset gate charge of the CPB. The eigenenergies for this Hamiltonian are shown in Fig. 2.3 for differing ratios of E_J/E_C. When $n_g = N + \frac{1}{2}$, where N is an integer, the uncoupled charge states $|0\rangle$ and $|1\rangle$ are degenerate. The Josephson energy lifts this degeneracy and the resulting qubit Hamiltonian can be expressed in a form similar to that of a general TLS, as was described by Eq. (2.1). While successful and even ground-breaking as a pioneering

[1]From BCS Theory, $\Delta = 1.76k_bT_c$ where T_c is the critical temperature of the superconductor.

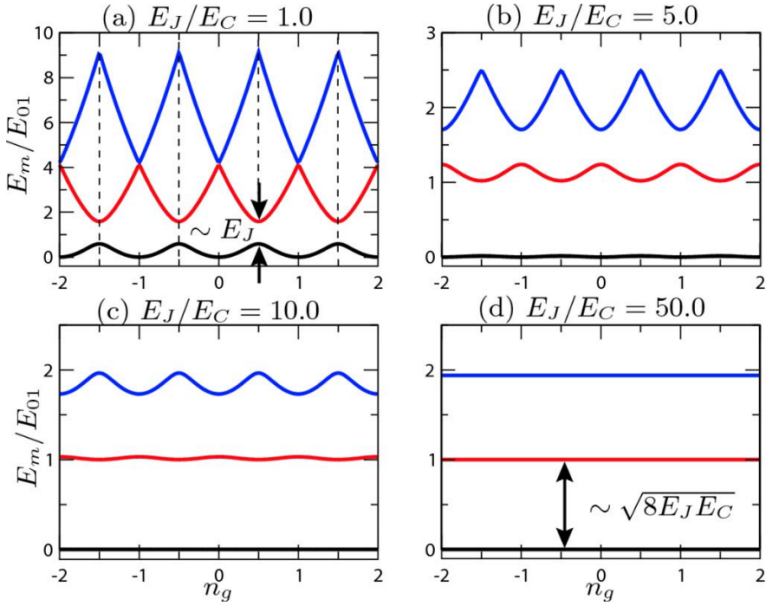

Figure 2.3: The eignenenergies E_m, for the first three levels of the transmon ($n = 0, 1, 2$) as a function of the offset charge n_g. Four different ratios of E_J/E_C are shown. The eigenenergies are normalised to the transition energy E_{01} at $n_g = \frac{1}{2}$. Adapted from [27].

demonstration of an artificial two-level quantum system is, the charge qubit suffered from sensitivity to charge fluctuations in its environment. This is caused by *e.g.* charge traps in the substrate. To alleviate this problem, several architectures were put forward, one of the most successful being the transmon design.

To create a transmon qubit, two changes need to be made to the charge qubit. One change is that an additional capacitance C_S, needs to be added that is connected via a shunted transmission line, shown in Fig. 2.2(b). The second change is that the qubit needs to operate in the so-called charge insensitive regime. This means that it must satisfy the criteria of $E_J/E_C \gg 1$. This has the effect of reducing charge noise in the qubit [27], which is a dominant form of noise. As shown in Fig. 2.3(a) for $E_J/E_C \sim 1$, when $n_g = \frac{1}{2}$, the energy bands are flat to first order, meaning that small charge fluctuations do not lead to noise in the energy level transition frequency. Though for values of n_g away from this 'sweet spot', sensitivity to charge noise is increased. However in Fig. 2.3(d) for the case where $E_J/E_C = 50$, the eigenenergies are approximately constant for changes in n_g and

thus the sensitivity to charge noise has been exponentially reduced to almost zero. However, this comes at a trade off. Flatter energy bands result in reduced anharmonicity *i.e.* the difference in transition frequency between the $|0\rangle$ and $|1\rangle$ states and the $|1\rangle$ and $|2\rangle$ states become smaller. For this reason, choosing the correct ratio of E_J/E_C has a significant impact when designing a qubit sample [28]. For a large ratio of E_J/E_C, the transition energy of the transmon can be approximated as

$$E_{01} = hf_p - E_C, \tag{2.4}$$

where f_p is the so-called Josephson plasma frequency and can be written as

$$f_p = \frac{\sqrt{8E_J E_C}}{h}. \tag{2.5}$$

This means that the choice of E_J and E_C is important in choosing a transition frequency. The choice also affects the design of the qubit as well as the fabrication process. The value of E_C is inversely proportional to the total capacitance of the qubit. This includes the value of the capacitance in the circuit as well as the capacitive contribution from the Josephson junctions. As for the fabrication, a double-angle shadow evaporation technique is used to create the Josephson junctions for the SQUID shown in Fig. 2.2. In this technique, a superconducting material, for example, aluminium, is deposited on to a mask of the design that was created using electron beam lithography. This first layer aluminium is then oxidised to create an insulating later of Al_2O_3 before another layer of aluminium is deposited. The two depositions are carried out at different angles with respect to the sample. The junctions are formed at the overlap of the two layers. The angle defines the lateral dimensions of the junction and therefore its capacitance. The pressure at which the sample is oxidised (or the duration of the oxidisation at a fixed pressure) directly affects the normal state resistance of the qubit sample and which is in turn indirectly proportional to E_J. Later on in Chapter 6 we discuss the specific parameters chosen for the charge qubit sample that we fabricate.

2.3 Material TLS Defects

As promising as superconducting qubits are to developing a robust quantum computer, some challenges need to be overcome. Like most implementations of qubits, there are still sources of dissipation, decoherence and noise in superconducting quantum circuits. The source of this loss has been widely attributed to the existence of defects that exist in superconducting quantum devices. These defects are not impurities that are introduced by the fabrication process but are due to the amorphous nature of the materials that are used in the fabrication. These defects behave as two-level quantum systems and the model often used to describe them was originally suggested to explain the behaviour of the heat capacity of glasses and similar semi-crystalline structures [30]. Despite the success of phenomenological models describing TLS, their microscopic nature in superconducting devices remains mostly unknown.

One proposal for the origin of material TLS defects has been the idea of tunnelling atoms. This idea suggests that atoms in the lattice can quantum mechanically tunnel between two energetically favourable states, creating an electric dipole. This assumes that the atoms are otherwise cooled to low enough temperature to not be thermally excited between these two states. These behaviours have been described in detail in the standard tunnelling model (STM) which is discussed next in more detail. Other theories used to describe TLS dynamics are

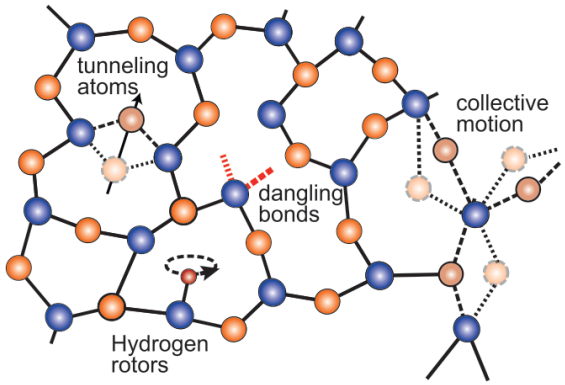

Figure 2.4: A sketch showing some of the different possible candidates for the nature of TLS defects. These include tunnelling atoms, dangling bonds, hydrogen rotors and collective motion of the lattice. Adapted from [29].

tunnelling electrons, dangling bonds of hydrogen atoms, hydrogen vacancies that lead to hydrogen rotors, and collective motion of phonons in the lattice [29]. Some of these suggested for the origin of TLS have been depicted in Fig. 2.4.

2.3.1 Standard Tunnelling Model

The theory of tunnelling material TLS defects was originally used to explain the thermal properties of glasses. The model assumes that an atom, or small group of atoms, sit in an asymmetric double-well potential and can quantum mechanically tunnel between the two semi-stable states [30–32]. The following assumptions are made for the STM for the double-well potential. They are [29]

- There are two energetically similar states for the TLS to exist in, of which it occupies one at any given time.
- These two states are modelled as two parabolic wells that are separated by a barrier.
- The TLS is at a low enough temperature such that thermal excitation over the barrier can be ignored and transitions between the two states require quantum tunnelling.
- Transitions between the two states can be induced via coupling to electric fields or by an applied strain to the amorphous solid.
- TLS defects exist in large ensembles and so can be parameterised by a distribution of barrier heights, asymmetries and eigenenergies that is approximately uniform.

A diagram of this type of potential is shown in Fig. 2.5 and is characterised by two energies: the asymmetry energy ε to describe the two different 'depths' of each well and the required tunnelling energy Δ, to tunnel through the barrier.

The Hamiltonian for the system can be written in terms of these two energies and the Pauli matrices as

$$\hat{H}_{\mathrm{TLS}} = \tfrac{1}{2}(\varepsilon\hat{\sigma}_z + \Delta\hat{\sigma}_x). \tag{2.6}$$

The eigenstates can be written in terms of the two lowest states of the potential well shown in Fig. 2.5 with $|L\rangle$ for the left state and $|R\rangle$ for the right state. Due to the tunnelling through the barrier, these states hybridise forming the new eigenstates $|\psi_+\rangle = \sin(\theta/2)\,|L\rangle + \cos(\theta/2)\,|R\rangle$ and $|\psi_-\rangle = \cos(\theta/2)\,|L\rangle - \sin(\theta/2)\,|R\rangle$, where $\tan(\theta) = \Delta/\epsilon$ is the so-called mixing angle. This yields a difference in energy between these two eigenstates *i.e.* the energy splitting of the TLS, to be

$$E = E_+ - E_- = \sqrt{\varepsilon^2 + \Delta^2}. \tag{2.7}$$

We can consider two limits to this equation. When $|\varepsilon| \ll \Delta$, the eigenstates are well described by the $|L\rangle$ and $|R\rangle$ states. Then for the case when $|\varepsilon| \approx 0$, and the double well is symmetric, there is a superposition of the $|\psi_+\rangle$ and $|\psi_-\rangle$ eigenstates.

The STM has had success in describing the low temperature, anomalous properties of amorphous solids. However, its predictions for the frequency noise does not match the data from recent experiments [34] but additions to the STM have been made to address two key assumptions. The first is that the STM assumes that there are no interactions between TLS, which, as it turns out, has an impact on the TLS relaxation times. The second assumption that is addressed is that the probability density is not uniform. This has been referred to as the so-called generalised tunnelling model (GTM). Theoretical work on the GTM is discussed

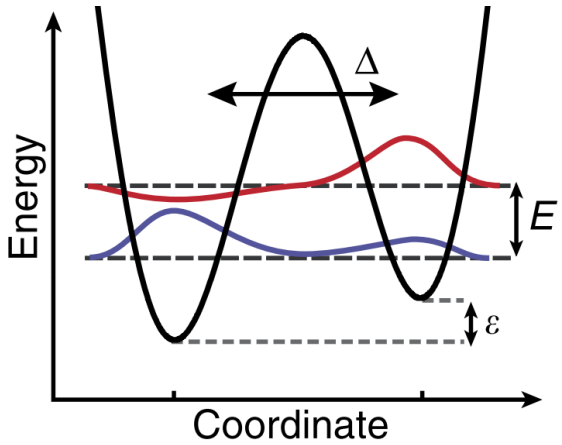

Figure 2.5: A diagram of an asymmetric double well potential. This depicts the required tunnelling energy Δ, and the asymmetry energy ε, of the double-well potential. Here, E is the energy splitting of the TLS. Adapted from [33].

in more detail in [34], where the idea of coherent and non-coherent material TLS defects, or quantum and classical respectively, are introduced.

2.3.2 Impact on Solid-State Quantum Devices

Many experiments investigating superconducting circuits or technologies in the past two decades have found sources of dielectric loss. They attribute the source of this loss to material TLS defects in dielectric materials that couple to resonance modes of the device under test. Some of the first reports of TLS defects contributing to decoherence in superconducting qubits [12, 35] showed how TLS defects in the dielectric layer of a Josephson junction contributed to an increase in the loss tangent $\tan(\delta)$, at millikelvin temperatures. Further studies have shown how material TLS defects affect the coherence times of qubits [36] and the varying time-scales of the material TLS defects lifetimes.

TLS defects have also been observed to affect superconducting microresonators. This manifests itself by causing jitter in the resonance frequency of the resonator. This is due to the 'switching' of electric dipoles as the TLS defects tunnel between two stable states, resulting in $1/f$ noise. It turns out that, when operating thin-film resonators at low temperature and low power, the STM does not fully explain their behaviour [37, 38]. The GTM modification (mentioned previously) is necessary to account for TLS-TLS defect interactions and fully describe the resonators in these regimes. Other works have identified the main source of material TLS defect loss to be due to the interface between materials [39]. For example, for a Nb coplanar waveguide (CPW) fabricated onto a Si substrate, the interface between the two materials was found to cause high levels of loss due to material TLS defects. It has also been found that treating the surfaces of resonator samples prior to metallic evaporation can reduce the dielectric loss level.

If we are to operate a superconducting resonator as an NSMM probe in the single photon regime, it is important to understand the properties of resonators at very low temperatures and low powers, and how they are affected by material TLS defects. To observe the behaviour of a superconducting resonator at low temperatures, one can track the change in its resonant frequency as a function of the temperature. The expected dependence of the resonance frequency versus

temperature is given by [40]

$$\Delta f(T) = F\tan(\delta_i)\left[\mathrm{Re}\left(\Psi\left(\tfrac{1}{2}+\tfrac{hf_0}{2\pi i k_B T}\right)+\Psi\left(\tfrac{1}{2}+\tfrac{hf_0}{2\pi i k_B T_0}\right)-\ln\left(\tfrac{T}{T_0}\right)\right)\right]. \quad (2.8)$$

Here, $\Delta f = (f(T) - f_0)/f_0$, $\Psi(x)$ is the di-gamma function and T_0 is a reference temperature, F is the so-called filling factor and $\tan(\delta_i) = \tan(\delta_0)\tanh(\hbar\omega/2k_BT)$ is the TLS loss tangent. The shift in frequency as a function of temperature is due to the broad density of states of TLS coupled to the resonator being thermally desaturated. This function gives a frequency decreasing with decreasing temperature until a minimum in frequency at $T = \hbar\omega/2k_B$, at which point the frequency starts to increase [41]. where $\omega = 2\pi \cdot f$ is the angular frequency. This 'upswing' in the frequency shift is caused by the TLS no longer being thermally saturated and can act as an extra channel of loss when thermal energies reach below the TLS transition energy. The loss of a superconducting resonator can also be observed by measuring its intrinsic quality factor Q_i, as a function of the applied power. This can be written as [42, 43]

$$Q_i^{-1} = \frac{F\tan(\delta_0)\tanh\left(\frac{\hbar\omega}{2k_BT}\right)}{\left(1+\frac{\langle n\rangle}{n_c}\right)^{\alpha}} + Q_{i,0}^{-1} \quad (2.9)$$

where $\langle n\rangle$ is the average photon number (this is proportional to the applied power to the resonator, discussed later in Section 4.1.4), n_c is the critical number of photons stored in the resonator needed to saturate one TLS from the electric field within the resonator. Other sources of loss are contained within $Q_{i,0}^{-1}$. At higher powers, all the TLS are saturated by a large number of photons in the resonator and there is a plateau in Q_i, as shown in Fig. 2.6. Equation (2.9) also shows Q_i as a function of temperature. For most experiments $\hbar\omega \gg k_BT$ so it is reasonable to assume that the term $\tanh(\hbar\omega/2k_BT) \approx 1$. As the power is decreased, the value of the intrinsic quality factor also decreases until another plateau is reached also shown in Fig. 2.6. This is where very few material TLS defects are being excited by microwave photons. The onset of this unsaturated region of $Q_i(\langle n\rangle)$ is a key indicator of the single photon regime where it can be assumed that, on average, a single photon populates the resonator.

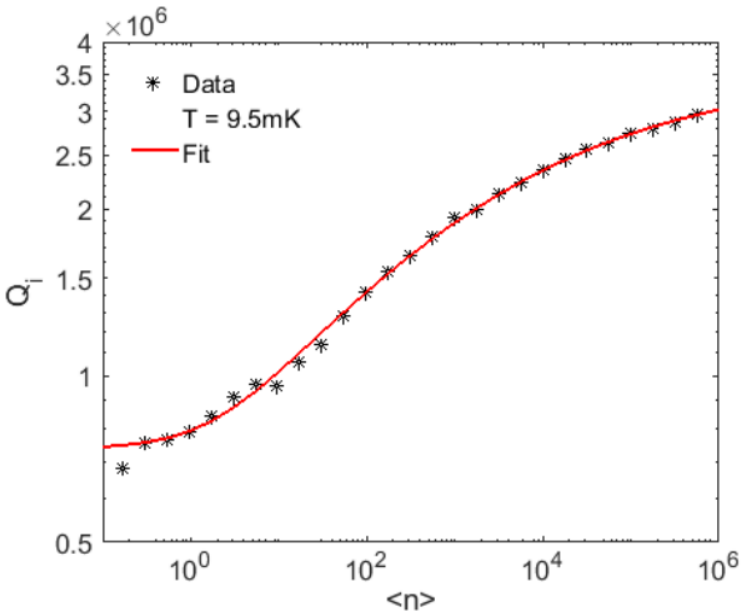

Figure 2.6: Data from Ref. [43] of the internal quality factor Q_i as a function of the average photon occupancy of a superconducting resonator $\langle n \rangle$.

Having discussed the behaviour of TLS at low temperatures and powers, and how they affect some solid-state quantum devices, this begs the question: what is the nature of TLS? The answer to this question remains elusive. However, there have been several experiments that have measured the properties of an ensemble of TLS. One such experiment uses strain spectroscopy to observe multiple two-level quantum systems coherently coupling to a superconducting qubit [33]. This experiment flexes the chip while applying different microwave pulses to measure the change in qubit excitation probability. This work shows that at least some of the TLS are in-fact defects that are inherent to a material's amorphous structure and provides strong evidence to the tunnelling of quantum particles model to explain these defects. Also observed are direct TLS-TLS interactions through avoided crossings and the frequency switching nature of TLS via non-hyperbolic strain responses.

Dedicated defect spectrometers have also been fabricated that consist of a Josephson junction in a superconducting LC circuit. By tuning the flux that penetrates the junction, which allows the resonant frequency of the circuit to be adjusted, the spectrometer can observe the splitting of the resonance frequency, a

key indicator of the device having coherently coupled to TLS defects of the same frequency [44]. These measurements allow the density of TLS defects per unit area to be calculated, a useful parameter to know for Josephson junctions when considering dielectric loss. Our NSMM has been designed to reveal the position of an individual material TLS defect, something that has not been achieved. This is important because knowing where the material TLS defects are will allow for them to be studied so that they can be better understood.

Recently some experiments have found that removing adsorbed spins on the surface of superconducting resonators has a large effect by reducing the level of $1/f$ noise. There is evidence that surface spins originating from atomic hydrogen contribute to the noise of a superconducting resonator, though the loss of the resonator does not decrease by the same factor as the overall noise level does. This is explained in the GTM, which partitions the material TLS defects in the resonator into two categories: one that is responsible for the loss and the other that is responsible for noise [40].

Frequency noise has a known impact on superconducting circuits and is a direct consequence of material TLS defects. We briefly discuss some experiments that measure the frequency noise in superconducting quantum circuits and their findings. A review of $1/f$ noise affecting solid-state quantum circuits can also be found in [13].

Noise has been known to affect the lifetime of superconducting qubits for some time. The design motivation of the transmon qubit was to create a qubit design that reduced the effects of charge noise in the circuit [27]. Superconducting resonators have also been observed to experience frequency noise. By adopting a technique from frequency metrology known as Pound-Drever-Hall (PDH) locking, often applied to atomic clocks, superconducting resonators have been characterised, and their noise processes identified, in a way that was not previously done using traditional techniques [45]. Other experiments for analysing noise in resonators have found that it is possible to calculate the density of material TLS defects in the amorphous oxidised layer of a superconducting device [38]. Noise measurements were also done whilst varying the applied power to the resonator at a fixed frequency. The data can be fitted using a model that finds that the

amplitude of the $1/f$ noise can be written as

$$A \propto \frac{1}{\sqrt{1 + \frac{|\mathbf{E}|^2}{|\mathbf{E_c}|^2}}}. \tag{2.10}$$

Here $|\mathbf{E}|^2 \propto \langle n \rangle$ is the magnitude of the electric field squared which is proportional to the average photon occupancy of a superconducting resonator. More recent work has studied how TLS affect the relaxation time of superconducting qubits by measuring this quantity many times over long time periods. The works aimed at 'benchmarking' typically measured qubit parameters as opposed to quoting the exceptional result. Within these works, noise analysis on the relaxation times tries to observe $1/f^{\alpha}$ noise spectrum. However, what is observed is a sum of this frequency noise spectra along with Lorentzian noise contributions, which is the signature of a single dominant fluctuator [46, 47]. This further motivates why a strong understanding of TLS dynamics is needed to understand, and hopefully mitigate, the effects of noise in the solid-state superconducting quantum circuits.

2.4 Analysing Noise

Having discussed the effects of material TLS defects in solid-state quantum circuits and their contribution to noise in such circuits, we will discuss how that noise is analysed and interpreted. We briefly mention power spectral density (PSD) analysis and how it is estimated and move on to discuss an analysis technique often used in frequency metrology known as the Allan variance.

2.4.1 Power Spectral Density

A commonplace technique when analysing noise data is to calculate the PSD. This can be used to analyse oscillator phase noise $S_{\varphi}(f)$ and oscillator frequency noise $S_y(f)$, where the subscript y refers to some time averaged quantity that is measured. A PSD is applied to a time-series set of data and shows a distribution of the frequency contributions to the power of a signal using Fourier analysis. To compute this with real-world data, it is necessary to use a numerical method to

calculate the Fourier transform.

For the noise analysis on time-series measurements of a superconducting resonator's resonant frequency fluctuations, we use Welch's estimation method which is built into MATLAB. Although useful for analysing time series data in the frequency domain, it does have some drawbacks. For example, Welch's method divides the data into segments and applies a time-domain window function to those segments. Depending on the choice of the window parameters, the output of the PSD can differ and result in information loss. To avoid this, we also employ another noise analysis method.

2.4.2 The Allan Variance

Here we introduce the Allan variance and its definition. This is useful for discussing the analysis methods that are used to understand the analysis performed on data from noise measurement experiments. The classical variance is a statistical measure of the deviation of the values in a distributed data set from the mean value of that data set. The Allan variance, however, is a statistical analysis technique for analysing a time-series data set that has a poorly defined mean value [48]. An example of such a data set may be a frequency-dependent system that drifts over long time periods. The Allan variance is commonly used in time and frequency metrology and for research into atomic clocks. Other applications include the characterisation of noise in voltage standards [49], ammeter calibration traceability [50], and for measuring the noise processes in superconducting micro-resonators [51], an application more pertinent to the content and work that is presented in this thesis.

The Allan variance is a function of the temporal measurement period τ, and can be computed for a data set of N discrete measurements using the equation

$$\sigma_y^2(\tau) = \tfrac{1}{2}\langle(\Delta\bar{y})^2\rangle = \frac{1}{2(N-1)}\sum_{i=1}^{N-1}(\bar{y}_{i+1} - \bar{y}_i)^2, \tag{2.11}$$

where $\bar{y}$ is the time-averaged measured quantity. For measuring frequency fluctuations, it is $\bar{y} = (f - f_0)/f_0$ where, for the case of a resonator, f is the measured frequency and f_0 is the resonant frequency. In the calculation of the classical

variance, each data point would be subtracted from the mean value of that data set. Whereas the definition for the Allan variance (Eq. (2.11)) is calculated using the difference between adjacent pair-wise data points, thus removing the need for a mean value from the calculation. The reader may also like to be aware of the existence of the Allan deviation which is simply defined as the square-root of the Allan variance $\sigma_A(\tau) = \sqrt{\sigma_y^2(\tau)}$. For examples that are mentioned in this work, we mainly concern ourselves with the Allan variance.

2.4.3 Interpreting Noise Spectra

When analysing noise, we need to be able to understand and interpret the various noise analysis methods that can be applied to oscillators, such as superconducting resonators. It has been found that both phase noise and frequency noise can be described using sums of power-laws when they are presented with using a PSD or Allan variance analysis [52]. For example, phase noise can be described by the summed over power law

$$S_\varphi(f) = \sum_{i=-4}^{0} b_i f^i. \tag{2.12}$$

The coefficients b_i correspond to separate noise processes that go with the frequency f^i. The noise processes that each of these coefficients corresponds to has been summarised in Table 2.1 and are illustrated on a log-log plot in Fig. 2.7. This table and diagram will become useful when analysing noise results later on in this thesis. Higher-order frequency noise processes can occur ($i \geq 5$) but these are not relevant for this thesis.

Just as with phase noise, the frequency noise of an oscillator can be modelled as a sum of power laws. This is expressed as

$$S_y(f) = \sum_{i=-2}^{2} h_i f^i. \tag{2.13}$$

As was the case for phase noise, the coefficients described here for the frequency noise h_i correspond to different noise processes. These are also shown in Table 2.1 and Fig. 2.7. A conversion between phase and frequency noise is possible. This is indicated by the blue arrows in Fig. 2.7. To convert between the two noise spectra,

we use the equation

$$S_y(f) = \frac{f^2}{f_0^2} S_\varphi(f), \tag{2.14}$$

meaning that we can write

$$h_i = \frac{1}{f_0^2} b_{i-2}. \tag{2.15}$$

These conversions are explicitly shown in Table 2.1 for each type of noise process.

The relationship between these noise spectra and the Allan variance is also shown in Table 2.1 and Fig. 2.7. Although it is possible to convert exactly between $S_y(f)$ and $S_\varphi(f)$ both ways, it is only possible to estimate the Allan variance from the frequency noise in one direction. This is indicated by the blue and red arrows of Fig. 2.7, which also shows an illustration of the 'bucket-like' shape of the Allan variance. Notice that there is no simple transform for the noise processes shown in

Noise type	$S_\varphi(f)$	$S_y(f)$	$S_\varphi \leftrightarrow S_y$	$\sigma_y^2(\tau)$
White PM	b_0	$h_2 f^2$	$h_2 = \frac{b_0}{f_0^2}$	$\frac{3f_H}{4\pi^2}\frac{h_2}{\tau^3}$
Flicker PM	$b_{-1}f^{-1}$	$h_1 f$	$h_1 = \frac{b_{-1}}{f_0^2}$	$\frac{3\gamma - \ln(2) + 3\ln(2\pi f_H \tau)}{4\pi^2}\frac{h_1}{\tau^2}$
White FM	$b_{-2}f^{-2}$	h_0	$h_0 = \frac{b_{-2}}{f_0^2}$	$\frac{1}{2}\frac{h_0}{\tau}$
Flicker FM	$b_{-3}f^{-3}$	$h_{-1}f^{-1}$	$h_{-1} = \frac{b_{-3}}{f_0^2}$	$2\ln(2)h_{-1}$
Random walk FM	$b_{-4}f^{-4}$	$h_{-2}f^{-2}$	$h_{-2} = \frac{b_{-4}}{f_0^2}$	$\frac{2\pi^2}{3}h_{-2}\tau$
Linear frequency drift D_y				$\frac{1}{2}D_y^2\tau^2$

Table 2.1: The conversion factors between phase modulated (PM) noise $S_\varphi(f)$, frequency modulated (FM) noise $S_y(f)$, and Allan variance $\sigma_y^2(\tau)$ understood in terms of power laws. In this table, f_H is a cut-off frequency and D_y is a coefficient for describing linear drift. The noise spectra are illustrated in Fig. 2.7. This is adapted from Enrico Rubiola [52].

the $S_\varphi(f)$ and $S_y(f)$ spectra that map to those same noise processes on the Allan variance. The coefficients for relating $S_y(f) \to \sigma_y^2(\tau)$ are shown in Table 2.1.

Although representing noise data in the form of a PSD can be useful, the Allan variance does have some extra advantages. For example, it is able to show linear frequency drift noise that is proportional to τ^2. Slow noise processes are difficult to observe with a PSD but are made easier to do so with Allan variance analysis. Another pitfall of a PSD is that when computing the PSD using some software, multiple algorithms exist across different pieces of software that calculate the spectra. This is because the spectra calculation involves using the Fourier transform of the data. Having multiple methods of calculating the same type of spectra to analyse noise can have the practical detriment of introducing inconsistencies between different analysis methods used to examine the same set of data. Whereas for the Allan variance, there is only one way of computing its value and that is to use the definition in Eq. (2.11).

There are benefits to using both the PSD and Allan variance when analysing noise data. Later on in this thesis, both analysis methods are used on noise data for a superconducting resonator probe and what noise processes limit it.

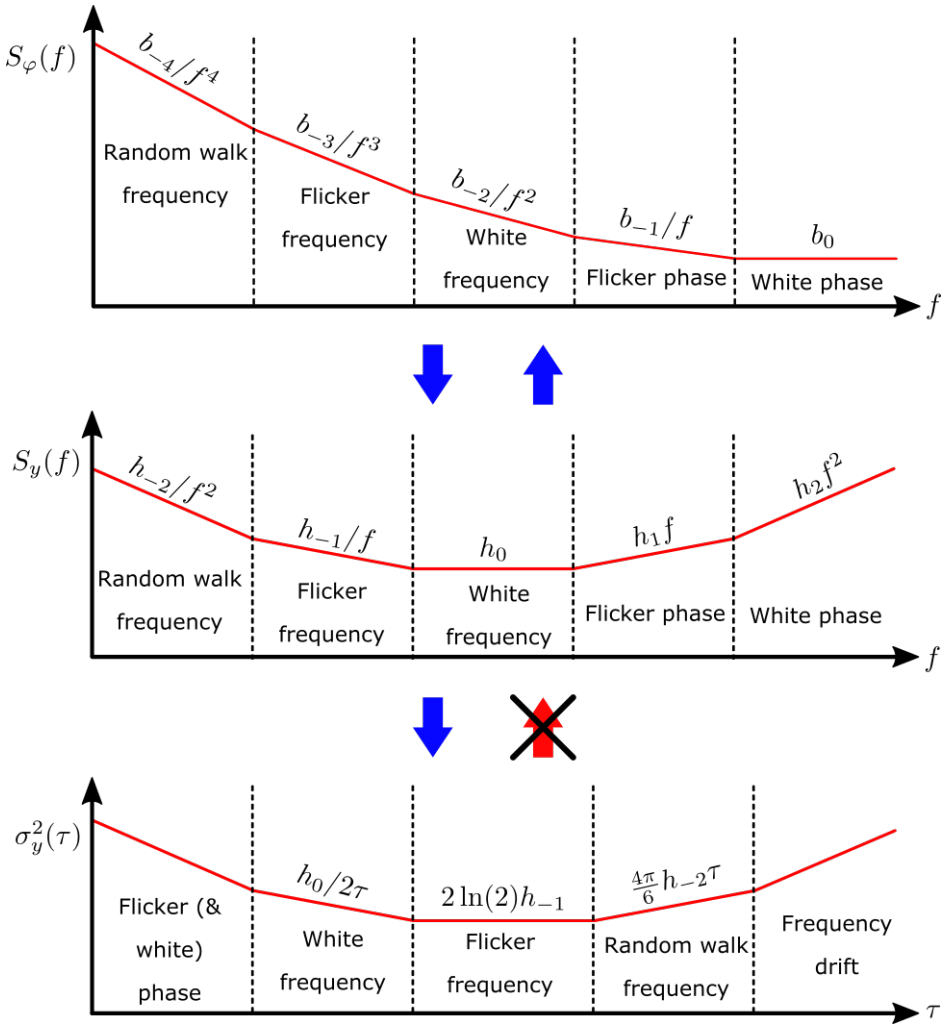

Figure 2.7: Noise spectra for phase modulated noise $S_\varphi(f)$, frequency modulated noise $S_y(f)$, and Allan variance $\sigma_y^2(\tau)$ understood in terms of power laws. Arrows indicate how each spectra can be converted to and from one another. The specific conversion factors are displayed in Table 2.1. This is adapted from Enrico Rubiola [52].

Chapter 3

Near-Field Scanning Microwave Microscopy

In this chapter, we first review some of the literature around classical scanning microwave microscopy, going through a brief history of the field, different types of scanning probes, different applications of the technique and discussing some of the more recent research in the field. We then discuss some principles of classical near-field scanning microwave microscopy (NSMM) and the underlying physics to the subject. This section also discusses different tip geometries and how they can be modelled so that the tip radius can be estimated. We then move on to discuss some principles of atomic force microscopy (AFM) and the origin of the force between an AFM tip and the surface of a sample. We then discuss various methods of distance control and which method is most suitable for the experiments presented in this thesis. Finally, we discuss the physics of taking NSMM into the quantum regime and how the interaction between a resonant NSMM probe can couple to a two-level quantum system. We also present simulations of the expected shift in frequency of the probe-sample interaction.

3.1 Literature Review

Historically the resolving power of any microscope was dictated by the wavelength of light used to observe a sample. However, it is widely considered that Synge first proposed a method for overcoming this limit in 1928 to create an ultra-high-resolution microscope [53]. Though the technological capability to build such a device was not available for some time. These concerns were also independently expressed by O'Keefe in 1956 [54]. The first demonstration of a near-field microscope was in the microwave regime by Ash and Nichols in their 1972 work [55]. To

achieve this, a small aperture in a thin diaphragm at the end of a hemispherical resonator was excited by a signal with large illuminating power. Provided this aperture is in close proximity to the sample, the small microwave fields about the outer side of the resonator can overcome the classical diffraction limit.

Broadly speaking, a near-field microscope uses either a broadband [56] or a resonant [57] probe, though many implementations of near-field microscope probes have been demonstrated. They rely on focusing evanescent waves around an aperture or a probe and measuring the changes in the stored energy of the evanescent fields that decay exponentially with distance. This is referred to as the 'near-field' in the literature [15]. Some types of near-field scanning microwave microscopes include microwave resonator cavities or waveguides that have a small aperture close to the sample, as shown in Fig. 3.1(a), to scan a sample. Others have microfabricated parallel strip lines that consist of a dielectric (such as SiO_2) flanked by two parallel strips of conducting material (such as Al) as shown in Fig. 3.1(b). Changes in the permittivity in a sample will cause a corresponding change in the stored energy in the electric field about the tip, this, in turn, causes a change in the resonant frequency of the probe, which can then be tracked. A modified AFM cantilever that is shielded with metal and connected to the central line of a coaxial cable, as shown in Fig. 3.1(c), can also be used as a microwave probe [58]. Open-ended coaxial lines (Fig. 3.1(d)) have also been implemented as microwave scanning probes [56] and to achieve a resolution down to 100 µm. The central wire of a coaxial cable can be attached to an scanning tunnelling electron microscopy (STEM) tip, as in Fig. 3.1(e), and has been reported to increase the resolution of such a microscope to 100 nm [59]. A loop of wire that shorts the central line of a coaxial cable to the outer shield to create a magnetic loop, as shown in Fig. 3.1(f), has also been demonstrated to measure the magnetic permeability of a sample down to length scales of 200 µm [60]. Each probe design has led to increased variety and innovation in the field of microwave microscopy. Ultimately, it was the introduction of precise distance control methods, mainly brought about from AFM and STEM technologies, that helped to accelerate research with and into near-field scanning microwave microscopy (NSMM) to where it is today.

NSMM has since found itself to be useful for many different applications. For example, early evidence for the existence of the superconducting energy gap in

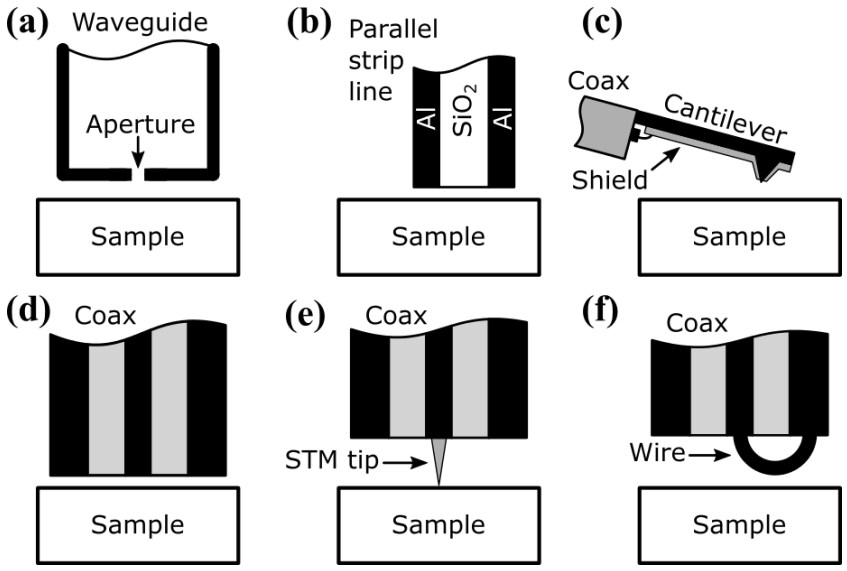

Figure 3.1: An illustration of several different implementations of microwave probes. These diagrams were adapted from Ref. [15]. Explanation in the text.

superconductors was shown using microwave transmission experiments [20,61,62]. Similar microwave microscopy techniques have also been applied to superconductors to identify superconducting phases in multiphase samples [63]. NSMM techniques can also be used in the characterisation of graphene layers by using an electromagnetic cavity with a spherical tip. This method makes it possible to measure variations in the local permittivity of a graphene sample [57]. The semiconductor industry has also used NSMM for measuring dopant concentration levels in p-type silicon [64] and for capacitance measurements for spatially resolved nanoscale structural mapping of a sample that can be achieved by using a network analyser to measure reflected microwaves from the sample [65]. There have even been reported uses of NSMM for biological samples. NSMM can be a desirable scanning method in biology due to its non-invasiveness. By using a resonant cavity and measuring its frequency shift, the detection of buried biological anomalies such as tumours is possible [66]. The detection of hybridisation in DNA films is also possible by observing the reflected microwaves from a tungsten tip due to changes in the dielectric properties of the DNA strands on a sample [67].

In this work, some essential requirements are necessary to fulfil in the design of an NSMM that can reach the quantum regime. One such requirement is that the

microscope needs to be operated at low power. This is so that, on average, a single photon occupies the resonant probe, $\langle n \rangle \sim 1$. Having such low powers ensures that any two-level quantum system will not be saturated by large numbers of photons. This motivates the need to achieve low power microwave measurements for our NSMM. Another requirement is the need to operate the NSMM at low temperatures, on the order of ∼10 mK. To ensure that the microscope probe would be able to couple to an individual quantum system, low temperatures are required so that any two-level system is not thermally saturated and this increases the likelihood that a quantum system's transition frequency is much greater than environmental thermal fluctuations, $\hbar\omega \ll k_B T$. Lowering the temperature also increases the number of two-level quantum systems that will be in their ground state. Another requirement is that the probe must also have a low rate of loss *i.e.* a high Q-factor. If the resonant probe is to couple to an individual two-level quantum system, the loss rate of the probe must be smaller than the coupling strength of the interaction. Finally, precise tip-to-sample distance control is necessary. This means that the effects of external mechanical vibrations on the tip should be minimised. This ensures a well-defined coupling between the NSMM probe and the sample surface and will reduce dither in the tip-to-sample distance.

In most of the previously discussed applications of classical NSMM, there is little or no mention of their operating power as a figure of merit. The interactions are described using classical electromagnetic theory which suggests large numbers of photons are intended to be involved in the interaction between a microwave probe and a sample. However, some works do quote the power levels of their microscopes. For example, NSMMs being used to quantitatively measure the conductivity and permittivity of a sample using microwave impedance microscopy do state an input microwave power to the NSMM probe of -20 dBm [68]. Other work has shown that extremely low powers of -100 dBm can be achieved with NSMM. These low power levels can be reached with the use of a micro-machined superconducting resonator as the NSMM probe and with the aid of a technique adopted from optics known as Pound-Drever-Hall locking [69], that can be used for high-sensitivity microwave measurements. This measurement technique has been applied to on-chip superconducting resonators to operate them in the single photon regime [43]. Given the ability of superconducting resonators to reach sin-

gle photon energies, and that they typically operate in the microwave regime, a resonator that has been designed and micro-machined as a probe would make an ideal candidate for our NSMM probe. Low power microwaves in the single photon regime, and high-sensitivity microwave measurements, are necessary to investigate two-level quantum systems so that they do not become thermally saturated and coherent coupling can be achieved.

There have been some NSMMs that have been demonstrated to operate down to cryogenic temperatures. For example, resistive mapping of YBCO films have been performed in older cryogenic systems that make use of cryogen baths (typically using LN2 or LHe), with the microscope protected from direct contact with the liquid with a vacuum jacket [70]. Other similar experiments for scanning probe microscopy (SPM) in a cryogenic environment have also been carried out to use microwave impedance microscopy to study semiconductors [71]. Other experiments have combined STEM with microwave scanning microscopy in cryogenic systems with the use of a resonant probe. A lumped element model can be used to describe the behaviour of the probe which can be compared with the near-field response on silicon wafers to show good agreement with the scan result [72]. These systems all make use of circulating liquid cryogens. There also exists cryogen-free Low-temperature systems that have been used for scanning microscopy with a superconducting quantum interference device (SQUID) [73] as the probe to map small magnetic fields in a sample. This requires low temperatures that achieved by using a 'dry' dilution refrigerator (DR) to cool the microscope. This experiment uses an Nb patterned SQUID attached to a copper cantilever as the probe. This probe is then moved with the use of piezo-steppers and S-bender piezos for the positioning of the probe. These experiments are not isolated examples and there have been many other implementations of NSMMs in cryogenic environments. These cryogenic microscopes typically reach temperatures on the order of Kelvin. To achieve coherent nanoscale measurements with NSMM, much lower temperatures, on the order of tens of millikelvin, need to be achieved. A review article from the National Institute of Standards and Technology (NIST) [74] discusses, in detail, a cryogenic SPM facility. This facility has many features including tip preparation, field-ion microscopy, horizontal transfer stations and more. Though it is the cryogenic SPM system that is inside of a DR that is of particular interest. It

consists of a DR system, similar to the DR used in the experiments in this thesis, with an SPM system placed at the coldest part of the cryostat that operates at approximately 10 mK. Most of these works pay particular attention to minimising the effects of external vibrations on the system, leading to increased mechanical noise. This same issue is addressed in the work presented in this thesis.

For resonant probes, a high Q-factor is desirable as this means the probe will have a smaller loss rate. Specifically for the case of low power NSMM, a high Q will increase microwave sensitivity (particularly if the Pound-Drever-Hall locking method is to be employed). To get a sense of some of the values for the Q-factors that exist in NSMMs, we review some of the literature that quotes the quality factors of their microscopes. A stainless steel wire, with a diameter of 50 µm, coupled to a dielectric resonator operating at 4 GHz has been reported to have $Q = 2.4 \times 10^4$. This experiment was done at room temperature [75]. Another room temperature NSMM that uses an yttrium-aluminium-garnet (YAG) dielectric puck inside of a copper cavity coupled to a metallic probe has been reported to have $Q = 3 \times 10^3$ with a resonant frequency of 3.8 GHz [57]. An NSMM with a Pt-Ir tip connected to the central conductor of a coaxial cable demonstrates an estimated $Q \sim 10^3$ [76]. Although not directly quoted, the Q-factor from this work can be estimated from the presented microwave transmission plots. More recently, a low-temperature NSMM that utilises a coaxial cable resonator has reported room-temperature quality factors of $Q = 1.2 \times 10^3$ and at lower temperatures of $Q = 2 \times 10^3$ with temperatures of 77 K [72]. Most of the literature seems to report resonant NSMM probes with Q-factors approximately in the range of 10^3 - 10^4. Ideally, our NSMM would need to have a high a Q-factor as possible. It has been reported that by using a micro-machined superconducting resonator as an NSMM probe, Q-factors on the order of $Q = 1.6 \times 10^4$ can be produced at very low temperatures (300 mK) and at low powers (-100 dBm) [69]. This is a promising result if we are to achieve similar resonant probe quality factors at such low temperatures and powers.

NSMM has useful applications in many areas. As mentioned earlier, the major development in the field of microwave microscopy techniques has been the advancements that were made in precise distance control and feedback methods. This meant that it became possible to bring the distance between a scanning probe

tip and a sample surface to the order of nanometers [15]. This helps to improve the signal-to-noise (SNR) ratio and achieves higher spatial resolution when scanning. There are three main methods of distance control that are commonly used in NSMM [77]. The first method is tunnelling-based current feedback, as used in STEM. This makes use of the phenomenon of quantum mechanical tunnelling and uses a feedback loop with the current from the tunnelling electrons as the feedback signal to precisely control the distance to the surface. The scanning tip and the sample need to be electrically conductive for this method to work. Another distance control technique is the use of a cantilever with an optical laser working in tandem with a feedback loop, popular in AFM. In this method, a sharp tip is attached to the underside of a cantilever and a laser is reflected off of the top side and measured by a photo-detector. The deflected beam from the cantilever is then used to map the topography of the sample surface. In the third method, a mechanical/piezoelectric tuning fork with feedback can also be used for precise distance control. This makes use of the intrinsic piezoelectric property of quartz that these tuning forks are typically made from. The resonant frequency of the tuning fork is shifted when the scanning tip comes in to close proximity with the sample surface. This is due to the atomic forces of the sample surface that are applied to the oscillating tuning fork prong. Any perturbation in the resonant frequency will alter the voltage of the measured error signal in a feedback loop and so the distance to the sample surface can be adjusted by a PID controller.

Having reviewed some of the more relevant pieces of literature, we address the question: is it feasible to meet the requirements for bringing NSMM into the quantum regime? Research has shown that it is indeed possible to operate an NSMM in a cryogenic environment. The combination of low power, low temperature, a high-Q resonant probe and isolation from external mechanical vibrations are what brings the microscope into the "quantum" regime. With the use of a superconducting resonator as a probe it is indeed feasible to operate an NSMM at the single photon energy levels for the interrogation of individual two-level quantum systems. Work on the plausibility of operating an NSMM in the quantum regime has been investigated by de Graaf who has theoretically shown that non-invasive, low power and coherent interactions with TLS is possible with a cryogenic NSMM. As described in Ref. [69] and Ref. [17], the NSMM probe used is a specially de-

signed micro-machined, thin-film superconducting fractal resonator. This specific resonator is designed to be small and compact enough to be used as a scanning probe. Such a probe can be mounted to an individual prong of a quartz tuning fork for precise distance control between the tip and sample. Superconducting resonators are often used when it comes to constructing macroscopic circuits for quantum electrodynamics (QED) and can be used to couple to qubits and two other two-level quantum systems. This makes them ideal for an NSMM probe that aims to operate in the quantum regime. What we propose is to 'take the resonator out of the page' and to do scanning probe microscopy with it to measure quantum systems.

Since its inception, NSMM has proven to be a widely applicable tool in many disciplines of research to investigate a number of different materials, gathering information such as the complex conductivity, polarisation and the dielectric properties of a material. This has been made possible by advancements in precise distance control between a probe and a sample surface. The remainder of this chapter discusses some of the theoretical descriptions of classical NSMM and how we adapt it to quantum NSMM. We also discuss introductory AFM physics and how it is applied to our proposed NSMM. This discussion will highlight some of the design choices that have been made for the microscope. After this we discuss some of the theory behind a quantum interaction between an NSMM probe and a two-level system and then present some supporting simulations.

3.2 Principles of Classical NSMM

All NSMMs presented in the literature operate in the classical regime. This means that there are a large number of photons involved in the interaction between a microwave probe and a sample and so the electromagnetic interaction can be treated classically. To understand the response from the NSMM considered in this thesis it is important to understand the physics that describes the interaction between the microwave near-field and any sample under interrogation. In this chapter, we will discuss the electrodynamics of an NSMM probe as it is brought toward a metallic sample and the different models that can be applied to describe this. We also present simulations of expected classical NSMM scanning and discuss the results

in the context of the chosen model. Finally, we discuss distance control using a tuning fork, and the reasoning for this choice, in our experiments.

As the name implies, NSMM operates by coupling a scanning probe to a sample via the near-field region of the electromagnetic field produced by the probe. If this tip has some characteristic length D, associated with it, and the radiation has a wavelength of λ, then the near-field typically occupies the region $D \leq r \ll \lambda$, where r is a radial vector describing, in this case, the distance from an NSMM tip to a sample [15]. When an electromagnetic wave is incident to some boundary *i.e.* the tip of the probe, some of the wave will be reflected and some will be transmitted, producing a so-called evanescent wave. For a boundary aligned along the x and an incident wave along the z axis, as shown in Fig. 3.2, the electric field of an evanescent wave can be written as

$$\mathbf{E}_T = \left(\mathbf{E}_{0,T} e^{i(k_x x - \omega t)}\right) e^{-\xi z}, \tag{3.1}$$

where y components are neglected. Here, $\mathbf{E}_{0,T}$ is the amplitude of the transmitted wave, k_x is a wave-number in the x direction and ξ is a coefficient describing the rate of exponential decay of the evanescent wave. This equation states that there is a propagating wave in the direction along the boundary that decays exponentially at distances further away from that boundary, shown by the z-component of the transmitted electric field $\mathbf{E}_{T,z}$, in Fig. 3.2. This implies that the energy of the wave is concentrated in the vicinity of the tip.

The interaction between and NSMM tip and a sample can be described by the tip-to-sample capacitance C_{t-s}, and the electromagnetic properties of the sample. The means that the response can be either dissipative or reactive. For a resonant probe with some voltage at the tip, this interaction is dominated by reactive contributions. In the following, we assume a purely capacitively reactive response caused by C_{t-s}, simplifying the NSMM description to a lumped-element electrostatic interaction. For a metallic resonant NSMM probe, we can write the frequency shift as

$$\Delta f = \frac{1}{2\pi}\left(\frac{1}{\sqrt{L(C+\Delta C)}} - \frac{1}{\sqrt{LC}}\right), \tag{3.2}$$

where L is the inductance and C is the capacitance of the resonant probe. The

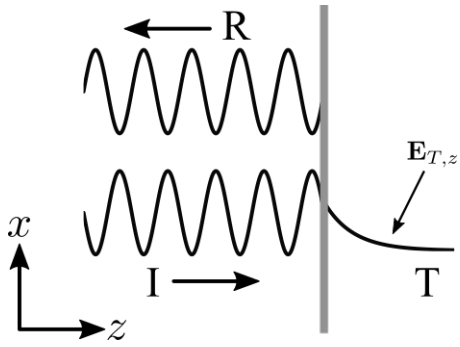

Figure 3.2: A diagram showing an incident (I), reflected (R) and transmitted (T) wave. The grey region is a boundary with a different refractive index. The transmitted wave shows only the exponential decay in the z direction of an evanescent wave.

term ΔC is the change in capacitance due to the changing coupling capacitance as the probe is moved towards or away from the sample surface. This means that ΔC is a function of z, the tip-to-sample distance. The term $1/(2\pi\sqrt{LC}) = f_0$ is the natural resonant frequency of the resonant probe, for large values of z. The shape and size of the tip will also affect the change in coupling capacitance. Assuming a rounded metallic tip, it would be expected that ΔC would be dependent on the tip radius R. The functional form of the change in capacitance is non-trivial for a realistic NSMM probe. However, approximations can be made to simplify the tip-sample interaction model. Some common approximations used in the literature for modelling the change in tip-to-sample capacitance are discussed in more details in the following sections.

3.2.1 Parallel Plate Model

The simplest way to model the change in capacitance is to use a parallel plate capacitor model. Assuming that the tip is one end of a cylinder, the capacitance for a circular tip is

$$C_{\text{pp}} = \frac{\varepsilon_0 \pi R^2}{z}. \tag{3.3}$$

This model has been used with limited success in describing the behaviour of the electric field between a tip and a sample [78]. This model is limited because it is only applicable to conductive samples and it can only be used as a first-order

approximation, due to $1/z$ dependence.

As the models assume that the overlapping circular area of the parallel plates is the end of a cylindrical tip, it does not account for any extra capacitance caused by fringing fields at the edges of the parallel plates. Although this can be accounted for by adding an extra logarithmic term to account for the total capacitive change. This has been empirically found by [79].

Despite its relative success, this model does not capture the full behaviour of the tip-to-sample capacitance. To be able to do this, a more sophisticated model is necessary that can account for the more complex shape of the tip.

3.2.2 Spherical and Conical Tip Model

A more sophisticated approximation for the tip-to-sample capacitance is to assume that a metallic sphere of radius R, is above an infinite plane at a distance z. This is shown in Fig. 3.3(a). The capacitance between the sphere and the plane can be calculated using the method of image charges. This model has shown good agreement with experimental data [80].

Another approach for calculating capacitance between the sphere and the plane uses an analytical method that has been demonstrated by Hudlet [81]. This results in a logarithmic correction for the capacitance and can be written as

$$C_{\text{sph}} = 2\pi\varepsilon_0 R \ln\left(1 + \frac{R}{z}\right). \tag{3.4}$$

In this method, the conducting sphere is infinitesimally faceted and the capaci-

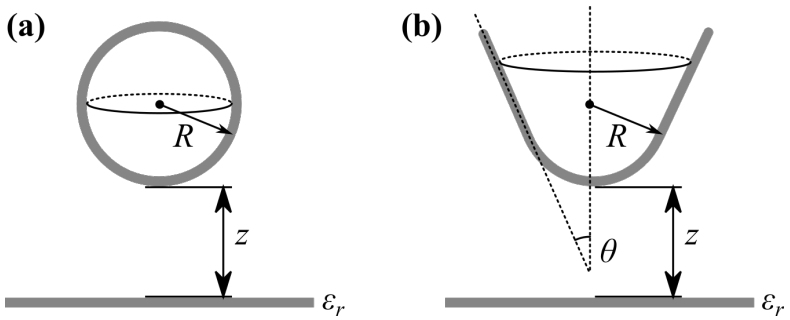

Figure 3.3: An illustration of the model parameters that define **(a)** a metallic spherical tip and **(b)** a metallic conical tip truncated with a sphere at the apex.

tance between each facet and the sample surface is calculated. This is done by considering the vertical force that is applied to the sphere due to the electric field between them. Each contribution is then summed over to calculate the total applied force and therefore the capacitance between sphere and plane. This same method can be applied to the geometry of a cone truncated by a sphere to form a tip-like apex, shown in Fig. 3.3(b). This yields a similar result to the spherical tip model and the capacitance of the metallic conical tip above an infinite conducting plane can be written as

$$C_{\text{apex}} = 2\pi\varepsilon_0 R \ln\left(1 + \frac{R(1-\sin\theta)}{z}\right). \tag{3.5}$$

This model accounts for the taper angle θ of the conical tip and the capacitive contribution from the cone. When the taper angle $\theta = 0$, this equation reduces to Eq. (3.4) for the capacitance for a metallic sphere above an infinite plane.

Both of these models are an improvement on the parallel plate model as they can more accurately show how the electric field is distributed about a conductive tip. This means that it is not necessary to add an extra term to account for fringing fields. The two models also reflect a more realistic shape of a nanometer-sized tip. It is this model that we assume for the NSMM presented in this work when analysing the resonant frequency shift of a microwave probe as a function of tip-to-sample distance in this thesis.

3.2.3 Capacitive Scanning Simulations

We can make use of tip models to approximate the change in capacitance between the probe and a sample. Simulations can produce a capacitive map when the tip scans over a sample. To do this we have used COMSOL Multiphysics 5.4 that uses a finite element method to implement the electrostatic interaction. The model consists of a metallic conical tip (as shown in Fig. 3.3(b)) and an underlying sample that consists of a thin metal pattern on top of a dielectric substrate. The metal patterning is an interdigitated capacitor with two smaller metallic squares, each being 2×2 µm^2 in size, located nearby. The finger width and the separation between fingers are both 1 µm. An image of this model is shown in Fig. 3.4(d).

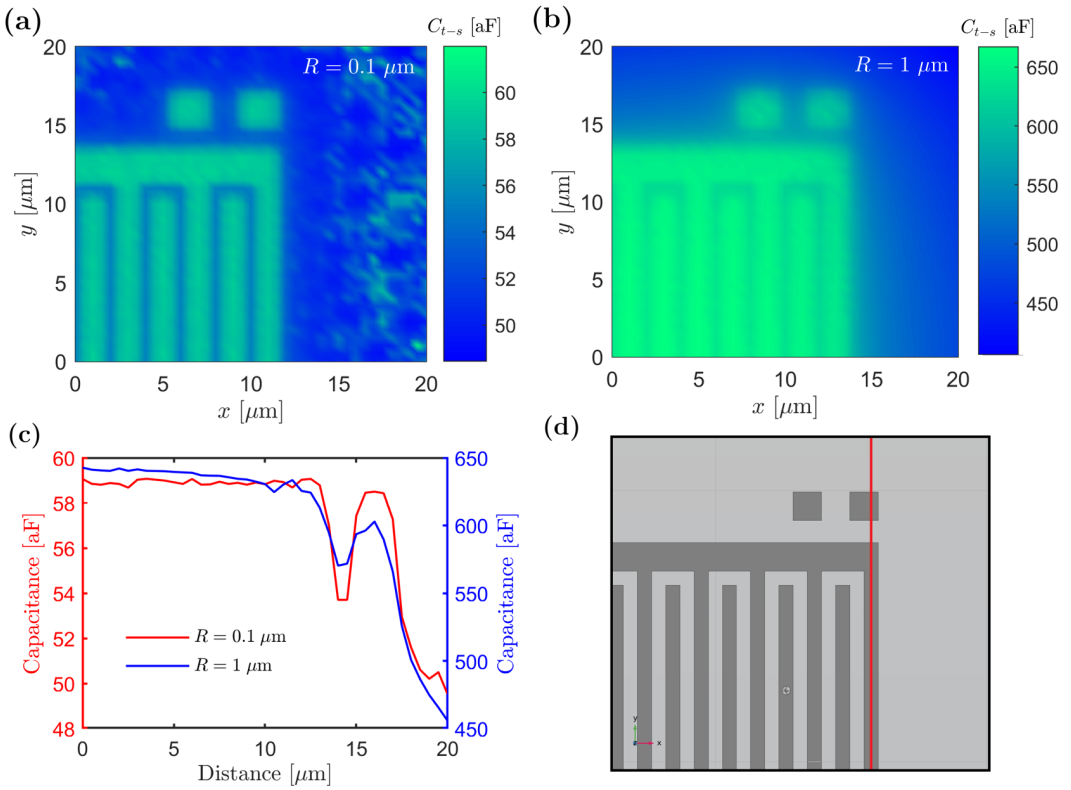

Figure 3.4: A COMSOL Multiphysics simulation from evaluating the capacitance between the metallic tip and the corner of a metallic inter-digitated capacitor on dielectric for **(a)** a tip radius of $R = 0.1$ µm and **(b)** a tip radius of $R = 1$ µm. **(c)** Lines traces from each of the capacitance simulations and **(d)** a screenshot of the area being scanned. The red line shows where the line traves where taken from. Dark grey and light grey represent conductor and insulator, respectively.

This model resembles the sample that is measured later on in this thesis, the details of which are discussed further in Chapter 5.

We performed two simulations each with different tip radii. To generate the images, the capacitance is calculated for each position of the tip, while the tip-to-sample distance is kept constant. The results of the simulations are shown in Fig. 3.4. Shown in Fig. 3.4(a) is a capacitive map for the case where the tip radius $R = 0.1$ µm. We see a contrast between the metal structure and the insulating substrate due to the change in the dielectric response of the two materials. The tip size is much smaller than the size of the features on the sample. This means that the capacitive coupling to the larger inter-digitated structure

shows a similar capacitance compared to when the tip is over the smaller adjacent metallic squares. This suggests that the measured frequency shift of a resonant NSMM probe (described by Eq. (3.2)) would be the same for both structures for this tip radius, relative to the size of the sample.

Shown in Fig. 3.4(b) we see the case when $R = 1$ µm. Here the capacitance between the tip and larger inter-digitated structure is overall greater than the capacitance between the tip and the smaller metallic squares. This is to be expected as the capacitive coupling to ground is weaker for the smaller squares than it is for the larger structure. The spacing between fingers for the inter-digitated structure also appears smeared out for the case of a larger tip radius. This is because there is greater coupling to adjacent metallic fingers when the tip is similar in size to the metallic features, causing an increase in capacitive coupling two both fingers that are either side of the regions of the dielectric.

Figure 3.4(c) shows two line traces, one from each of the capacitance map simulations. The lines are taken from the red line shown in Fig. 3.4(d). These line traces show how, for the smaller tip radius, the capacitive coupling between the larger metallic structure and the smaller metallic squares remains approximately the same. Whereas for the larger tip radius there is a noticeable decrease in the capacitance between the tip and interdigitated capacitor and the tip and the smaller squares. It is worth noting the difference in scale of the two y-axes.

3.3 Principles of AFM

The basic principle behind AFM is that a sharp tip is used to measure the forces between it and a sample surface. Scanning the tip across the surface means that a map of the topography of the sample can be created. AFM techniques can be broadly categorised into three operating modes: tapping, contact and non-contact. Tapping mode is where the scanning probe is excited or oscillated in some way and deflections from this motion, caused to the physical tapping of a sample, are measured. Tapping modes of operation usually require some form of feedback mechanism for distance control. Contact AFM probes are 'dragged' across the surface of a sample and non-contact probes maintain some distance above the sample surface. The application for the AFM typically dictates the choice of

operational mode. In our case, we wish to create an NSMM that is non-invasive and does not degrade the sample over time. Therefore the choice of a non-contact mode of AFM is desirable for our application. This operational mode provides atomic-scale resolution that is comparable to STEM [82]. It typically operates by exciting a probe at its mechanical resonant frequency and measuring the shift in that resonant frequency as the atomic forces perturb the probe.

The forces that act on the probe are important to understand for force microscopy. The types of forces depend on the material properties of the sample and the probe and the experimental conditions of the microscope. We mainly concern ourselves with solid-state sample surfaces and a conductive probe in a vacuum, so liquid and capillary forces are not essential here. Short-range forces typically act on the scale of individual atoms. They can be considered as chemical forces arising from the repulsion of atomic nuclei or overlapping electron wavefunctions. They can either be attractive forces, where the overlapping of electrons reduces the total energy of the atomic tip-sample system, or repulsive forces, which can be a direct consequence of the Pauli exclusion principle. Van der Waals forces are another relevant force contribution to consider. These a distant dependent forces that originate from attractive electrostatic interactions between permanent or short-lived dipole moments [82]. Other contributions can include electrostatic forces that arise from the build-up or presence of static charges. These forces can be calculated using Coulomb's law. Electrostatic forces are often minimal when

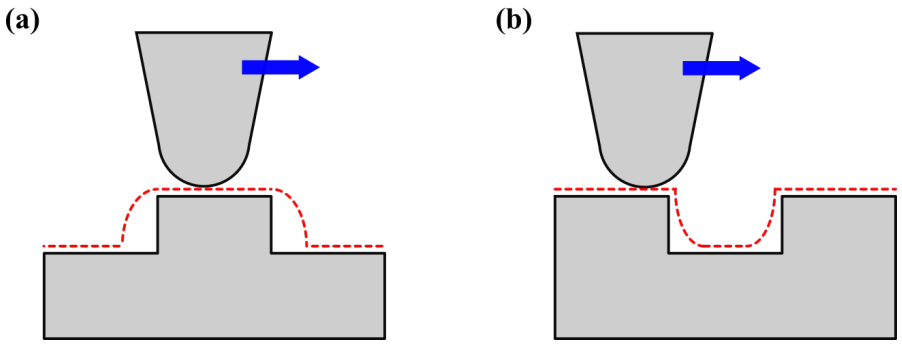

Figure 3.5: A sketch of two examples of convolution AFM artefacts for **(a)** a protrusion from the sample and **(b)** a trench feature on the sample. The blue arrow shows the direction of motion for the tip and the dashed red line shows the convoluted response as measured by the AFM.

there is a conducting tip or sample involved.

AFM is a powerful imaging tool that can achieve atomic-scale resolution images of a sample. However, it can be subject to image artefacts. The most common type is a convolution of the tip and a sample feature. They can occur when the radius of the tip is large compared to the characteristic dimensions of a feature on the sample. Figure 3.5 shows this effect for the case of a protruding feature and a trench in the sample. The red dashed line in these diagrams shows the convoluted response as seen by the AFM when it is moved across the surface. Another type of artefacts can be from the PID settings of the feedback control. A slow feedback controller may leave the cliff-edge of a raised feature and take a relatively long amount of time to reach the lower part of the sample. Though this can be checked by doing forward and backward line scans. Conversely, a quick feedback controller may not spend enough time at the surface a pull-away from features far too quickly for them to be measured.

3.3.1 Distance Control

To be able to effectively employ NSMM techniques in this experiment, it is first necessary to have a method of scanning a sample at a fixed and small distance from the sample. This distance needs to be less than the required microwave resolution and in the case of a two-level system coupling, as small as a few nanometers. This is because confined electromagnetic fields in a scanning tip are highly sensitive to the tip-sample separation distance. Large fluctuations in this distance can lead to image artefacts ergo leading to inaccurate imaging of the sample [83] and poor coupling to two-level system.

There are a number of ways to implement distance control in an SPM system. The choice of distance control is very much dependent on the application. For example, a common method is to reflect a laser from the back of an oscillating cantilever, often referred to as beam-deflection. The reflected signal is then measured by a small array of photo-diodes that measures the deflection of the cantilever. This system, although widely applied, is not suitable for our NSMM. The laser would heat the probe and is simply not viable in a cryogenic environment.

Another commonly used distance control technique is to use STEM. In brief,

this method uses the quantum tunnelling of electrons passing from a conductive tip to a conducting sample over a small distance. By measuring the current that tunnels between the probe and sample, then connecting this signal to a feedback loop allows for the current to be tracked and kept constant with the use of a PID controller. As the current changes, the experimental electronics keep the tip-to-sample distance the same as the sample topography is traced by the STEM tip. Although this method provides precise distance control with very small tip-to-samples distances, it requires a conductive sample. Meaning that any dielectric sample could not be used in our NSMM.

The experimental requirements for the operation of the microscope at low temperatures and low power provide certain challenges when trying to incorporate a precise distance control method for the NSMM. Ultimately the use of a quartz tuning fork was chosen because, unlike a conventional AFM cantilever, it does not require a laser feedback system to detect deflections due to tip-sample forces. The advantages of using a tuning fork include that it can be used at low temperatures and it is indifferent to the electrical properties of the sample. In the next section, we discuss tuning fork distance control in more detail.

3.3.2 Tuning Fork AFM for Cryogenic Scanning

The use of a piezoelectric tuning fork for precision distance control has been well established for some years now [84] and has been demonstrated for use in cryogenic applications [85]. The operating principle is fairly straight-forward: by applying

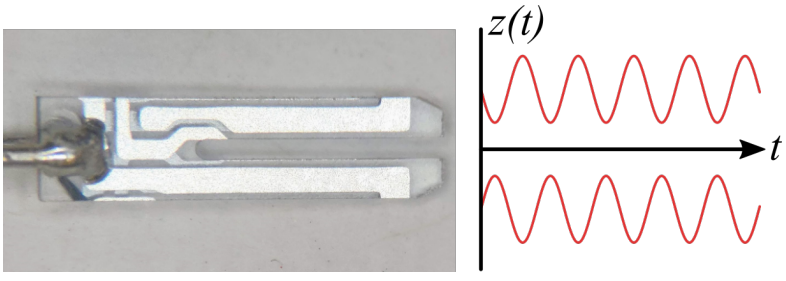

Figure 3.6: A photograph of a quartz tuning fork with adjacent plot of each prong displacement $z(t)$, as a function of time t, indicating the primary mode of oscillation of the tuning fork. The resonant frequency is $f_{r,\mathrm{TF}} = 32.7$ kHz.

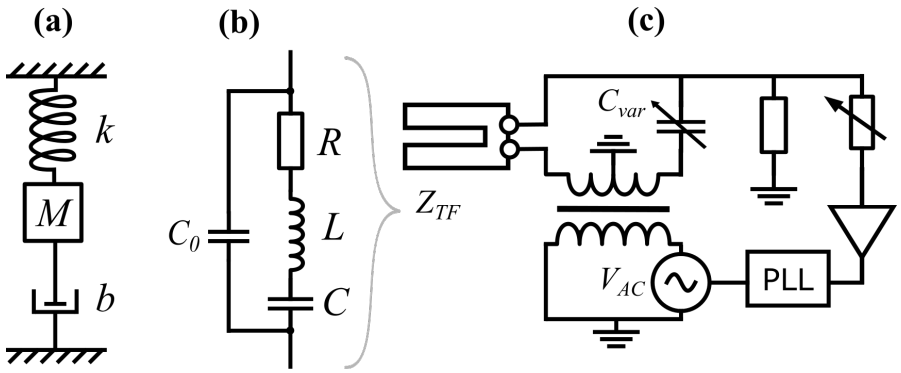

Figure 3.7: **(a)** The mechanical equivalent to a resonator circuit where k is the spring constant, M is the mass and b is the damping coefficient. **(b)** The electrical resonator circuit for a quartz crystal oscillator, in this case, a quartz tuning fork. The extra capacitance C_0 arises from the capacitance between the metallic contact pads that are separated by the dielectric quartz crystal. **(c)** The tuning fork connected to the antiresonance compensation circuit with the variable resistor and variable capacitor C_{var}. This diagram also shows the system connected to the PLL.

an AC voltage to the tuning fork, the prongs oscillate in opposition to one another - the primary mode of oscillation - at resonance. This is illustrated in Fig. 3.6. This motion keeps the centre of mass of the tuning fork static. The direction of the displacement of the prongs is aligned to be perpendicular to the sample surface. As the tuning fork approaches the sample, it's resonance properties - namely the resonant frequency, phase angle and energy dissipation - are altered due to the atomic surface forces acting on the probe. By detecting the piezo-electric response with a phase-locked loop (PLL) from the tuning fork, we can monitor the tuning fork's resonant frequency.

The tuning fork itself can be modelled as a simple RLC resonator circuit shunted with a stray capacitance C_0, as shown in Fig. 3.7(b). The physical reason for C_0 is due to the capacitance between the metallic electrodes separated by the quartz dielectric crystal. Analogously, it can be described as a damped mechanical resonator. By comparing the two differential equations for a mechanical oscillator and an RLC resonant circuit one has

$$F = M\ddot{x} + b\dot{x} + kx \qquad \text{and} \qquad V = L\ddot{q} + R\dot{q} + \frac{1}{C}q. \tag{3.6}$$

From these two equations, we can relate the mechanical and electrical properties of the tuning fork. Important parameters such as the quality factor Q, and the resonant angular frequency ω_0, can be written as

$$Q = \frac{1}{b}\sqrt{kM} \qquad \longleftrightarrow \qquad Q = \frac{1}{R}\sqrt{\frac{L}{C}} \tag{3.7}$$

$$\omega_0 = \sqrt{\frac{k}{m}} \qquad \longleftrightarrow \qquad \omega_0 = \frac{1}{\sqrt{LC}} \tag{3.8}$$

for each type of oscillator. However, the introduction of the capacitor C_0 in the electrical model of the tuning fork gives rise to modified behaviour in the current response of the tuning fork when performing a frequency sweep. The shunted capacitance gives rise to a so-called antiresonance *i.e.* a current minimum peak at a frequency around the tuning fork resonant frequency [86]. This antiresonance can be troublesome as it also adds a second phase shift of 180° that cancels out the change in phase caused by the tuning forks resonant frequency. The trouble comes from the fact that we use a PLL circuit (discussed further in the subsequent section) to lock to the tuning fork's resonant frequency. If there are two sharp gradients in the phase response of the tuning fork's readout signal then its stability may be compromised. To suppress the contribution to the frequency response due to the antiresonance some additional electronics are required that are designed to compensate for the phase response induced by the extra capacitance C_0.

The antiresonance effect can be compensated for with the use of a variable capacitor and a transformer. A circuit diagram can be seen in Fig. 3.7(c). The transformer produces two identical waveforms that are shifted by 180° in phase. Then by adjusting a variable capacitance C_{var}, such that $C_{\text{var}} = C_0$, will negate the effect of this shunted capacitance. The difference in phase will mean that the impedance for the capacitor C_0 will be $Z_0 = 1/j\omega C_0$ and the impedance for the variable capacitor will be $Z_{\text{var}} = -1/j\omega C_{\text{var}}$, thus the two signals will cancel one another out if $C_{\text{var}} = C_0$. The ratio of the input to the output signal for a balanced tuning fork follows the Lorentzian form

$$\frac{V_{\text{in}}}{V_{\text{out}}} = A\frac{(f_0/Q)f}{\sqrt{(f_0^2 - f^2)^2 + ((f_0/Q)f)^2}}, \tag{3.9}$$

where A is an experimentally determined constant. This resulting signal - the ideal resonance of the RLC components of the tuning fork - is then amplified and fed to a PLL which can then be used to measure the instantaneous phase near resonance of the tuning fork to keep it at a fixed value which, for our purposes, will be at the resonant frequency [87, 88].

Phase-Locked Loop

We can measure the shift in frequency from an input signal $V_i(t)$ (in this case the resonant frequency of the quartz tuning fork) relative to an output signal by using a PLL. Generally speaking, a PLL consists of a phase detector, a voltage controlled oscillator (VCO) and an amplifier, as shown in Fig. 3.8. As the name suggests, this device will measure the phase of an input signal, in this case the phase near resonance of the tuning fork, and compare it with the signal generated by the VCO and will work to match the phases of the two signals. This is done by feeding the error signal from the amplifier $V_e(t)$, to the VCO and then feeding back to the phase detector. This causes the VCO to adjust the PLL frequency to the resonator frequency and the PLL locks to the incoming signal. If the difference in the phase between the input signal and the fed-back signal is zero, then the two are operating at the same frequency. This technique is useful because, for an oscillator with a high quality factor, the relaxation time can be relatively long. Therefore, it is inefficient and impractical to measure the amplitude of oscillations directly and to match that measurement to a given voltage [89].

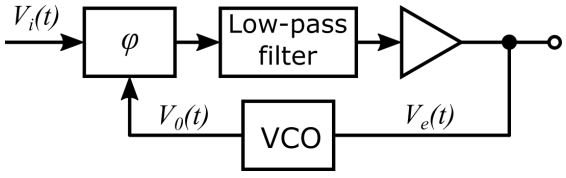

Figure 3.8: Diagram of a phase-locked loop (PLL) consisting of a phase detector, low-pass filter, an amplifier a voltage controlled oscillator (VCO) in a feedback loop.

3.4 NSMM in the Quantum Regime

Having reviewed classical NSMM we now move on to discuss the physics of a quantum NSMM. We have established that a superconducting thin-film resonator would be an ideal candidate as the microwave NSMM probe. With this, we can move on to discussing the physics behind how our NSMM resonator probe can coherently interact with a two-level quantum system when it operates in the single photon regime. We will also present some simulations of the interaction between an NSMM probe and material TLS defect, that are each modelled as an electromagnetic cavity and a generic two-level quantum system respectively.

3.4.1 Jaynes-Cummings Model

To understand the interaction of the resonator probe with an individual quantum two-level system it becomes useful to use the Jaynes-Cummings Model. This model quantises the electromagnetic field in the atom-light interaction instead of describing a classical electromagnetic field such as $\mathbf{E}_0(t) = E_0 \exp(\pm i\omega t)$. The Jaynes-Cummings model assumes that the field in the resonator can be considered as quantum harmonic oscillator with the basis states $\{|n\rangle, n = 1, 2, 3...\}$ corresponding to the number of photons populating the resonator. The Hamiltonian for the full atom-field system can be written as

$$\hat{H} = \hat{H}_{\text{osc}} + \hat{H}_{\text{TLS}} + \hat{H}_{\text{int}}. \tag{3.10}$$

The individual contributions to the total Hamiltonian are

$$\hat{H}_{\text{osc}} = \hbar\omega_r \left(\hat{a}^\dagger \hat{a} + \tfrac{1}{2}\right) \tag{3.11}$$

which is the quantum harmonic oscillator used to model the quantised electromagnetic field, either adding or removing an individual photon to or from the cavity. Here, ω_r is the resonant frequency of the resonator. The next term

$$\hat{H}_{\text{TLS}} = -\tfrac{1}{2}\hbar\omega_{\text{TLS}}\hat{\sigma}_z \tag{3.12}$$

is the general Hamiltonian for a quantum two-level system, whether that be a qubit or a material TLS defect. Where $\hbar\omega_{\mathrm{TLS}}$ is the energy gap of the TLS. Finally, the interaction Hamiltonian

$$\hat{H}_{\mathrm{int}} = \hbar g(\hat{a} + \hat{a}^{\dagger})(\hat{\sigma}_{+} + \hat{\sigma}_{-}) = \hbar g(\hat{\sigma}_{+}\hat{a} + \hat{\sigma}_{-}\hat{a}^{\dagger}) + \hbar g(\hat{\sigma}_{+}\hat{a}^{\dagger} + \hat{\sigma}_{-}\hat{a}) \tag{3.13}$$

where g is the coupling frequency, and $\sigma_{\pm} = \sigma_x \pm i\sigma_y$. The first set of parentheses in the interaction Hamiltonian, $\hbar g(\hat{\sigma}_{+}\hat{a} + \hat{\sigma}_{-}\hat{a}^{\dagger})$, is the on resonance part of the interaction where a photon is absorbed and the TLS is excited, $\hat{\sigma}_{+}\hat{a}$, and the opposite case where the TLS relaxes to the ground state and a photon is emitted, $\hat{\sigma}_{-}\hat{a}^{\dagger}$. The second set of parentheses is the off resonance, rapidly oscillating 'counter-rotating' part. This term can be disregarded in what is known as the Rotating Wave Approximation (RWA). This is justified because on time-scales of the order of the near-resonance interaction, these oscillations will quickly average to zero. This leaves

$$\hat{H} = \hbar\omega_r \left(\hat{a}^{\dagger}\hat{a} + \tfrac{1}{2}\right) - \tfrac{1}{2}\hbar\omega_{\mathrm{TLS}}\hat{\sigma}_z + \hbar g \left(\hat{\sigma}_{+}\hat{a} + \hat{\sigma}_{-}\hat{a}^{\dagger}\right). \tag{3.14}$$

This final Hamiltonian describes the full resonator-TLS system coupled to a transverse quantised field with a frequency close to resonance.

3.4.2 Dispersive Regime

We define a so-called detuning frequency given by $\delta\omega = \omega_{\mathrm{TLS}} - \omega_r$. Now consider the case where $|\delta\omega| \gg g$, meaning the resonator is far detuned from the TLS, though not so far that the RWA is no longer valid, that is the resonator frequency is still on the order of the TLS frequency $\omega_r \sim \omega_{\mathrm{TLS}}$. This is called the dispersive regime. The coupling term can be eliminated by applying a unitary transformation of the form

$$\hat{U} = \exp\left(\frac{g}{\omega_{\mathrm{TLS}}}\left(\hat{\sigma}_{+}\hat{a} - \hat{\sigma}_{-}\hat{a}^{\dagger}\right)\right) \tag{3.15}$$

to the Jaynes-Cummings Hamiltonian. Ignoring damping terms and expanding to second order in g, the diagonalised total Hamiltonian [90, 91] yields

$$\hat{H}_{\text{total}} = \hat{U}\hat{H}\hat{U}^{\dagger} \approx -\frac{\hbar}{2}\left(\omega_{\text{TLS}} + \frac{g^2}{\delta\omega}\right)\hat{\sigma}_z + \hbar\left(\omega_r + \frac{g^2}{\delta\omega}\hat{\sigma}_z\right)\hat{a}^{\dagger}\hat{a}. \tag{3.16}$$

This result states that there will be a frequency shift of $\pm g^2/\delta\omega$ of the resonator depending on the state of the two-level quantum system. This is significant as it means we can perform non-demolition state readout of a TLS, that is it will allow us to perform repeated measurements on observables of the quantum system without disturbing its value. The result also implies that, by coupling to a resonator, there is an AC Stark shift in the TLS transition energy [18]. The dependency of Eq. (3.16) on the photon number has been removed in this approximation and so is valid for photon numbers in the resonator n below some critical photon number given by $n < n_c = \omega_{\text{TLS}}^2/4g^2$ [19, 92]. For larger photon numbers a dressed states formalism can be used to derive the frequency response.

3.4.3 Simulations of NSMM-TLS Interaction

The interaction between a material TLS defect and a superconducting resonator NSMM probe, depicted by the diagram in Fig. 3.9, can be simulated using the open-source Python library "QuTip: Quantum Optics Toolbox" [93, 94]. This approach assumes that the resonant probe can be modelled as an electromagnetic cavity that can be described as a quantum harmonic oscillator. The simulations are based on work by T. Lindström in Ref. [95] and Ref. [45]. These articles show simulations of a superconducting resonator cavity strongly coupling to a qubit and discuss the physics that describe the interaction. We expand on this work by calculating the coupling strength between the resonator-TLS system

$$g(\mathbf{r}) = \frac{e}{\hbar\pi}\mathbf{E}(\mathbf{r}) \cdot \mathbf{d}, \tag{3.17}$$

across a 2-D map and modelling the interaction of a cavity (resonator) as it is moved to different positions above a two-level system. Here, $\mathbf{E}$ is the electric field at the material TLS defect, $\mathbf{d}$ is the electric dipole moment of the material TLS

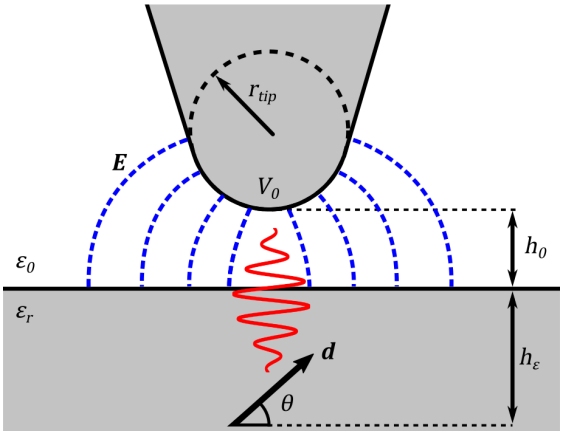

Figure 3.9: Diagram of the NSMM-TLS interaction via a single photon (shown in red) that was used in the simulations. Here we can define a tip-to-TLS distance $h = h_0 + h_\epsilon$. The TLS dipole couples to the electric field **E**, (blue dashed lines) about the tip at the angle θ relative to the z-axis.

defect and **r** is the tip-to-TLS vector. The functional form of **E** cannot be precisely calculated analytically. The discussion in Appendix A discusses in greater detail how this electric field is calculated.

The coupling needs to be calculated at each point as the tip is scanned across the surface because the simulations use the full Hamiltonian for the interaction between the resonator and the TLS which can be described by the Jaynes-Cummings model, the Hamiltonian for which is written in Eq. (3.14). This Hamiltonian assumes that the RWA is valid. This can then be used in calculating the power spectrum

$$S(\omega) = \frac{1}{2\pi} \int_{-\infty}^{\infty} e^{i\omega\tau} \langle \hat{a}^\dagger(\tau + t)\hat{a}(t)\rangle d\tau, \tag{3.18}$$

of the resonator probe. By calculating the frequency shift of the probe, a 2D map of an expected microwave scan of a TLS coupling to our resonator probe can be produced. The full calculation of Eq. (3.18) can be done with the use of in-built functions in the QuTip Python library but further details of the calculations are discussed in Appendix A.

In Fig. 3.10 we show four such simulations. Using the NSMM-TLS diagram in Fig. 3.9 as a reference, in these simulations a two-level system was placed at the origin of the 2-D map spanning the x and y plane and the resonator, with a

resonant frequency of 6 GHz, is positioned at $z = h_0 = 1$ nm above the sample surface. A material TLS defect, with a splitting frequency also of 6 GHz and dipole moment of 3 eÅ, was embedded at $h_\varepsilon = 1$ nm in the dielectric. Thus making the vertical distance from the NSMM tip to the centre of the TLS dipole $h = 2$ nm. We show the coupling strength over the 2-D map for two different dipole angles θ, relative to the z-axis. The coupling strength g, is calculated using Eq. (3.17) for the case in Fig. 3.10(a) when the dipole is parallel to the z-axis ($\theta = 90°$) and as well in Fig. 3.10(b) but when the dipole is perpendicular to the z-axis ($\theta = 0°$). As would be expected, the maximum value of the coupling strength for the case when the dipole is perpendicular to the probe is much less

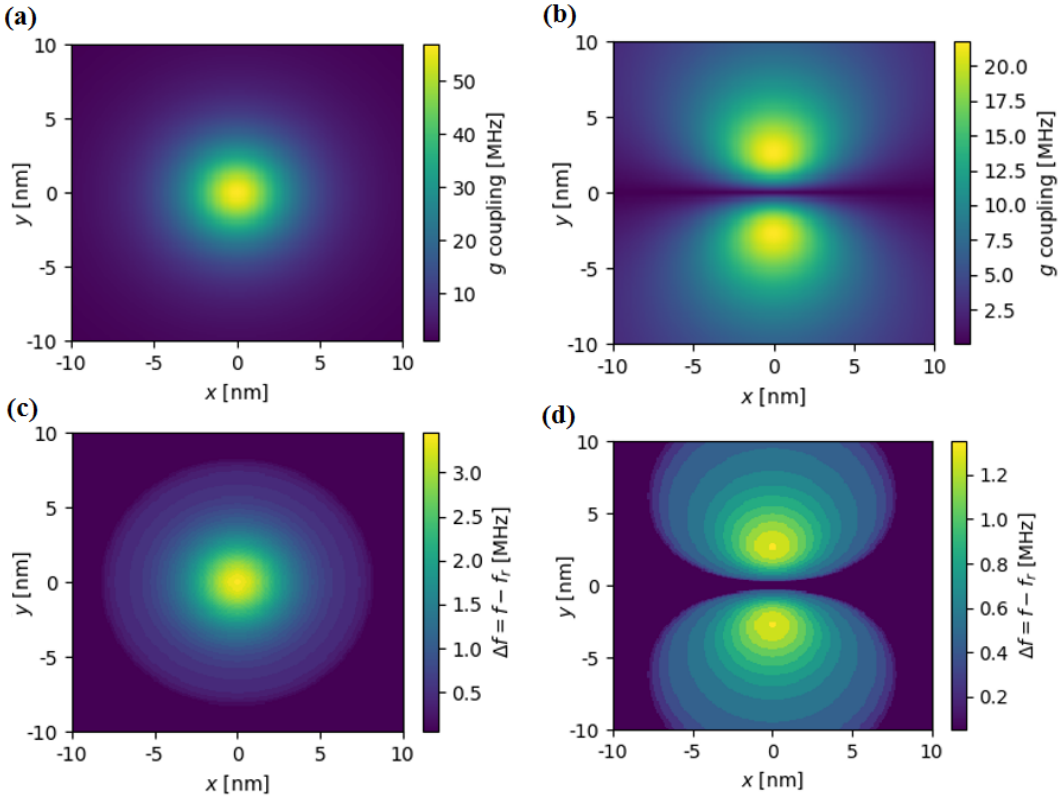

Figure 3.10: Simulations for the interaction between and NSMM resonator probe and a dipole TLS. The first two plots show a map of the coupling strength g, for the case when the dipole is **(a)** parallel to the probe and **(b)** perpendicular to the probe. The second two plots show the dispersive frequency shift of the resonator probe Δf, calculated using the QuTip library for the cases when the dipole is **(c)** parallel to the probe and **(d)** perpendicular to the probe.

than for the parallel case. We then performed simulations utilising the QuTip library to calculate the power spectrum $S(\omega)$, that is defined in Eq. (3.18). From this, we can calculate the dispersive frequency shift due to a coherent coupling of the resonator to the two-level system and plot that across a 2-D map. This is shown in Fig. 3.10(c) for the case when the dipole is parallel to the tip and again in Fig. 3.10(d) when the dipole is perpendicular to the resonator. The simulations take into account dissipation of the whole quantum system to the environment through three different loss channels (discussed in more detail in Appendix A). For these simulations, these dissipation channels had the following values: the resonator probe loss rate $\kappa = 1$ MHz; the relaxation rate from the first excited state to the ground state of the TLS $\gamma_1 = 5$ MHz; and the pure dephasing rate of the TLS $\gamma_\phi = 10$ MHz. These values were chosen such that the resonator-TLS system is in the so-called strong coupling regime where the coupling strength is much larger than the relaxation rate and dephasing rate of the TLS, written as $g \gg \kappa, \gamma_1$. The loss rate of the resonator can be calculated by $\kappa/2\pi = \omega_r/Q$, where Q is the quality factor of the resonator. This means the resonator would have $Q \sim 10^5$. This is similar to the values of the resonator probes that are used in the experiments in this thesis, the results of which are in Chapter 6. As the value for g is at a maximum when $\theta = 0$, we would expect to see a greater dispersive frequency shift when the TLS dipole is parallel to the z-axis. This is indeed what we observe in Fig. 3.10. These simulations show that, if a material TLS defect were to be coupled to using an NSMM with a superconducting resonator probe, we would see a 'bright spot' in the scan that corresponds to a frequency shift on the order of megahertz. It is worth pointing out that these simulations use ideal parameters for *e.g.* the loss channels, the material TLS defect position and its splitting frequency. In reality, it would be possible but relatively unlikely that a material TLS defect with such properties would be found with such favourable parameters and, as such, if coupling were to occur, would likely be smaller than those values presented in Fig. 3.10. The simulations also assume that there would only be a single, isolated material TLS defect with no others around it or close by in frequency that could coherently couple to the TLS of interest.

Chapter 4

Superconducting Resonators

In this thesis, we present an NSMM with a microwave probe that is a superconducting resonator. This chapter aims to discuss some of the underlying theory for understanding superconducting resonators, a device that is commonly used in quantum circuitry and in the following experiments that are described in this thesis.

First, we introduce the idea of superconducting thin-film microwave resonators, then present some common resonator designs and finally discuss their applications as well as recent research surrounding these devices. To reiterate, the goal is to achieve coherent interaction between the resonator probe and a material TLS defect. Therefore it is important to understand the relevant loss mechanisms of superconducting resonators and their frequency response due to changes in their electromagnetic environment, both classically and quantum mechanically. Finally, we introduce the concept of a fractal superconducting resonator and why it is essential for use in our NSMM.

4.1 Thin-Film Superconducting Resonators

Thin-film superconducting resonators are devices of great interest in the field of solid-state quantum circuit research. The quantum properties of superconducting resonators have been applied to many research areas. In astronomy, for example, arrays of superconducting resonators in microwave kinetic inductance detectors (MKIDs) have been used as single photon detectors [96]. These detectors work by absorbing individual photons with sufficient energy to overcome the Cooper-pair binding energy, $\hbar\omega > 2\Delta$. This causes an increase in quasiparticle density in the superconductor which in turn causes a change in the superconductor's surface impedance. This change can be detected by measuring the frequency shift δf

of the resonator [97]. Superconducting circuits have also been used as quantum simulators. Resonators can be used as on-chip cavities for microwave modes and to couple to qubits. Arranging superconducting resonators and qubits into cavity lattices have been used to simulate quantum many-body systems that contain a large number of spins (see [98] for a review). Resonators have also been applied to quantum information processing for the readout of superconducting qubits [99]. Experiments have demonstrated that a coplanar waveguide (CPW) with a sufficiently high Q-factor can coherently couple to two-level quantum systems in the single photon regime [100]. This ability has led to the use of resonators in quantum electrodynamic (QED) circuit experiments such as entangling two superconducting qubits [101], a quantum bus [102] and dispersive qubit readout [103]. By using high-quality crystalline substrates, lower dissipation can be achieved [104]. If we are to reach the single photon regime with NSMM then the microwave probe will need to have a high Q-factor to be capable of coherent coupling to a two-level quantum system. This is to ensure that the rate of loss of photons from the probe does not exceed the average lifetime of a photon within the probe. A superconducting resonator is an ideal candidate for such an NSMM probe as they typically have low rates of loss.

The geometry of three different types of thin-film superconducting resonators are illustrated in Fig. 4.1, each one is capacitively coupled to a transmission line. Figure 4.1(a) shows a meandering distributed $\lambda/2$ coplanar transmission line resonator with each end terminating in an open-circuit, where λ is the wavelength of radiation in the resonator. It is this type of resonator that we will concentrate on throughout the work presented here. Figure 4.1(b) shows a $\lambda/4$ coplanar transmission line resonator. One end of the line is short-circuited, meaning that it is connected to the ground plane of the resonator. Figure 4.1(c) a lumped element resonator consisting of a meandering inductor and an interdigitated capacitor. Structures like these can be fabricated using standard lithographic techniques to etch material away to expose the substrate, producing the single-layer structure. Figure 4.1(a) shows one type of capacitively coupled link between the feedline and resonator. This geometry can be as simple as a small break in an otherwise continuous transmission line or even overlapping interdigitated fingers of varying size [41, 99]. In terms of overall size, a superconducting resonator can be in the

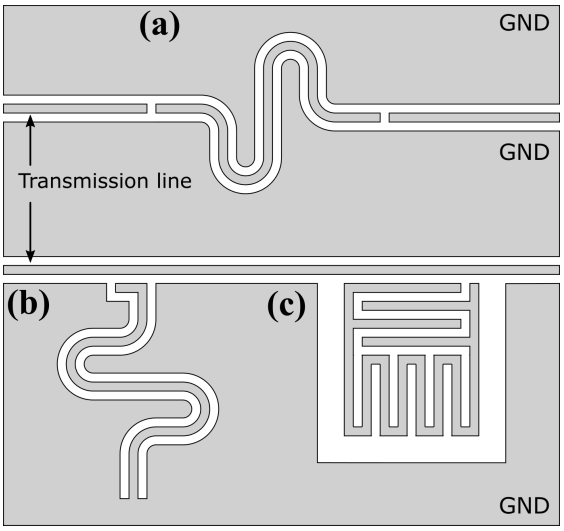

Figure 4.1: Illustrations of three common examples of thin film superconducting resonator geometries. Grey regions are areas of metallisation and the white regions are the exposed underlying substrate. Each resonator is capacitively coupled to a transmission line. **(a)** A meandering distributed open-circuited $\lambda/2$ resonator. **(b)** A meandering distributed short-circuited $\lambda/4$ resonator. **(c)** a lumped element resonator with a meandering inductor and an interdigitated capacitor.

range of 100 µm up to a few millimetres, depending on the choice of resonator geometry needed to support a given wavelength. Capacitive coupling distances between the resonator and the feedline are typically in the range of 10 – 100 µm. The wire width of such transmission line resonators is typically of the order 1 – 10 µm with a thin-film thickness of approximately 100 nm [105]. These dimensions can differ depending on the specific design requirements of a resonator. Having introduced the structure and form of some simple resonator designs to give a sense of their appearance and scale, we can start to discuss their relevance and applications.

4.1.1 Transmission Line Resonator

The geometry of a superconducting coplanar waveguide (CPW) was first shown in Fig. 4.1 and a cross section of this CPW is shown in Fig. 4.2. A central transmission line of width W, and thickness d, is flanked by two semi-infinite ground planes with a gap distance D, either side of the central transmission line. This gap exposes

the underlying substrate with dielectric constant $\varepsilon = \varepsilon' - i\varepsilon''$. The impedance of a such a CPW is given by

$$Z_0 = \sqrt{\frac{R + i\omega L}{G + i\omega C}}, \tag{4.1}$$

where R, L, G and C are the resistance, inductance, conductance and capacitance, per unit length, respectively. If the transmission line is considered to be lossless this reduces to $Z_0 = \sqrt{L/C}$. For the geometry in Fig. 4.2, we can consider a plane wave of the form $Ae^{\gamma y + i\omega t}$ travelling down the central conductor, where

$$\gamma = \sqrt{(R + i\omega L)(G + i\omega C)} = \alpha + i\beta. \tag{4.2}$$

We can turn the CPW into a resonator by making an open ended $\lambda/2$ transmission line, meaning that the boundary conditions are such that the maximum voltage amplitude and the minimum current amplitude are at the open end of the resonator, as shown in Fig. 4.3. If the transmission line has a length l, the impedance can be written as [106]

$$Z_{\text{in}} = Z_0 \coth(\gamma l). \tag{4.3}$$

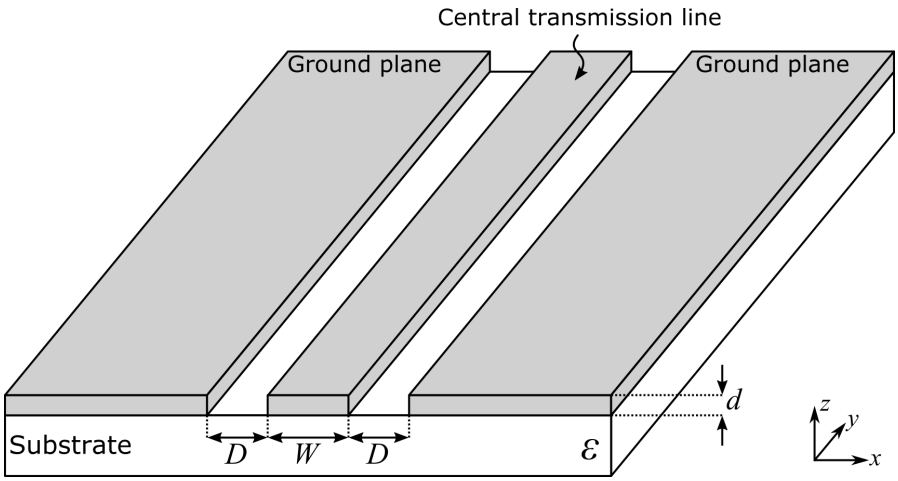

Figure 4.2: A cross section view of the geometry of a coplanar waveguide (CPW) transmission line. The grey areas show metallisation and the white areas are the underlying dielectric substrate. We can define $a = W + 2D$ in this diagram.

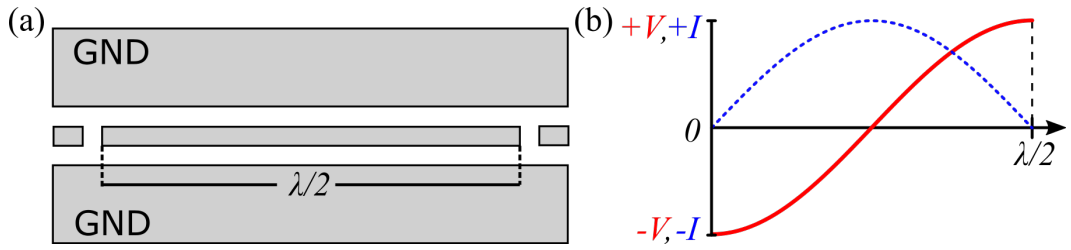

Figure 4.3: **(a)** Illustration of a $\lambda/2$ open-ended resonator flanked by two large ground planes. **(b)** Plot of the voltage (solid red line) and the current (dashed blue line) for a $\lambda/2$ open-ended resonator.

By using the standard identity for the inverse hyperbolic tangent function we obtain

$$Z_{\text{in}} = Z_0 \frac{1 + i\tan(\beta l)\tanh(\alpha l)}{\tanh(\alpha l) + i\tan(\beta l)}. \tag{4.4}$$

Although a superconductor is a good approximation to a lossless line, in reality there are still small losses (discussed in subsequent sections). This means that α is non-zero but small such that we can assume $\alpha l \ll 1$ and therefore that $\tanh(\alpha l) \approx \alpha l$. Now let $l = \lambda/2 = \pi\nu_{\text{p}}/\omega_0$. Here $\nu_{\text{p}} = \omega_0\lambda/2\pi$ is the phase velocity of the travelling wave within a transmission line. Also we can write $\omega = \omega_0 + \Delta\omega$ for small $\Delta\omega$, which is referred to as the detuning angular frequency. Knowing that $\beta l = \omega l/\nu_{\text{p}}$ we can then write

$$\beta l = \pi + \frac{\pi\Delta\omega}{\omega_0}, \tag{4.5}$$

such that

$$\tan(\beta l) = \tan\left(\pi + \frac{\pi\Delta\omega}{\omega_0}\right) = \tan\left(\frac{\pi\Delta\omega}{\omega_0}\right) \approx \frac{\pi\Delta\omega}{\omega_0} \tag{4.6}$$

and substituting Eq. (4.6) into Eq. (4.4) gives the impedance of an open ended transmission line to be

$$Z_{\text{in}} = \frac{Z_0}{\alpha l + i\left(\frac{\pi\Delta\omega}{\omega_0}\right)}. \tag{4.7}$$

Comparing this equation to that of the impedance for a parallel RLC resonator circuit

$$Z_{\text{in}} = \frac{R}{1 + 2iQ\frac{\Delta\omega}{\omega_0}}, \tag{4.8}$$

we can identify the quality factor of the RLC resonator as

$$Q = \frac{\beta}{2\alpha} = \frac{\pi}{2\alpha l} = \omega_0 RC. \tag{4.9}$$

Similar expressions can be derived for a short-circuited transmission line and for $\lambda/4$ resonators by going through the same mathematical process but considering the relevant form for the initial impedance of the resonator design. The boundary conditions differ to those described in Fig. 4.3. For a shorted resonator the voltage is zero and the current is at a maximum at the shorted end of the resonator [106].

4.1.2 The Scattering Matrix

Superconducting resonators can be designed to have resonant frequencies on the order of gigahertz, placing them in the microwave region of the electromagnetic spectrum. The microwave signals passing through a resonator can be described in the framework of a microwave network, for which we introduce the concept of the so-called scattering parameters. We can describe the incident, transmitted and reflected microwaves on a device in terms of a scattering matrix S. For a device with n-ports, reflected voltages of V_i^+ and incident voltages V_j^-, the scattering matrix can be written as [106]

$$\begin{pmatrix} V_1^- \\ V_2^- \\ \vdots \\ V_n^- \end{pmatrix} = \begin{pmatrix} S_{11} & S_{12} & \cdots & S_{1n} \\ S_{21} & S_{22} & \cdots & S_{2n} \\ \vdots & \vdots & \ddots & \vdots \\ S_{n1} & S_{n2} & \cdots & S_{nn} \end{pmatrix} \begin{pmatrix} V_1^+ \\ V_2^+ \\ \vdots \\ V_n^+ \end{pmatrix} \tag{4.10}$$

where a specific matrix element is calculated using the ratio of the incident to reflected voltages such that

$$S_{ij} = \frac{V_i^-}{V_j^+}. \tag{4.11}$$

A 2-port vector network analyser (VNA) can be used to measure a resonator. This means that assuming port 1 is the port with the incident wave, then S_{11} is the measured reflection from the incident port and that S_{21} is the signal transmitted from port 1 to port 2 of the network.

4.1.3 Inductively Coupled Resonator

To measure the transmission (or reflection) through a resonator, it needs to be coupled to a feed-line with an input and an output. In the NSMM we need to ensure that the feed-line is mechanically isolated from the resonator. We do this by choosing to inductively couple to the NSMM resonator probe.

As a simplified case we can derive the S_{21} scattering component of a resonator that is inductively coupled to a transmission line. Figure 4.4 shows the geometry of such a layout. This diagram also illustrates how the resonator can be modelled as a series RLC circuit coupled to a transmission line with mutual inductance M. Starting with a simple RLC circuit, the impedance of the resonator can be written as

$$Z_r = R + i\omega L + \frac{1}{i\omega C} = R + i\left(\omega L - \frac{1}{\omega C}\right), \tag{4.12}$$

where $\omega = 2\pi f$ is the angular frequency. When the system is on resonance the inductive and capacitive reactances cancel one another out, $\omega_0 L = 1/\omega_0 C$. Therefore the impedance becomes wholly real and we can express the resonance frequency as $\omega_0 = 1/\sqrt{LC}$. A lossless transmission line has characteristic impedance $Z_0 = \sqrt{L/C}$, which is a good approximation for a superconducting resonator. The quality factor can then be written as $Q_i = Z_0/R$. Therefore we can write the

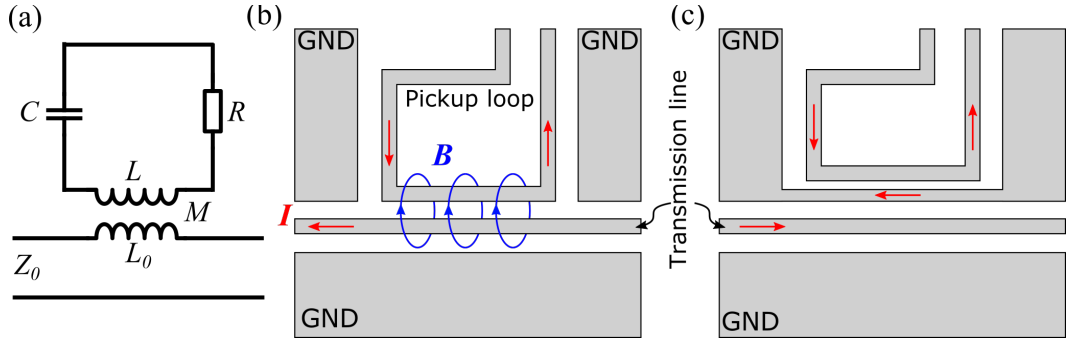

Figure 4.4: **(a)** The lumped element circuit model of an inductively coupled resonator. **(b)** The loop-like geometry of an inductively coupled resonator. Here, the grey area is the thin film superconducting metal and the white areas are the underlying exposed dielectric substrate. Magnetic field lines are shown in blue and the current is shown in red. **(c)** Geometry with a connecting piece of ground plane between the loop and transmission that is discussed in the text.

resonator impedance as

$$Z_r = R + i\left(\omega_0 L\frac{\omega}{\omega_0} - \frac{1}{\omega_0 C}\frac{\omega_0}{\omega}\right) = R + iZ_0\left(\frac{\omega}{\omega_0} - \frac{\omega_0}{\omega}\right). \tag{4.13}$$

Then by substituting in Q_i we get

$$Z_r = R\left(1 + iQ_i\left(\frac{\omega}{\omega_0} - \frac{\omega_0}{\omega}\right)\right). \tag{4.14}$$

Close to resonance we can set $\omega = \omega_0 + \Delta\omega$. Now substituting this into Eq. (4.14), noting that $\Delta\omega/\omega_0$ is small and by using the Taylor expansion of the function $1/(1+x) = 1 - x + \mathcal{O}(x^2)$ while neglecting higher order terms, one finds

$$Z_r = R\left(1 + 2iQ_i\frac{\Delta\omega}{\omega_0}\right). \tag{4.15}$$

Now we consider the whole circuit that is shown in Fig. 4.4(a) and derive a full expression for the impedance for the inductively coupled resonator transmission line system. This takes into account the mutual inductance M, and the inductance of the coupling loop L_0, of the transmission line. The equation for the impedance as seen from the input for this circuit is [107]

$$Z_{\text{in}} = i\omega L_0 + \frac{\omega^2 M^2}{Z_r}. \tag{4.16}$$

The first term of this equation can be neglected when near the resonance frequency. Thus the input impedance becomes

$$Z_{\text{in}} \approx \frac{\omega^2 M^2}{R\left(1 + 2iQ_i\frac{\Delta\omega}{\omega_0}\right)}. \tag{4.17}$$

Now that an equation for Z_{in} has been derived, it can be substituted into the following expression [106]

$$S_{21} = \frac{2Z_0}{2Z_0 + Z_{\text{in}}}, \tag{4.18}$$

which is the transmission for a 2-port network with series impedance. Z_0 is the characteristic impedance defined in Eq. (4.1). Performing the substitution yields

the result

$$S_{21} = 1 - \frac{1 - S_{21,\min}}{1 + 2iQ_i\frac{\Delta\omega}{\omega_0}} \tag{4.19}$$

where

$$S_{21,\min} = \frac{1}{1 + Q_i/Q_c}. \tag{4.20}$$

$S_{21} = S_{21,\min}$ at resonance ($\omega = \omega_0$) and the total quality factor Q, is defined as

$$\frac{1}{Q} = \frac{1}{Q_c} + \frac{1}{Q_i}, \tag{4.21}$$

where Q_c is the coupling quality factor. Equation (4.19) shows the functional form of an ideal transmission response of an inductively coupled resonator circuit where the impedance at the input and the output are matched. However, it is not always the case that such a circuit will be perfectly impedance matched. A mismatch leads to asymmetry in the resonance shape. Analytical work that was done by Khalil *et. al.* [108] shows that this asymmetry can be described by a rotation by φ in the complex plane. This yields the final result

$$S_{21} = 1 - \frac{(1 - S_{21,\min})e^{i\varphi}}{1 + 2iQ_i\frac{\Delta\omega}{\omega_0}}. \tag{4.22}$$

This expression is identical to that of a capacitively coupled resonator, where Q_c is instead a function of the coupling capacitance between the feedline and resonator, rather than the mutual inductance M, as defined above [106]. This means the same expression can be used to analyse both capacitively and inductively coupled resonator. In this work, we are mainly concerned with inductively coupled resonators. We can express the inductive coupling quality factor in terms of the mutual inductance as

$$Q_c = \frac{2Z_0Z_r}{\omega_0^2M^2}. \tag{4.23}$$

The geometry determines the mutual inductance M, and usually requires a numerical simulation to determine the value of M. For example, see the geometry that is shown in Fig. 4.4(c). There is a thin piece of grounded conducting material going between the transmission line and the inductive loop. This induces a current in the opposite direction to the main transmission line which effectively screens

the resonator. The effective coupling as seen by the resonator is reduced but gives the advantage that it becomes easier to choose some arbitrary coupling quality factor when designing a resonator. Having this extra ground line also improves the Q-factor as it acts as a short so that microwave currents in the ground plane can circulate around the resonator. This reduces electrical dipole radiation losses.

Now that we have an analytical expression for the S_{21} through a resonator, as described by Eq. (4.22), we can to plot the magnitude and phase as a function of frequency. This is shown in Fig. 4.5(a-c) for various coupling conditions. The individual curves show the condition for cases of under-coupling ($Q_c > Q_i$), critical coupling ($Q_c = Q_i$) and over-coupling ($Q_c < Q_i$). In these plots, the resonance frequency is set to be 6 GHz with a $Q_i = 3 \times 10^5$. The cases for under-coupling and over-coupling set Q_c at 2.5 times lower and larger than Q_i, respectively.

We notice that at resonance the imaginary part of S_{21} goes to zero and the response is purely real. This is the case when $S_{21} = S_{21,\text{min}}$ and the gradient of the phase about this point is at its steepest. It should be noted that this is the response for the specific case of a $\lambda/4$ CPW resonator measured in transmission. Other geometries, although similar, are not the same. The theses of [96, 109] demonstrate the response for other resonator geometries.

We recall that we added an extra phase factor φ, to account for resonance asymmetries in Eq. (4.22). The effects of varying this phase angle can be seen in Fig. 4.5(d-f) where $|S_{21}|$ and $\angle S_{21}$ have been plotted as a function of frequency. The complex plot in Fig. 4.5(f) shows the rotation of the resonance circle about the point $1 + 0i$ by an angle φ. A full analysis of this resonance curve [108] shows that an asymmetric S_{21} will also reduce the diameter of this circle by a factor of $1/\cos(\varphi)$. This means that simply rotating this resonance circle to fit for the quality factors alone would be an inaccurate method without also taking into account this diameter reduction.

Numerous factors may cause asymmetry in the resonance curve. A likely cause is due to the mismatch of the impedance of the input and output lines [110]. Other spurious resonant profiles close to the frequency of interest can also couple to the primary resonance mode and cause an asymmetric response.

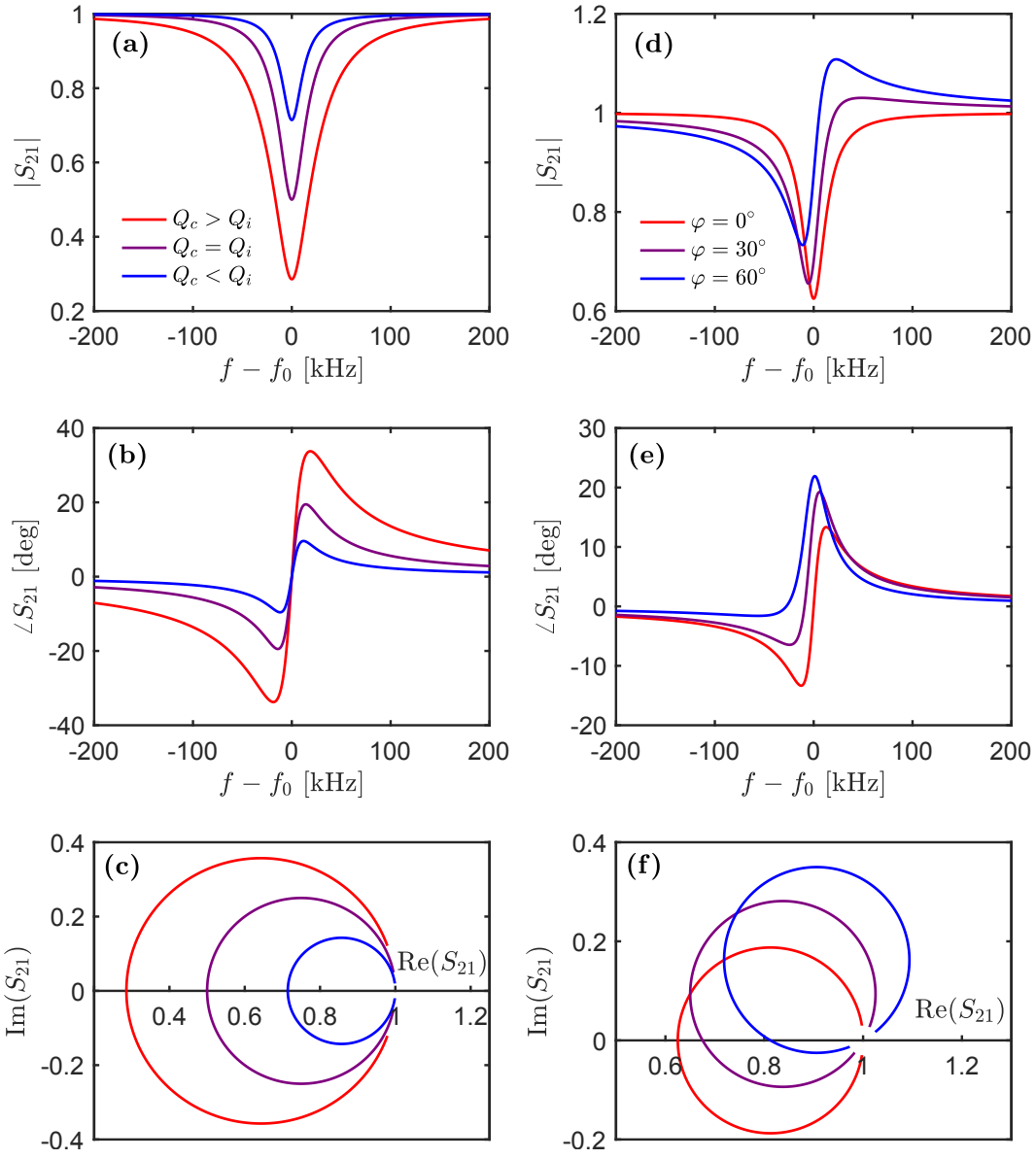

Figure 4.5: Plots showing the S_{21} transmission through a superconducting resonator with $\omega_0/2\pi = f_0 = 6$ GHz, as described by Eq. (4.22). The first three plots show **(a)** the magnitude, **(b)** the phase and **(c)** the complex plane of the S_{21} scattering parameter for three different coupling regimes. The internal quality factor is set to $Q_i = 3 \times 10^5$ for these plots. The next three plots show **(d)** the magnitude, **(e)** the phase and **(f)** the complex plane of the S_{21} scattering parameter for three different values of the phase asymmetry angle φ. The internal and coupling quality factors are set to $Q_i = 3 \times 10^5$ and $Q_c = 5 \times 10^5$, respectively, for these plots. The above stated resonance frequency and quality factors are typical values for the superconducting resonators used in this work.

4.1.4 Average Photon Occupancy

To be able to coherently couple a resonant probe to an individual TLS using NSMM, we need to operate at low powers such that, on average, only one photon occupies the resonator. It is possible to deduce the average number of photons that occupy a resonator by considering the microwave power supplied to that resonator. First, by assuming that the input microwave line, the resonator and the output line act as a 3-port microwave network [109], the proportion of the internal power of the resonator to the input can be written as

$$\frac{P_{\text{int}}}{P_{\text{input}}} = \frac{2}{\pi}\frac{Q^2}{Q_c}\frac{Z_0}{Z_r} \tag{4.24}$$

where P_{int} is the power of the standing wave microwave in the resonator and Q and Q_c are the total and coupling quality factors, respectively. Typically the characteristic impedance $Z_0 = 50\ \Omega$ for standard coaxial lines. It is often reasonable to assume that $Z_0/Z_r = 1$ when calculating this ratio, as most resonators are designed to have an impedance of $Z_r = 50\ \Omega$. Now, by noting that $P_{\text{int}} = \omega_0 E_{\text{int}}$, we can write

$$\langle E_{\text{int}} \rangle = \frac{2}{\pi}\frac{Z_0}{Z_r}\frac{Q^2}{Q_c}\frac{P_{\text{input}}}{\omega_0}. \tag{4.25}$$

Dividing this equation by the energy of one photon $E = \hbar\omega_0$, leads to the final equation of the average photon occupancy of the resonator

$$\langle n \rangle = \frac{\langle E_{\text{int}} \rangle}{\hbar\omega_0}. \tag{4.26}$$

As an example, the resonators used throughout the experiments described in this thesis have a resonant frequency of 6 GHz with $Q \sim 10^5$ and $Q_c \sim 10^6$. Then the required power supplied to the resonator would need to be $P_{\text{input}} = -136$ dBm ($\equiv$ 25 aW) to reach the single photon regime. We can find what P_{input} is by measuring the attenuation from room temperature down to the resonator. Using a VNA we can supply a signal with an arbitrary value so that the total power being input to the resonator is -136 dBm.

4.2 Loss Mechanisms

The figure of merit when describing resonators is usually the quality factor Q. This is a dimensionless quantity that is the ratio of the total energy stored within the resonator and the amount of energy that is dissipated per cycle of oscillation. So far we have considered the internal quality factor of the resonator as an individual source of loss when deriving expressions for the transmission through a resonator. In reality, however, there are separate constituent contributions that must be considered when analysing loss mechanisms in resonators.

The reciprocal of the internal quality factor (recall that $Q^{-1} = Q_i^{-1} + Q_c^{-1}$ from Eq. (4.21)) can be expressed as the reciprocal sum of the individual loss contributions so that we can write the dominant sources of loss as

$$\frac{1}{Q_i} = \frac{1}{Q_{\mathrm{TLS}}} + \frac{1}{Q_{\mathrm{rad}}} + \frac{1}{Q_\sigma} + \text{Other...} \tag{4.27}$$

Where Q_{TLS} is the dielectric loss due to TLS defects, Q_{rad} is the contribution from radiative losses and Q_σ is losses from surface resistivity and kinetic inductance. Theses contributions are discussed in more detail in the following subsections. Other forms of loss, such as magnetic field induced losses, are considered to be negligible in the work presented here.

4.2.1 Dielectric Losses

Metallic thin-film resonator patterns are fabricated on top of dielectric substrates. These substrates have an associated complex dielectric constant $\varepsilon = \varepsilon' - i\varepsilon''$. The loss tangent is defined as the angle in the complex plane between the real and imaginary components such that $\tan(\delta) = \varepsilon''/\varepsilon'$. This relates to the dielectric quality factor by

$$Q_{\mathrm{TLS}} = \frac{1}{\tan(\delta)}. \tag{4.28}$$

The loss tangent gives a measure of the overall dissipative dielectric loss but little physical understanding of the origin and source of this loss.

The widely accepted model for dielectric loss within superconducting resonators and other quantum devices that have been identified in the literature is the ex-

istence of material defects that behave as fluctuating quantum two-level systems (TLS). The effects of these material TLS defects are dominant at low power (single photon energies) and low temperatures and appear to be mostly located at the interfaces between the metal, substrate and air [12, 39, 111, 112]. Investigations into dielectric losses of superconducting resonators at varying temperatures show that counter to what one would expect, there is an optimum temperature, at which, the losses are at a minimum and further cooling can show an increase in dissipation [41]. At elevated temperatures, the interacting material TLS defects become thermally saturated. At lower temperatures, the majority of material TLS defects are no longer thermally saturated and can interact with the resonator. Resonant absorption dominates and therefore losses increase at lower temperatures.

Although experiments have been conducted that measure the behaviour of ensembles of material TLS defects [33, 113] their origin and nature remain elusive. Recent studies have shown that desorption of surface spins can reduce the noise in solid-state quantum circuits but only produce a small reduction in the loss [40]. Identifying the source of these dielectric losses are a significant motivation in this project and more information can be found back in Chapter 2.

4.2.2 Radiative Losses

Another source of loss is due to the emission of radiation from the resonator into free space. Typically these losses are negligible for a resonator with a CPW design (see Fig. 4.2). This is due to the screening current that is produced in the ground planes of the CPW. The screening currents are in the opposite direction and have the opposite polarity to the current in the central transmission line, confining the field in the waveguide [114]. This means that increasing the gap distance D, would increase radiative losses. In the limit where $D \gg W$, *i.e.* no ground planes within the vicinity of the central transmission line, the resonator would act as a good antenna rather than a CPW.

The radiative losses can be calculated analytically for the primary mode of resonance in a CPW geometry. For the geometric parameters defined in Fig. 4.2

(recall that $a = W + 2D$), we can use the formula [96]

$$Q_{\text{rad}} = \frac{\pi(1+\varepsilon)^2}{2\varepsilon^{5/2}} \frac{\eta_0}{Z_0} \frac{1}{I'(\varepsilon, n)} \frac{1}{n - \frac{1}{2}} \left(\frac{l}{a}\right)^2 \approx 5.6 \left(\frac{l}{a}\right)^2, \tag{4.29}$$

to calculate the losses. Here, l is the length of the resonator, $\eta_0 = 377\ \Omega$ and the current density $I'(\varepsilon = 10, n)$ is numerically calculated by Barends [109] and is equal to 1.62 for $n = 1$. This formula would result in radiation losses on the order of $Q_{\text{rad}} = 10^6$ - 10^7, for typical values of resonator dimensions. This result shows that radiative losses are negligible when compared to the overall losses of a resonator [19].

4.2.3 Surface Resistivity and Kinetic Losses

Superconductors exhibit zero electrical resistance below their critical current when a DC signal is applied. However, at larger frequencies still below the superconducting energy gap, there is a non-zero surface resistance. By considering the two-fluid model of superconductivity [115] we can obtain an expression for the surface impedance. The two-fluid model assumes that the total carrier density n_t, comprises of the density of normal state quasiparticles n_n, and the density of Cooper-pairs n_s, such that $n_t = n_n + n_s$. For a frequency ω that is much less than the inverse scattering time of the quasiparticles $\omega \ll \tau_n^{-1}$, the complex conductivity can be written as

$$\sigma = \sigma_n + i\sigma_s = \frac{n_n e^2 \tau_n}{m_e} - i\frac{n_s e^2}{m_e \omega}, \tag{4.30}$$

where m_e is the electron mass. Assuming that typical quasiparticle scattering times are of the order $\tau_n \sim 1$ ps means that this is valid for $\omega < 100$ GHz. In the regime where $\omega > \tau_n^{-1}$ then the complex surface impedance can be written as [114]

$$Z_s = \sqrt{\frac{i\mu_0\omega}{\sigma_n + i\sigma_s}} = R_s + i\omega L_s. \tag{4.31}$$

This expression for the surface impedance shows that there is a non-zero real contribution. This brings about dissipation in the superconductor. The imaginary contribution corresponds to an effective inductance due to the kinetic energy of

Cooper-pairs. An expression for the loss due to surface impedance can be derived for finite temperatures [20, 114, 116]. The losses can be written as

$$Q_\sigma = \frac{\omega L_s}{R_s} = \frac{n_s}{n_n} \frac{Z_0}{c\mu_0 \sqrt{\varepsilon_r} \tau_n \omega_0 \lambda_{\text{eff}}^2 g}, \tag{4.32}$$

where Z_0 is the characteristic impedance and is typically 50 Ω, λ_{eff} is the penetration depth of a thin film superconductor and is given by $\lambda_{\text{eff}} = \lambda^2/d$ in the limit where $d \ll \lambda$ where d is the film thickness and λ is the London penetration depth. The parameter g is a geometric factor (defined in terms of the parameters described by Fig. 4.2) found from conformal mapping [116]. Resistive losses are increased at the edges of a CPW because this is where currents are mostly localised. It is worth noting that BCS theory predicts the temperature dependence of such losses. The ratio of quasiparticle to Cooper-pair carrier densities is given by $n_s/n_n = 1 - (T/T_c)^4$, where T_c is the superconducting critical temperature. In the limit where $T \ll T_c$ then these resistive losses become negligible. For the Nb resonators used in this thesis, losses due to surface resistivity are typically small and therefore negligible because the $T_c^{\text{Nb}} \sim 9.3$ K and the NSMM operates at $T = 10$ mK $\ll T_c^{\text{Nb}}$.

4.3 Fractal Superconducting Resonators for NSMM

The superconducting resonators that have been discussed in this chapter so far are relatively large, typically on the order of millimetres. This does not make them particularly ideal as a resonant probe for NSMM and tuning fork AFM as they are too large. The requirements for a resonant probe for application in a cryogenic NSMM are as follows:

- Be small and light enough to fit on to the end of a quartz tuning fork prong without significantly reducing the mechanical Q-factor of the tuning fork.
- A large capacitive network to reduce the microwave propagation velocity so that for the same frequency, the probe becomes smaller and thus fits on to one of the prongs of the tuning fork.

- Have a sharp tip where the voltage anti-nodes of a standing microwave will be located. This ensures higher AFM and NSMM resolution and a more highly concentrated electric field for coupling to TLS dipoles.
- Metallic loop to inductively couple to an external, mechanically decoupled transmission line that will excite/read-out the microwave signal from the probe, reducing the effects of external mechanical vibrations.
- Symmetric design to minimise radiation losses and to ensure the location of the voltage anti-nodes at the probe tip. This means that another 'dummy' coupling loop will be necessary.

If we are to use a superconducting resonator as a resonant NSMM probe then all these criteria must be satisfied.

A superconducting resonator with a fractal design, as shown in works done by S. E. de Graaf [19, 69], has been demonstrated that satisfy all of these criteria. These fractal resonators are ideal candidates to be used as NSMM probes to coherently couple to quantum two-level systems in a cryogenic environment. Additional features of these fractal resonators for NSMM include flux pinning centres in the ground planes of the probe as well as in the electrodes. This helps to reduce any losses due to magnetic fields.

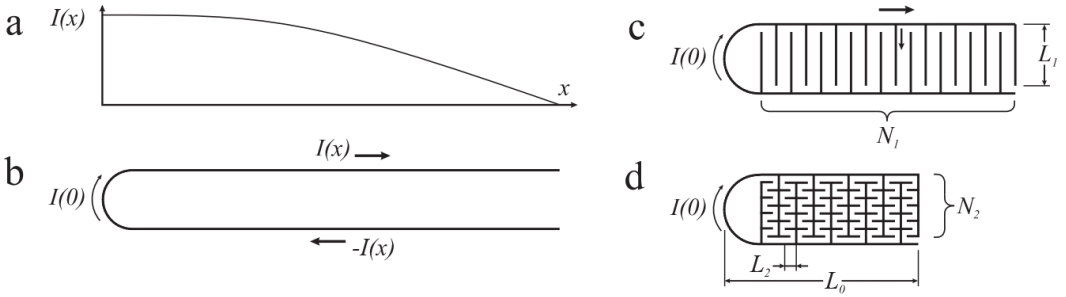

Figure 4.6: **(a)** The current distribution along a single branch in a half wave resonator. **(b)** A half wave resonator where the voltage node, $I(0)$, is located where the branches join. **(c)** First order distributed fractal resonator of equal frequency with N_1 secondary branches. Each carries a current approximately equal to $I(0)/N_1$. **(d)** Second order fractal resonator where each first order branch is loaded with N_2 sub-branches. Relative resonator lengths not to scale. Adapted from [117].

To introduce the concept of a fractal resonator, we consider the current distribution through a "U" shaped $\lambda/2$ transmission line (Fig. 4.6(a) and Fig. 4.6(b)). From the fact that the microwave propagation velocity $v_p \propto 1/\sqrt{LC}$, an increase in inductance or capacitance will reduce the propagation velocity. Figure 4.6(c) shows the first iteration of a fractal resonator by adding interdigitated branches that increase the capacitance of the transmission line. This can be repeated, as shown in Fig. 4.6(d), to create a second-order fractal network that increases the capacitance further. This design also has the effect of reducing the overall length ($l = \lambda/2 = \pi v_p/\omega_0$) and the footprint of the resonator, satisfying another key requirement for the NSMM probe. The fractal design also helps to reduce radiative losses [118].

A resonator probe that makes use of this concept is shown in Fig. 4.7. In this image, the lighter grey regions are areas of Nb where as the darker grey/blue areas are the underlying dielectric substrate, as indicated by the labelled arrows in Fig. 4.7(a). This resonator has made use of the "U" shaped design described earlier in Fig. 4.6, where the whole resonator supports a $\lambda/2$ mode standing wave at 6 GHz. This fractal capacitive network makes the resonator compact and the whole chip is $\sim$ 1 mm in length and can be made lightweight enough to adhere to the prong of a tuning fork. There is also a large area on the left side of Fig. 4.7(a) that is grounded. This area can also be used to bond a thin wire to DC-bias the resonator.

An optical image of the coupling loop is shown in Fig. 4.7(b). There are two loops in this design to maintain symmetry in the two arms of the resonator. The ground plane goes around the loop to help screen the resonator and reduce radiation losses that would occur from an effective dipole moment. Holes in the ground plane encourage flux pinning in these areas that are far from the tip.

A close up image of the third-order fractal capacitive network is shown in Fig. 4.7(c). The resonator is fabricated using a standard electron beam lithography technique. The details of the fabrication process can be found in [19]. The resonator is patterned in Nb on a Si substrate and individual probes are cut from the wafer using deep silicon plasma etching. Both of the arms lead to the tip of the resonator shown in the scanning electron microscope (SEM) image in Fig. 4.7(d).

To achieve the requirement of having a sharp tip we use xenon focused ion

beam (FIB) etching from the backside of the resonator. This prevents damage to the resonator that is patterned on the front side. Milling with the Xe-FIB from the backside (non-metalised side) of the probe has no observed impact on the quality factor of the microwave resonator. The FIB etching process is required for high resolution and high sensitivity NSMM imaging, ensuring the NSMM tip is well defined and that the AFM and metallic NSMM tips are one and the same. One arm is extended slightly further than the other to form the scanning tip. The voltage maxima of the standing wave are located at the tip to ensure the maximum electric field for coupling to the sample.

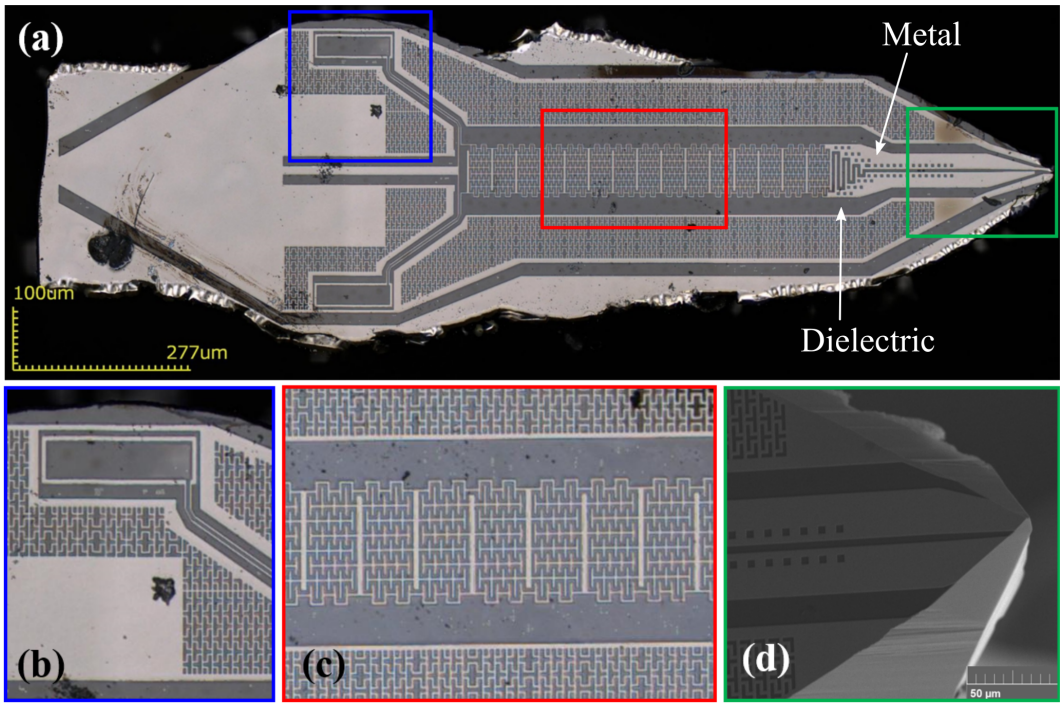

Figure 4.7: **(a)** An optical image of a superconducting microwave fractal resonator that is used as a microwave probe in the project. The chip is made from Nb patterned on a Si substrate and is $\sim$ 1 mm in length. **(b)** A close-up optical image of the coupling loop and the surrounding ground plane. **(c)** A close-up optical image of the third-order capacitive network that reduces the propagation velocity v_p, of the microwaves. **(d)** An SEM image of the resonator probe tip post FIB etching.

Chapter 5

Experimental Set-Up and Measurement Systems

This chapter focuses on the design of our NSMM. It aims to give the reader a better understanding of the experimental set-up of the microscope within the cryogenic dilution refrigerator and the layout of the most significant components relative to one other within the experiment. This will help to provide a clearer context when discussing measurements and data that will be presented in subsequent chapters. The techniques employed to measure the resonator are also explained here as well as a discussion of the fabrication of bespoke qubit samples that were used in the testing of the microscope's capabilities. Also discussed in this chapter is the design of a mechanical low-pass filter suspension system that aims to minimise the effects of external mechanical vibrations, particularly those of the pulse tube which is used in the cooling of the dilution refrigerator.

At this point, it is worth reminding the reader of some of the design requirements of this microscope that makes it unique to other NSMMs that currently exist in the literature at the time of writing. These requirements are

- The need for low temperatures (< 300 mK) so that the condition $\hbar\omega \gg k_B T$ is satisfied so that thermal fluctuations do not saturate any material TLS defects in the sample under investigation.

- The NSMM needs to operate at low microwave powers for coherent interaction of the superconducting resonator with a material TLS defect, as a single photon can saturate a material TLS defect, such that $\langle n \rangle \sim 1$.

These two criteria, along with a suspension system, are necessary if the NSMM is to coherently couple to individual two-level quantum systems.

5.1 Mechanical Suspension

The entire NSMM will need to be housed within a cryogenic dilution refrigerator so that it can be cooled to ultra-low temperatures. This introduces a few design challenges for the NSMM. One such challenge is to minimise the effects of external mechanical vibrations on the system. This is crucial because mechanical vibrations will significantly impact the effectiveness of any distance control method used for scanning and will therefore negatively impact the performance of a coherent NSMM-TLS interaction. In particular, the effect of the dilution refrigerator's pulse tube cooling mechanism is a significant source of vibrations on the system. The operational piston frequency of the pulse tube is $f_{\mathrm{PT}} \sim 1.4$ Hz, so any mechanical low-pass filter design would need to have a cut off frequency lower than the piston frequency of the pulse tube.

Practically speaking, one difficult aspect of installing a suspension system inside a cryostat is that space quickly becomes scarce in the coldest parts of the refrigerator. This is apparent from examining Fig. 5.1 that shows the full cryogenic experimental set-up, including the NSMM. The solution was to place the springs at the 50 K plate of the cryostat and to have Kevlar thread feed down and attach to a copper platform holding the NSMM at the coldest stage. However, doing so means that this will create holes in higher temperature plates, allowing for photons with greater thermal energy to reach the coldest parts of the cryostat. The impact of this was reduced by designing special feed-through channels (shown in Fig. 5.1) with caps that reduce the leakage of these higher energy photons. The insides of these feed-throughs were painted black using stycast to increase the absorption of photons.

The suspension consists of three copper-beryllium (CuBe) springs arranged in triangular geometry at the 50 K plate. CuBe was chosen because of its small thermal contraction rate and its retention of its mechanical properties, such as its spring constant, when cooled. The resonant frequency of a mass on a spring can simply be calculated using $2\pi f_r = \sqrt{k/m}$ where k is the spring constant and m is the mass loaded on the spring. In this case, the Cu mounting plate and the NSMM have a combined mass of approximately 5 kg. The spring constant for all three springs in parallel can be calculated as a function of the material and dimensional

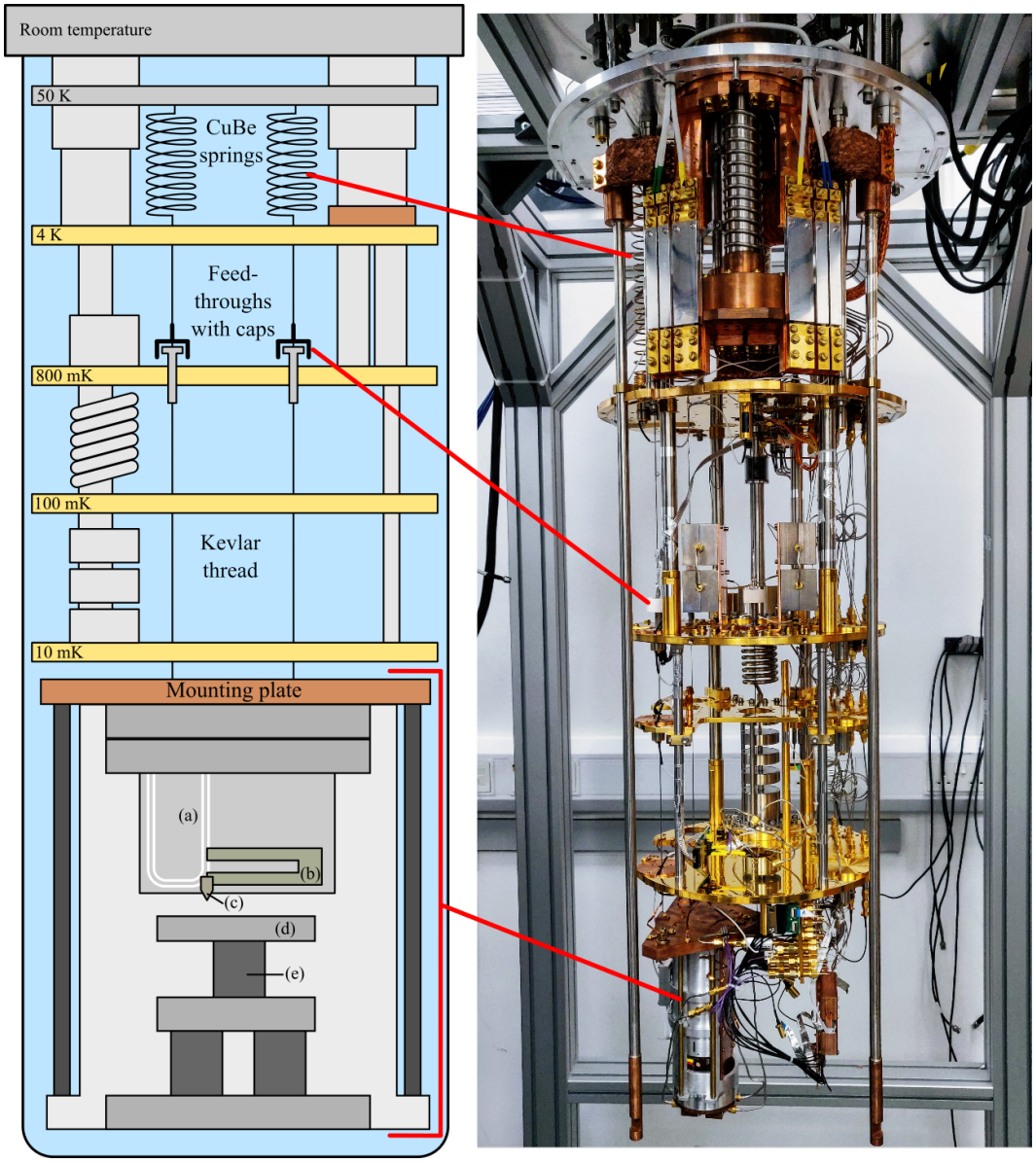

Figure 5.1: *Left:* A not-to-scale schematic layout of the NSMM inside the dilution refrigerator. *Right:* A photograph of the NSMM mounted in the BlueFors dilution refrigerator, open and at room temperature. (a) Coplanar waveguide (CPW) for microwave transmission. (b) Quartz crystal tuning fork for precise distance control. (c) Superconducting microwave resonator tip, glued to the tuning fork and couples to the CPW. (d) Sample stage. (e) Piezo-stack for z-direction approach to the sample. At the top of both images, the CuBe springs that act as mechanical low pass filters can be seen attached to the 50 K plate of the BlueFors refrigerator. The NSMM is also highlighted in both images.

properties of the spring using

$$k = \frac{Ed^4}{8ND^3}, \tag{5.1}$$

where E is the Young's Modulus of CuBe ($\sim$ 125 GPa). Here the spring diameter is $D = 44.5$ mm, the wire diameter is $d = 2$ mm and the total number of turns for our springs was chosen to be $N = 30$. We find a spring constant $k = 295$ N/m for the total suspension ($\sim$ 98.3 N/m for each individual spring) which corresponds to a resonant frequency of $f_{\text{sus}} \sim 1.2$ Hz, which is less than the resonant frequency of the cryostat pulse tube ($f_{\text{sus}} < f_{\text{PT}}$). To further mitigate the effects of vibrations on the experiment, it makes sense to discuss damping and its effect on the frequency response of the system. The amplitude of the oscillations caused by an external force on a harmonic oscillator can be written as

$$A(\omega) = \frac{1/k}{\sqrt{\left(1 - (\omega/\omega_0)^2\right)^2 + \left(2\xi\omega/\omega_0\right)^2}}. \tag{5.2}$$

Here, $\xi = b/2\sqrt{km}$ where b is the linear damping coefficient. Critical damping occurs when $\xi = 1$. This has been plotted in Fig. 5.2 for varying values of ξ. The system that is shown in Fig. 5.1 is damped mainly by the cables that connect directly to the NSMM from the 10 mK plate. As will be shown later, the NSMM

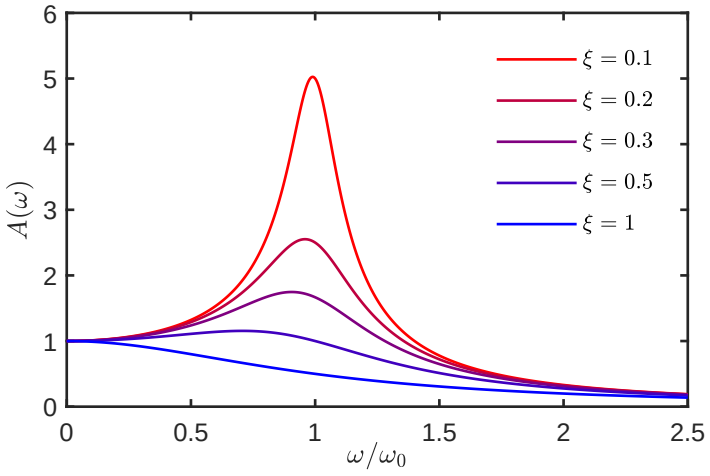

Figure 5.2: Plots of the frequency response for a resonant system for five different damping coefficients. When $\xi < 1$ the system is under-damped, when $\xi > 1$, this system is over-damped and for $\xi = 1$ the system is critically damped.

suspension is damped but not sufficiently damped in the final set-up. Ideally the system would be critically or slightly over damped ($\xi \geq 1$), otherwise, the suspension will help to amplify the effects of the pulse tube. See Fig. 5.2. One way to achieve this level of damping would be to introduce Eddy current dampers to the NSMM suspension system [119].

5.2 Scanner Design

In this section, we will discuss the design of the NSMM itself and explain how the experiment is set-up and discuss how the various components move or interact with one another. Figure 5.3 shows a diagram with an adjacent photograph of the inside of the NSMM casing. In the casing, we show the sample stage, the tuning fork and resonator probe combination, shown in more detail in Fig. 5.4. It is this whole structure that makes up the NSMM inside an aluminium casing. This structure is then suspended - upside down - inside of the cryostat by the three CuBe springs mentioned earlier.

5.2.1 Sample Stage

Figure 5.3 shows a labelled diagram, as well as a photograph, of the inside of the NSMM itself that is attached to the Cu mounting plate and suspended upside down by the CuBe springs and Kevlar thread. The sample stage of the NSMM consists of a small copper sample platform, a solenoid, one piezo-stepper for coarse z direction of movement and five piezo-tubes. One piezo-tube is used for fine distance control in the z-direction of the sample stage and the other four are arranged in a 2×2 formation and are used for fine xy-sample movement when scanning a sample or device under test. There are two more piezo-steppers at the top of the NSMM casing that are for coarse xy-positioning. Not clearly shown in the diagram or photograph is another smaller piezo-stepper that is behind the yellow-coloured CPW. This is used to adjust the coupling between the CPW and the microwave resonator probe by changing the distance between them.

Starting from the two piezo-steppers that are attached at the top of the NSMM casing (see Fig. 5.3), both of these steppers are used for the coarse xy-positioning

of the probe above the sample. These steppers are Attocube ANPx101 and, when supplied with 20 V amplitude saw-tooth pulses, have a measured step-size of 33 nm in each direction at low temperature (< 4 K). This increases to 58 nm when 35 V is applied. These values were measured by scanning a sample that had known feature sizes. The working principle for these steppers is a slip-stick mechanism. A piezo-stick is extended, moving the stepper forward until the peak of the saw-tooth pulse is reached. The voltage quickly goes to zero and the piezo snaps back to its original length. The sudden movement overcomes the static coefficient of friction in the piezo-stepper so that it is not pulled back. The piezo-steppers move the whole mount that holds the CPW with the probe, tuning fork and the

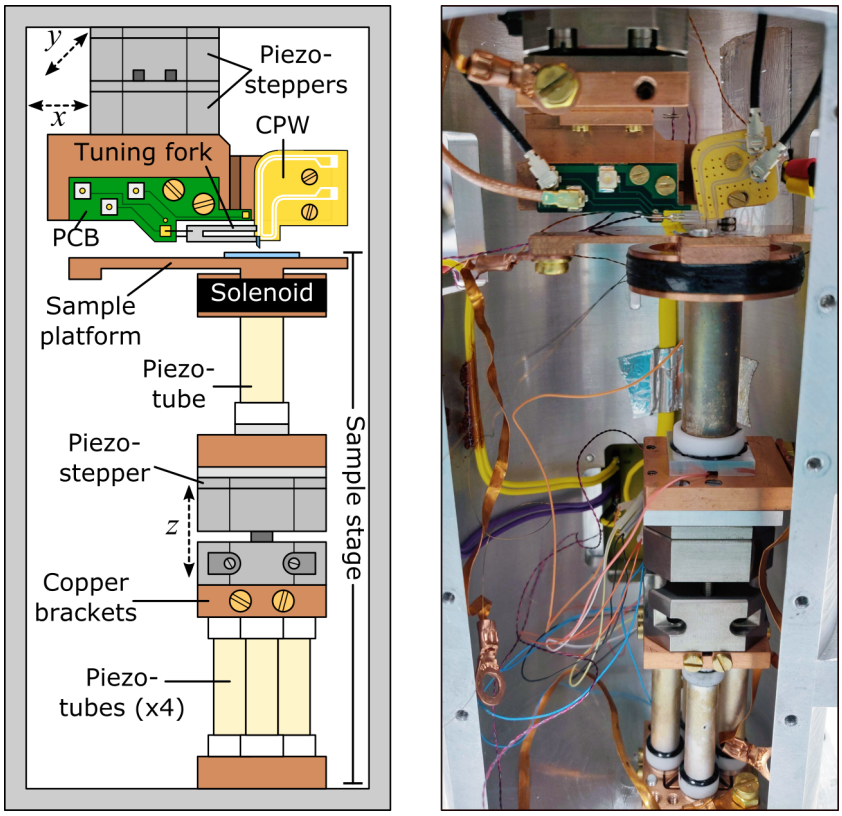

Figure 5.3: *Left:* A labelled diagram of the inside of the NSMM. *Right:* A photograph of the inside of the NSMM, showing the experimental set-up. These images show the sample stage where samples are placed above a solenoid for scanning, piezo-steppers that are used for coarse positioning and piezo-tubes that are used for fine z-approach and scanning.

other smaller piezo-stepper hidden behind the CPW in xy as well. This is so that the CPW-resonator coupling is not changed when moving the probe across a sample. The smaller piezo-stepper behind the CPW is an Attocube ANPz30 and has a quoted step size of 25 nm at room temperature and 10 nm at 4 K at 20 V. This smaller piezo-stepper is much more difficult to calibrate because we do not have an analytical function to describe the CPW-resonator coupling as a function of distance. There is a third stepper in the sample stage column. This is an Attocube ANPz101 piezo-stepper and it controls the coarse z-positioning of the sample stage. This has an estimated approach step size of ~ 48 nm, though this differs when being retracted as (due to being placed upside down in the cryostat) the stepper has to work against gravity.

In the sample stage, there are a total of five piezo-tubes made from a piezoelectric ceramic and coated in a conducting material that acts as the electrode. On the ends of the tubes are white ceramic (Macor) caps that are adhered using stycast epoxy. They are then held in place with custom brackets made from copper so that the thermal expansion is matched between the different materials and does not break or lose grip of the tubes. These tubes are used for the finer positioning control of the sample stage, relative to the probe. The displacement of the piezo-tubes has been measured to be 370 nm/V in xy and 17.7 nm/V in z at room temperature and 42 nm/V in xy and 750 pm/V in z at 80 mK. The calibration was done before adding the feed-through caps for the suspension cable, hence the higher temperature. However, there is no observed change in the calibration factors when cooled to lower temperatures. A single piezo-tube is placed directly under the sample platform and finely tunes the tip-to-sample distance when fed-back with the tuning fork response from a PLL (discussed in Chapter 3). The other four tubes are located towards the bottom of the NSMM casing (see Fig. 5.3) and are arranged in a 2×2 formation. This arrangement tilts the sample in the xy directions so that they align with the directions of the piezo-steppers at the top of the NSMM casing. Each diagonally opposing pair of tubes correspond to one x or y direction of movement. As one extends, the other contracts and this motion 'rocks' the sample when the NSMM is scanning.

At the top of the sample stage is the sample platform. This is made from oxygen-free copper and it extends further out to the side than the stage beneath it

so that it can be thermally anchored to the casing of the NSMM. On this copper plate, samples are adhered using high vacuum Apiezon N grease. The sample platform has a toroidal copper piece directly below it that holds a solenoid that consists of a superconducting wire wound around it that is made from NbTi with a Cu30Ni alloy matrix. The solenoid is then coated in stycast epoxy to hold it in place. The purpose of the solenoid is so that any quantum sample that can be flux biased can be tuned into resonance with the resonator probe.

In Fig. 5.3 we can also see the green printed circuit board (PCB) that the tuning fork is soldered to and also the yellow-coloured PCB that makes up the CPW. The tuning fork PCB is made from layered copper with FR-4 (a woven fibreglass and epoxy resin composite material), a common PCB material that is used in electronics. There are three connectors on this PCB. One for each electrode of the tuning fork and a third connector so that, if needed, the resonator probe can have a thin wire directly bonded to it so that the resonator can be DC biased. The CPW PCB is made from gold plated copper on top of a dielectric (Rogers PTFE laminate) substrate. The CPW has two electrodes, one for the incoming microwave signal and another for the outgoing microwave signal. The central stripline has a width of $W = 200$ µm and a gap distance of $D = 120$ µm at its closest approach to the resonator probe. This is then directly screwed on to the smaller piezo-stepper for adjusting the coupling distance between the CPW and the resonator.

5.2.2 AFM & NSMM Probe

The sample stage and how the sample platform is moved for scanning has been discussed in the previous section. Here, we discuss in more detail the experimental set-up of the NSMM resonant probe and other related scanner components. Figure 5.4(a) shows the layout of the various microscope components.

A superconducting fractal resonator, with resonant frequency $f_r = 6$ GHz, is adhered to the end of the lower prong of a quartz tuning fork using Epo-tek H77 epoxy that is then cured at 150 °C for 1 hour. The tuning fork, with the resonator probe attached, has a resonant frequency in the region of $f_{r,\mathrm{TF}} \sim 29$ - 30 kHz with a Q factor of $\sim 10^4$. This reduction in tuning fork resonance frequency is caused by the added mass of the superconducting resonator probe. The resonator probes

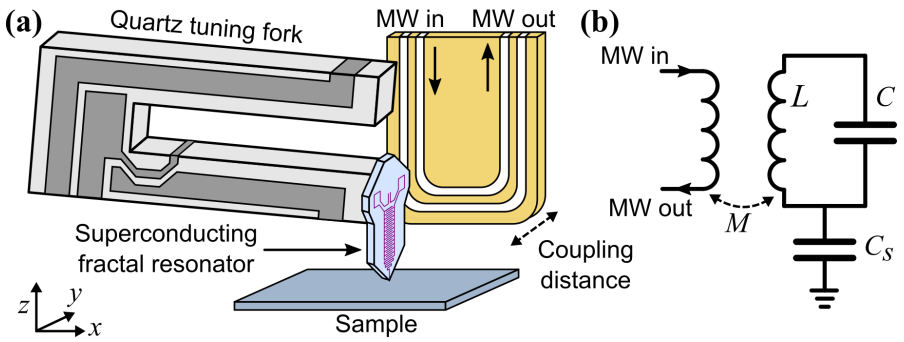

Figure 5.4: **(a)** Diagram of the set-up of the NSMM probe. A superconducting fractal resonator ($f_r = 6$ GHz), with average photon occupancy $\langle n \rangle \sim 1$, is adhered to a quartz tuning fork. A movable CPW is used to adjust the inductive coupling to the resonator for excitation and readout of a microwave signal. **(b)** An equivalent circuit diagram of the NSMM probe set-up where M is the mutual inductance between the resonator and the CPW.

are designed to be small and compact enough to fit on to the end of a tuning fork without hugely altering its quality factor ($Q \sim 10^4$) due to the mass imbalance on the prongs. A detailed optical image of the fractal resonator can be found in Fig. 4.7 at the end of Chapter 4 along with a more in-depth discussion. Once mounted on to a tuning fork, there is need to ensure that there is a well-defined tip. To do this, we use xenon focused ion beam (FIB) etching from the backside of the resonator to mill the tip to the desired size. The FIB step is required for high resolution AFM and microwave imaging by having a well-defined tip and electric field. FIB etching also ensures that the AFM tip and metallic NSMM tips are one and the same. This process has no observed impact on the quality factor of the superconducting microwave resonator.

Figure 5.4(b) shows an equivalent circuit diagram of the experimental set-up shown in the adjacent diagram in Fig. 5.4(a). The resonator is modelled as a LC-circuit and shows a mutual inductance between the resonator and another inductor. This models the inductive coupling between the fractal resonator and the CPW. This ensures that the resonator and CPW are mechanically decoupled from one another. The tip-to-sample interaction can be modelled as a capacitance C_s. This is the capacitance between the metallic tip and the underlying sample. Calculating this capacitance is discussed in more detail in Section 3.2.2 of Chapter 3.

5.2.3 Data Acquisition and Stage Control

We have discussed the various components that make up the NSMM and the whole experiment. Now we briefly look into the methods of data acquisition and how the sample stage is controlled. The operation of the scanning *i.e.* the motion of the piezo-steppers and piezo-tubes, is controlled by a Nanonis SPM controller with piezo-drivers and oscillation control functionality for the tuning fork. Locking to the tuning fork resonant frequency is done with the use of a PLL (as shown and discussed in Fig. 3.8 from Section 3.3.2). The Nanonis control software also acted as a data acquisition toolkit and was able to capture scan data, had an in-built spectrum analyser and tracked tuning fork properties such as the amplitude and phase as a function of frequency.

5.3 Microwave Measurements

In this section, we will discuss the microwave measurement systems used for measuring the properties of the resonator probe. First, we discuss the microwave components that are used in the cryostat that lead directly to the NSMM. This is important when we need to calculate the input power into the resonator probe. We then move on to discuss data acquisition (DAQ) methods by introducing a simple microwave measurement set-up using a vector network analyser (VNA). We then move on to discussing a more complex DAQ set-up known as Pound-Drever-Hall (PDH) locking that can be used for measuring the noise levels of the resonator and accurate real-time monitoring of the resonant frequency while scanning.

As mentioned at the beginning of this chapter, the NSMM must operate at low temperatures, of the order of millikelvin, to be able to coherently couple to a quantum system. This is achieved by suspending the NSMM inside of a BlueFors LD-400 dilution refrigerator. The NSMM also requires ultra-low microwave powers at the superconducting resonator. To aid in achieving low microwave powers, the input microwave line to the NSMM has a large amount of attenuation added to it. The input and output microwave lines are shown in Fig. 5.5. Each temperature stage of the cryostat has also been indicated.

5.3.1 The Cryogenic Microwave Set-Up

Room temperature attenuators can be added to the input line to aid in reducing the microwave power being supplied to the NSMM. Inside the fridge, attenuators are placed at different temperature stages (see Fig. 5.5) totalling −60 dB that are arranged to reduce thermal noise at 30 mK. The microwave line itself is a coaxial cable with a loss that needs to be accounted for. From room temperature down to the lowest temperature section (30 mK) of the cryostat (before flexible microwave cables are used) the total loss of the coaxial cable was measured to be −7 dB at 6 GHz. Between the fixed coaxial cable and the NSMM, flexible microwave cables (SMA to U.FL coaxial cable, 50 Ω) need to be used. This is so that the NSMM suspension is not hindered by a rigid coaxial cable. However, these flexible cables are particularly lossy compared to rigid coaxial cables. The total loss of the flexible microwave cables was measured from the first flexible cable, through the CPW PCB (see Fig. 5.4) then back through to the second microwave cable. The total loss was measured to be ∼21 dB at 6 GHz. Taking half of this value gets ∼10.5 dB loss per flexible microwave cable. Both of these extra losses are taken into account when calculating the power supplied to the resonator later on.

Figure 5.5 shows the output microwave line, which has the second flexible microwave cable coming from the NSMM. The rigid output coaxial line does not have any additional attenuation. There are two isolators, terminated at 50 Ω at

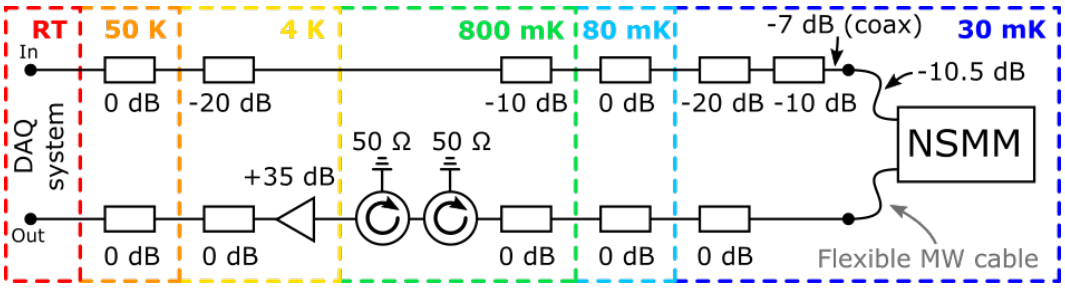

Figure 5.5: Schematic showing the temperature stages of the dilution refrigerator. The attenuation for the input and output microwave lines, as well as the coaxial cables that have a total loss of -7 dB at 6 GHz, are shown. The microwave cables that go directly to the NSMM at the 30 mK stage are flexible (with -10.5 dB loss at 6 GHz), allowing for the movement of the NSMM suspension. Data acquisition (DAQ) systems connect to the microwave lines at room temperature (RT).

800 mK, that reduce microwave reflections when measuring the weak microwave signal on the output line and, more importantly, to reduce thermal photons from the cryogenic amplifier. The amplifier (LNF-LNC1-12A) is used to amplify the weak signal by ~ 35 dB. The output line exits the cryostat at room temperature where it can be connected to a DAQ system. Two microwave measurement systems that were used in the experiments are discussed in the following sections.

5.3.2 VNA Measurements

Using a vector network analyser (VNA) is a straightforward method to measure the transmission, or the S_{21} component of the scattering matrix (see Eq. (4.22)), as a function of frequency for a superconducting resonator. A diagram of the measurement set-up using a VNA is shown in Fig. 5.6. The microwave input line in this set-up has 30 dB worth of attenuation at room temperature. This is to further reduce the power being supplied to the resonator so that it becomes possible to reach the single photon regime. The input line then goes into the cryostat and connects to the set-up shown in Fig. 5.5, leading to the NSMM and then coming back out of the cryostat again. The signal on the output line of Fig. 5.6 passes through 60 dB worth of amplification. The amplification is so that the signal is strong enough to be detected by the VNA. This circuit can have an optional yttrium iron garnet (YIG) band-pass filter added after the amplifiers on the output line to remove broadband noise from the amplifiers.

The VNA measurement set-up is useful for measuring the S_{21} transmission response of the resonator. With this set-up, we can extract values for the internal

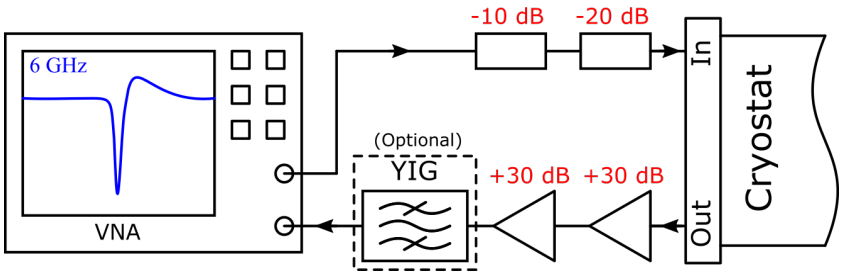

Figure 5.6: The microwave set-up for measuring the superconducting resonator inside the NSMM using a Vector Network Analyser (VNA).

Q_i, and coupling Q_c, quality factors by fitting to Eq. (4.22). The VNA can also vary the power going into the cryostat. This allows us to measure properties of the resonator as a function of the input power to the resonator, and by calculating the average photon occupancy by using Eq. (4.26) from Section 4.1.4 for a given input power, allows us to verify when the resonator is in the single photon regime. The resonant frequency shift Δf_r, of the resonator as a function of the tip-to-sample distance can also be measured using the VNA . This is simply done by sweeping in frequency through the resonator as the z-distance piezo-stepper steps away, starting from the sample surface.

The VNA can be useful for simple measurements of the resonator's properties, it is, however, not fast enough to measure other time-dependent processes of the resonator. Due to its slow measurement time, the VNA will average over processes that occur at high frequencies. This means that another measurement system is required that is fast enough to track these processes in real-time. This measurement technique must also operate over a wide frequency range much larger than the bandwidth of the resonator so that any shift in the resonance frequency can be observed.

5.3.3 Pound-Drever-Hall Locking

A more sophisticated measurement technique, called Pound-Drever-Hall (PDH) locking, can be use to measure the real-time frequency shift of the superconducting resonator with high-sensitivity. This method is commonly applied to optics experiments that require high-levels of laser frequency stabilisation, such as the interferometers used in gravitational wave detection experiments [120]. PDH locking has also been successfully applied to superconducting micro-resonators to measure their noise processes [51]. This method can accurately monitor the microwave resonance frequency while scanning a resonant microwave probe over the sample surface. Another advantage of the PDH technique is that it is insensitive to variations in electrical length. This means that variations caused by thermal drift, poor connectors or coaxial cables, moving parts or other noise processes do not affect the measurement readout signal. This makes using the PDH technique for fast microwave measurements ideal when scanning using NSMM, as opposed to an

interferometric technique such as homodyne detection. Measuring the resonator with the PDH technique also overcomes the drawbacks that limit a VNA measurement set-up.

PDH locking can be thought of as being similar to a heterodyne technique. A phase modulated (PM) signal that has two side-bands and a carrier tone are detected via the self-mixing of these signals, instead of using a mixer on two separate frequency sources. The amplitude of the down-converted signal depends strongly on the deviation of the applied microwave tone from the resonance frequency. This signal is then fed to a PID control system that works to keep the output at zero. This can be better understood by considering a PM voltage signal of the form

$$V = V_0 \exp(i\omega_c t + i\beta \sin(\omega_m t)), \tag{5.3}$$

where $f_c = \omega_c/2\pi$ is the carrier frequency, $f_m = \omega_m/2\pi$ is the PM frequency (causing the side-bands located at $f_c \pm f_m$) and β is the so-called modulation depth. This PM signal can be expressed in terms of Bessel functions of the first kind $J_n(\beta)$. To first order in n, we can write

$$V \approx V_0 \left(J_0(\beta) e^{i\omega_c t} + J_1(\beta) e^{i(\omega_c+\omega_m)t} - J_1(\beta) e^{i(\omega_c-\omega_m)t} \right). \tag{5.4}$$

The higher-order terms correspond to other harmonics of the side-bands, which are neglected here because the modulation depth for the PDH loop is such that all the power is predominantly concentrated in the main carrier tone and the two primary side-bands tones. It is these three frequencies that are expressed in the above function. This signal then passes through the resonator that we wish to measure. As mentioned in previous sections, the transmission of the resonator is given by $S_{21}(\omega)$ for some angular frequency ω. This, therefore, gives a transmitted voltage response V_T, of

$$\begin{aligned} V_T = V_0 \Big(& S_{21}(\omega_c) J_0(\beta) e^{i\omega_c t} \\ & + S_{21}(\omega_c + \omega_m) J_1(\beta) e^{i(\omega_c+\omega_m)t} \\ & - S_{21}(\omega_c - \omega_m) J_1(\beta) e^{i(\omega_c-\omega_m)t} \Big). \end{aligned} \tag{5.5}$$

After passing through the resonator, the signal is self-mixed with the use of a power

diode. The transmitted power passing through the diode is $P_T = |V_T|^2 = V_T V_T^*$. The algebra is somewhat long and, for the interested reader, has been written in full in Appendix B. Following through with the calculations (and passing the resulting signal through a lock-in amplifier after the power diode) we obtain the final result showing that the error signal used in the PDH loop is

$$\begin{aligned}\varepsilon \propto 2J_0(\beta)J_1(\beta)V_0^2\Big(&\mathrm{Re}S_{21}(\omega_c)\Big[\mathrm{Im}S_{21}(\omega_c+\omega_m)+\mathrm{Im}S_{21}(\omega_c-\omega_m)\Big]\\ &-\mathrm{Im}S_{21}(\omega_c)\Big[\mathrm{Re}S_{21}(\omega_c+\omega_m)+\mathrm{Re}S_{21}(\omega_c-\omega_m)\Big]\Big).\end{aligned} \tag{5.6}$$

This error signal is plotted in Fig. 5.7 in arbitrary units for a carrier frequency $f_c = 6$ GHz and modulation frequency of $f_m = 2$ MHz. The central peak at f_c is chosen to have an amplitude that is larger than the amplitude of two side-bands at the modulation frequency in the resulting error signal. The signal crosses zero at f_c and a PID controller is added to complete the PDH loop as this attempts to null any deviations from the zero point by adjusting the frequency of the carrier signal. The PDH error signal in Eq. (5.6) can be linearised about f_c. This gives a linear error signal about zero such that

$$\varepsilon_{\mathrm{lin}} \propto 4QJ_0(\beta)J_1(\beta)V_0^2(1-S_{21,\mathrm{min}})\frac{\omega-\omega_r}{\omega_r}, \tag{5.7}$$

where $S_{21,\mathrm{min}}$ is defined in Eq. (4.20) and Q is the total quality factor of the resonator that is defined in Eq. (4.21). This equation is also linearly dependent on the gain of the whole PDH loop. As the linear signal is dependent on the internal quality factor of the resonator, this will have an impact on locking to the resonator at low powers. A lower Q_i has the effect of decreasing the linear gradient and the frequency range over which the linear approximation is valid. This means that it is more difficult for the PID to reliably track changes in frequency if the bandwidth of the PID is not changed.

It is worth noting that an asymmetric resonance transmission shape will affect the error signal of the PDH loop. Asymmetry in $S_{21}(\omega)$ means that the zero crossing of the phase response of the resonator no longer corresponds to the resonant frequency (refer back to Fig. 4.5 for a reminder). This has two effects on the PDH loop. The first is that, if the phase zero crossing of the resonator no longer

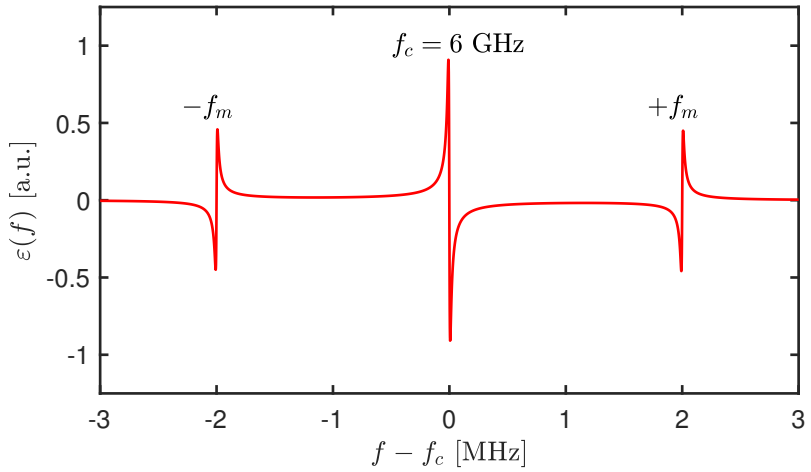

Figure 5.7: The error signal as a function of frequency $\varepsilon(f)$, produced by a Pound-Drever-Hall loop. This plot is centred on a carrier frequency of $f_c = 6$ GHz and has modulation side bands at $f_c \pm f_m$ where, in this plot, $f_m = 2$ MHz.

corresponds to the resonance frequency, then neither will the PDH error signal. Secondly, the magnitude of the error signal decreases as asymmetry is increased. This leads to reduced sensitivity of the PDH loop. This can be significant when trying to lock to the resonance at low powers. The resonators used in this thesis have relatively small asymmetry angles ($\sim 10°$) and so these limitations become negligible and do not hugely affect the results presented in this thesis.

Figure 5.8 shows the experimental set-up of the PDH loop that was used in the experiments in this thesis. It also shows two auxiliary microwave circuits, one that was used to measure the noise of the resonator and the second used for measuring the change in the PDH error signal with respect to the tip-to-sample distance $\partial\varepsilon/\partial z$. First, we will discuss the PDH loop in this configuration then each of the auxiliary circuits individually.

Starting from Signal Generator 1 (Keysight E8267D) in Fig. 5.8, this is used to generate a carrier frequency f_c, that is close to the resonant frequency of the superconducting resonator f_r, inside the NSMM. This carrier signal is then passed through a phase modulator (Hittite HMC538LP4) which is driven with a modulation frequency f_m. This frequency needs to be larger than the bandwidth of the resonator to ensure that it does not interact with the resonator. The resulting PM signal is then passed through a circulator to prevent reflections back up to the

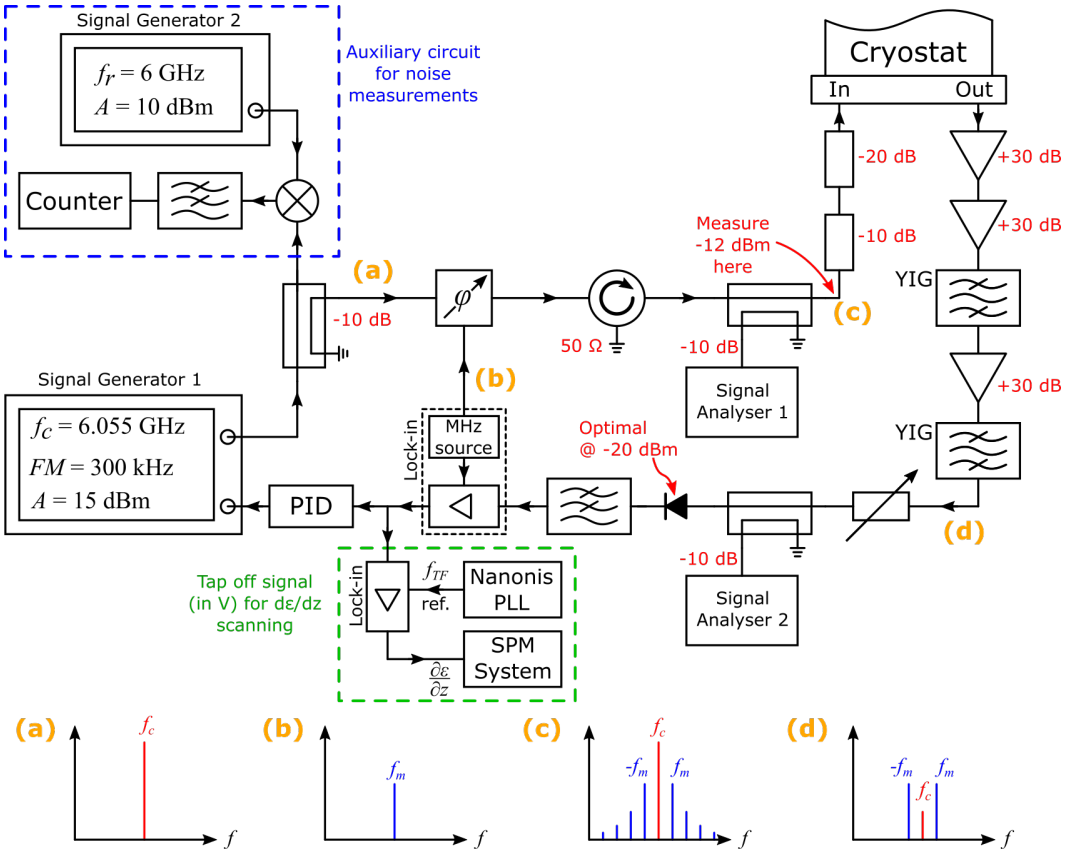

Figure 5.8: The Pound-Drever-Hall Loop microwave set-up that was used for measuring the resonator while scanning. The attached auxiliary circuit (blue dashed box) was used to measure the noise processes of the resonator. The signal coming from the PID controller was also tapped off to another auxiliary circuit (green dashed box) to measure the derivative PDH error signal with respect to tip-to-sample distance $\partial\varepsilon/\partial z$, while performing NSMM. Inset plots **(a-d)** show frequency spectra at various points along the PDH loop.

carrier and side-band source. After the circulator, the signal passes through some attenuators at room temperature and then into the cryostat set-up which is shown back in Fig. 5.5. After the signal has interacted with the resonator it passes out of the cryostat and is amplified using room temperature amplifiers (AtlanTecRF AOX-030120). This increases the signal power so that it comes within the optimal operating range of the diode. The signal is also passed through two band-pass YIG filters. This is to cut broadband noise from the amplifiers and the higher order harmonics of the PM signal. A variable attenuator is then used to set the power

of the output signal such that it is at the optimum level for the power diode (ATO 020080), which is, for the diode used in this set-up, $\sim$ 20 dBm. The diode has the effect of self-mixing the signal that passes through it. After the power diode, a low-pass filter that filters out the higher frequency signals after the self-mixing, leaving a signal with a low-frequency envelope at f_m to pass through. The signal is then demodulated at the modulation frequency using a lock-in amplifier to produce the error signal shown in Fig. 5.7. This spectrum is then fed to the PID controller (SRS SIM960) which works to null the signal *i.e.* keep the signal equal to zero. At the zero-crossing point, the gradient is very large meaning that any fluctuation in the signal about this point is directly proportional to frequency fluctuations of the resonator's resonance frequency. Finally, the signal coming out of the PID is fed back to signal generator 1 in Fig. 5.8 where a VCO adjusts the frequency of the generator so as to keep the carrier on resonance with the measured resonator.

An additional auxiliary circuit to the PDH loop is also shown in the blue dashed box of Fig. 5.8. This circuit is used when measuring the noise of the resonator. This signal takes the output from the generator (which is on resonance) and mixes it with a tone (from signal generator 2) that is close to the measured resonant frequency. The result of these mixed signals is then passed through a low-pass filter that removes the higher of the two main frequency components, leaving the difference between the two input frequencies to pass to a counter. The microwave counter then measures the changes in the resonant frequency of the resonator over time with high accuracy. For scanning with the NSMM, we instead need to produce a rasterised image from an analogue signal. Instead of using the counter we directly sample the signal used to control the VCO in generator 1 and use the known voltage-to-frequency conversion factor of the VCO.

Another auxiliary microwave circuit is shown in the green dashed box of Fig. 5.8 for measuring the $\partial\varepsilon/\partial z$, where z is the tip-to-sample distance. This is important because this allows us to produce a scan image that demonstrates the contrast formation mechanism of the NSMM. By tapping off the PDH error signal and feeding it through a second lock-in amplifier, we can demodulate the error signal at the tuning fork resonance frequency f_{TF}, by using it as the reference signal to the lock-in amplifier. As the PDH error signal is proportional to the resonator frequency in the linear regime (see Eq. (5.7)), this signal is proportional to $\partial f_r/\partial z$.

The signal is then fed into the SPM system to produce a scan image.

5.4 Qubit Samples

Having gone through the microwave measurement set-up for the superconducting resonator probe, we now discuss the sample that was used to produce most of the scans shown in Chapter 6, the following results chapter. The idea behind the sample was to have multiple 3×3 qubit arrays on one chip. Having many of these arrays made the process of finding a feature of interest much easier with the integrated AFM, considering the scanning area is small compared to the size of an individual qubit. Each array of qubits were designed to have transition energies corresponding to a range of frequencies between 6 - 7 GHz. This is because, if we hoped to eventually scan an actual material TLS defect with the NSMM, the same quantum interaction could be achieved with an 'artificial TLS' *i.e.* a superconducting qubit coherently coupling to the resonator probe, demonstrating a 'proof-of-concept' measurement for the NSMM.

An optical image of the sample along with a diagram of an individual qubit is shown in Fig. 5.9. Each array contains 9 qubits and there is a total of 18 arrays on the chip. Each qubit is approximately 26.5 µm in height by 58 µm in width. All of the qubits have a similar design that consists of an interdigitated capacitor with a SQUID loop at the centre. The dimensions of the capacitor are that each finger has

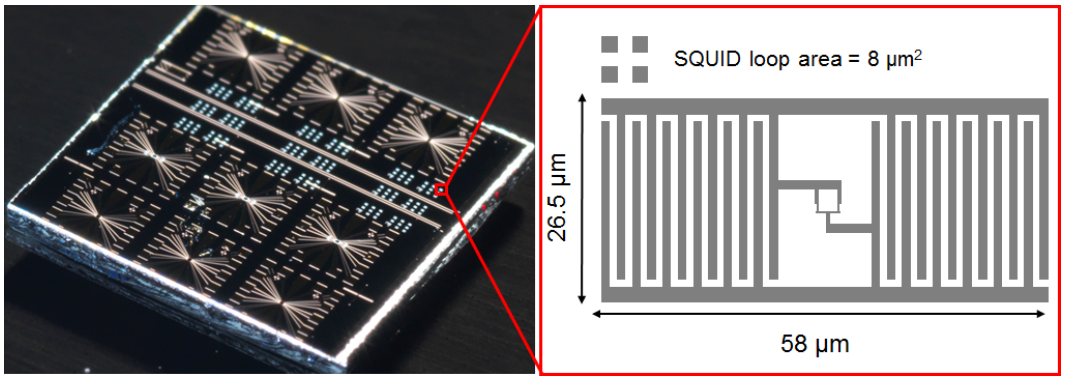

Figure 5.9: Qubit array sample that was fabricated at SuperFab at Royal Holloway, University of London. The finger widths are 1 µm, as is the spacing between the fingers. The squares at the top left of the sample are each 2×2 µm^2 in size.

a width 1 µm and the spacing between fingers is also 1 µm (meaning the pitch of the fingers is 2 µm). Each qubit per array has a unique identifier in the top left-hand corner (see the right-hand image of Fig. 5.9) indicating the designed frequency of the ground to the first excited state transition. The identifiers are an arrangement of 2×2 µm^2 metallic squares, with the number of squares corresponding to a frequency and position of a qubit within the array. These are useful when trying to navigate the NSMM about the sample.

These qubits consist of a capacitor with a SQUID loop at the centre. This superconducting circuit forms a simple transmon qubit. The inclusion of a SQUID allows for the qubit transition energy to be tuned with the use of an applied magnetic field - perpendicular to the plane the sample lies - from the solenoid under the sample platform (see Fig. 5.3).

This sample was fabricated at SuperFab at Royal Holloway, University of London by colleagues at Royal Holloway and the National Physical Laboratory. The fabrication process involves electron beam lithography of the 2D pattern of the array design. Once the two-layer e-beam resist was developed with an undercut, aluminium was evaporated at two angles, and in between the evaporations, the first aluminium layer was oxidised to produce the tunnel barrier in the Josephson junctions required for the SQUID loop at the centre of each qubit. Details of this process can be found in Ref. [121], the author of that thesis, T. Hönigl-Decrinis, also fabricated these samples.

Chapter 6

Results

The following chapter includes measurements such as the microwave transmission of the superconducting resonator, that is the S_{21} component of the scattering matrix, the frequency shift of the resonator as a function of the tip-to-sample distance and the coupling distance between the CPW and the inductive loop that is on the resonator itself. The internal Q-factor of the resonator is also extracted by fitting to the S_{21} transmission and expressed as a function of the average photon number within the resonator. We also present AFM scans and some microwave scans that were performed at different power levels. Noise measurements of the resonator over long time periods are also presented. These noise measurements are useful for highlighting what noise processes are dominant in the resonator and over which time scales. The noise measurement techniques are outlined back in Chapter 5 and are presented here using analysis methods such as power spectral densities (PSD) and the Allan variance, $\sigma_y^2(\tau)$. Lastly, we also present scans that were taken using the NSMM in the classical and single photon regime, as well as discussing the signal-to-noise (SNR) ratio of the NSMM.

6.1 Resonator Measurements

The measurements in this section are of the superconducting microwave resonator. It is this component of the NSMM that is used as the microwave probe within the microscope. The resonator itself has a metallic loop that inductively couples to a CPW that carries the microwave signal to the resonator that can then couple back to the CPW (see Fig. 5.4). This configuration receives and transmits the microwave signal. The signal is measured, using a VNA set-up (see Fig. 5.6), and it consists of the sum of the initial signal that did not couple to the resonator and the signal that coupled back to the CPW from the resonator.

Probe	f_r (GHz)	$Q_i(\langle n\rangle \sim 1)$	Δf_r [Distance]	Notes
3	5.912	1.1×10^5	170 kHz [48 µm]	Not FIB etched. This probe produced the preliminary scans. FIB etching destroyed it.
5	6.070	—	—	Parasitic mode near the resonance frequency.
6	5.998 (6.015)	8.5×10^4 (8.6×10^4)	50 kHz [24 µm] (—)	FIB etched twice. Produced some scans. Later crashed into the sample (post crash in brackets). Ruined the tip.
16	6.056	5.4×10^4	0.5 MHz [24 µm]	FIB etched tip. Most successful probe. Most of the data shown in this chapter is from this probe
18	5.999	8.0×10^4	—	Not in the NSMM. Good candidate for the future.
19	5.987	$\sim 8.4 \times 10^4$	—	Not FIB etched. Waiting for FIB etch.
21	5.990	1.6×10^5	—	Not in the NSMM. Excellent candidate for the future.

Table 6.1: A table showing some of the NSMM probes that were measured throughout this work. The table shows the probe number, its resonant frequency, the internal Q-factor at the single photon level, the frequency shift of the resonator with the change in tip-to-sample distance and some general notes concerning those specific resonators. Probe 6 shows two sets of data. This is because the probe was crashed into the sample surface. We observed a frequency shift of the resonant frequency but a small change in the Q-factor. Probe 16 was used for most of the measurements shown in this chapter, unless stated otherwise in the text. Probes that are not mentioned here were damaged or unresponsive.

6.1.1 Microwave Transmission Measurements

Multiple microwave resonator probes were measured throughout this work. A summary of some of the measurements of resonators has been tabulated in Table 6.1. Some probes yielded more data than others and some of that data is presented in this chapter. The probes are referred to by their numerical name and Table 6.1 will be referred back to frequently when discussing which measurements were used with which probes. Unless stated otherwise, Probe 16 was used for the majority of the measurements shown in this chapter.

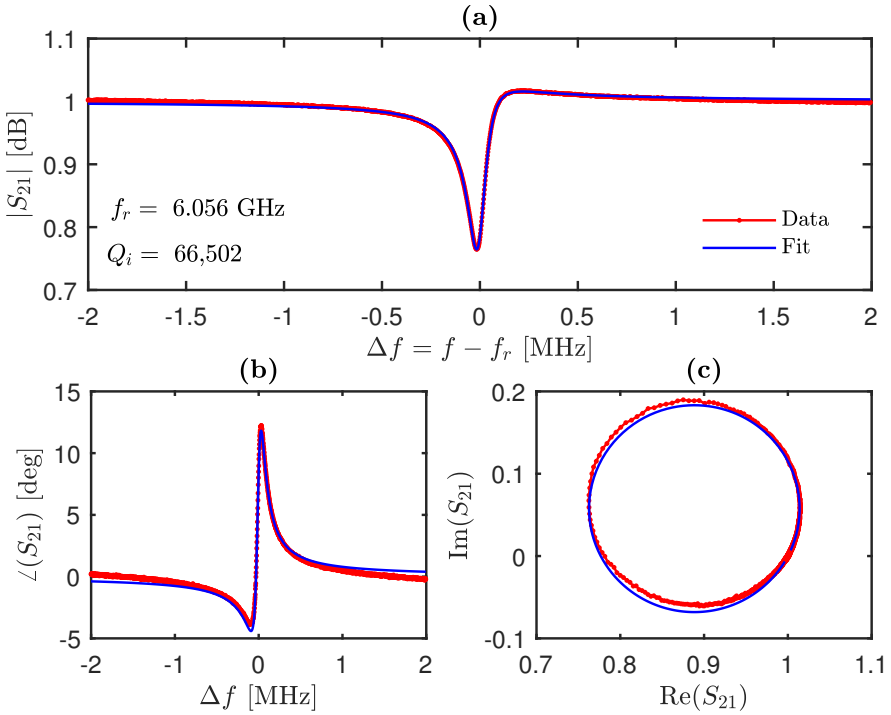

Figure 6.1: Measurements of Probe 16 with input power $P_{\text{input}} = -70$ dBm, translating to an average photon occupancy of $\langle n \rangle \sim 1.78 \times 10^6$. **(a)** The amplitude $|S_{21}|$, in dB, of the microwave resonator response measured as a function of frequency. The frequency is shown as the difference from the resonant frequency, f_r. This resonator has a $Q_i = 6.6 \times 10^4$. There is an asymmetry of the transmission that is due to a mismatch of the impedance on the microwave input and output lines. **(b)** The phase response in degrees, $\arg(S_{21})$ as a function of frequency difference from the resonant frequency. **(c)** The $\mathrm{Re}(S_{21})$ and $\mathrm{Im}(S_{21})$ components, *i.e.* the quadrature component $\bar{\mathrm{Q}}$, and the in-phase component I, respectively, of the transmission response of the VNA.

We can measure the transmission of the resonance of a superconducting microwave resonator using a VNA. We can measure the S_{21} component of the two-port scattering matrix to determine the microwave transmission through the CPW coupled to a resonator probe to extract the resonant frequency f_r, and fit to the internal quality factor Q_i. This S_{21} scattering matrix element is a complex number where $|S_{21}|$ is the magnitude and $\angle(S_{21})$ is the phase of the transmission through the microwave resonator, both of which are a function of frequency.

Figure 6.1 shows the S_{21} measurement of Probe 16 at 42 mK with an input power of $P_{\text{input}} = -70$ dBm, corresponding to an average of 1.78×10^6 photons populating this resonator. This is calculated using Eq. (4.26) for the average photon occupancy of the resonator. The extracted Q-factor of this resonator is 6.6×10^4. This is the highest quality factor of any resonator that has been used as a resonant NSMM probe at the time of writing [72, 75, 76, 122].

6.1.2 Quality Factor Power Dependence

The change in the intrinsic quality factor of a resonator as a function of the power applied to that resonator was measured at three different temperatures for Probe 16 and the data is shown in Fig. 6.2. Knowledge of the power supplied to the resonator

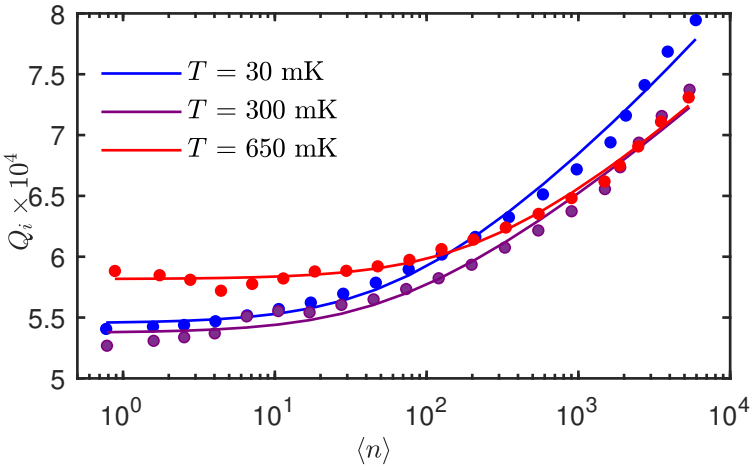

Figure 6.2: The intrinsic quality factor Q_i, of Probe 16 as a function of average photon number $\langle n \rangle$, for three different temperatures as measured at the mixing chamber of the cryostat. The data (•) is fitted (—) to Eq. (2.9).

allows us to calculate the average number of photons occupying the resonator by using Eq. (4.26) discussed in Chapter 4. The data is fitted using the framework of the standard tunnelling model using Eq. (2.9). Fitting the data to this equation returns $\alpha = 0.07$ and $F\tan(\delta_i) = 1.8 \times 10^{-5}$ as measured at 30 mK. Typical values for α from other experiments give $\alpha \sim 0.2$, based on the literature. This is higher than our calculated value from Fig. 6.2. This suggests a weaker dependence on the input power for our resonator probe as compared to other typical superconducting resonators.

Figure 6.2 shows a reduction in the internal quality factor for lower average photon numbers. As the average number of photons within the resonator decreases, the curve begins to saturate, indicating the onset of the single photon regime where, on average, a single photon is populating the resonator. This saturation occurs because there are fewer photons in the resonator to couple to material TLS defects and none of them become saturated. At intermediate powers, we have an increase in Q_i as more and more material TLS defects become saturated by the increasing number of photons. At even higher powers, the internal Q_i factor would begin to saturate again (not shown). This is when a large number of photons saturate the TLS in the resonator and other loss mechanisms begin to dominant. This happens when the loss rates of the TLS are exceeded by their effective Rabi frequency.

6.1.3 Tip-to-Sample Frequency Shift

Figure 6.3 shows the behaviour of Probe 16 as it is moved towards the sample surface. We show the data (measured using a VNA) of the resonant frequency shift of the NSMM resonator as a function of the tip-to-sample distance. As the metallic tip approaches a sample surface there is a frequency shift due to the changing capacitance ΔC, between the tip and the sample, meaning there is an increase in the resonant frequency of the resonator due to the decrease in capacitance as the tip is moved further away from the sample surface, $f_r \propto 1/\sqrt{C}$. This is described by Eq. (3.2) and, combined with Eq. (3.5) (describing the capacitance between a conical tip and surface), we are able to fit to the data in Fig. 6.3. This fit yields an approximate tip radius of $R = 2$ µm, but an almost zero taper angle, as defined by Eq. (3.5). This suggests that a sphere-to-surface capacitance model is sufficient

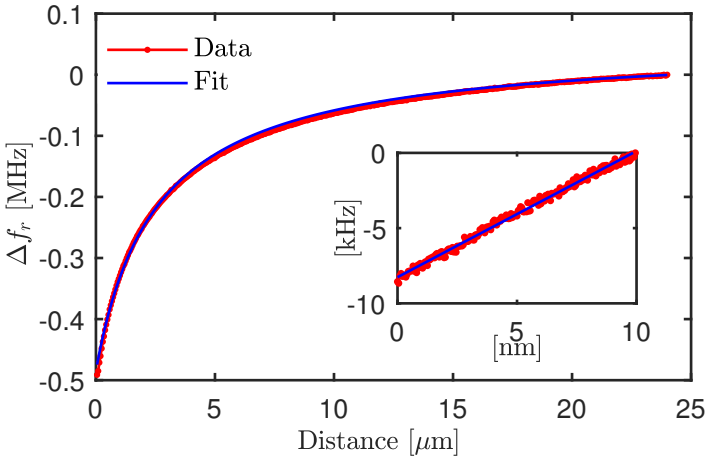

Figure 6.3: The frequency shift of Probe 16 as a function of tip-to-sample distance. These data were fitted to using Eq. (3.2) and Eq. (3.3). This results in an estimated tip radius of $R = 2$ µm. Inset: The frequency shift at small distances with a linear approximation. The gradient is calculated to be 0.84 kHz/nm.

enough to describe the electrostatic interaction between the tip and a surface for this probe.

The inset of Fig. 6.3 shows a section of an approach curve where the tip-to-sample distance is small *i.e.* just above the surface, that we can assume a proportionally linear shift in resonator frequency. The red line shows the measured data and the blue line shows a linear fit. The gradient of this line is calculated to be 0.84 kHz/nm for Probe 16. This gives us a conversion between the shift in resonant frequency to a distance for cases when the tip is in 'contact', or close to, the sample surface. Zero distance in these plots is defined as the point when the tip is in contact with the sample.

6.1.4 Variable Coupling

The distance between the inductive coupling loop on Probe 16 and the CPW can be changed with the use of a small piezo-electric stepper placed behind the CPW. This means that a similar measurement to that shown in Fig. 6.3 can be performed again but for the change in internal quality factor Q_i, of the resonator and the coupling quality factor Q_c, as a function of the loop-CPW coupling distance. Figure 6.4(a) shows this data. We note that the number of steps was used instead of a measure

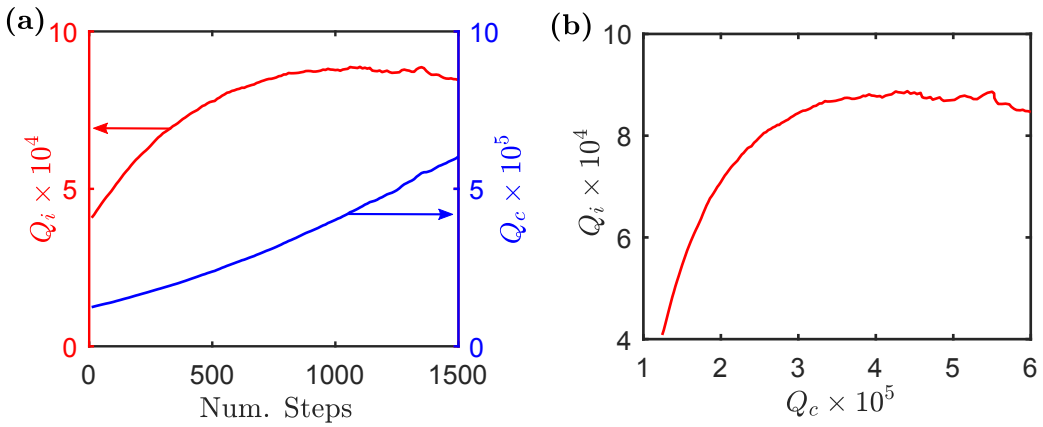

Figure 6.4: **(a)** The intrinsic (left red axis) and coupling (right blue axis) quality factors as a function of the number of steps made by the coupling piezo-stepper for Probe 16. **(b)** The same intrinsic quality factor Q_i, plotted as a function of the coupling quality factor Q_c, as described by Eq. (6.3). Note that an increasing number of steps means an increasing separation between the CPW and the probe.

of loop-CPW distance. This is because it is difficult to calibrate the distance that one step corresponds to for the coupling piezo-stepper. The complex geometry makes it difficult to find an analytical solution to the mutual inductance and the coupling.

To explain the results in Fig. 6.4(a) we consider the idea that the response in Q_i follows from the change in $\langle n \rangle$ induced by the change in Q_c *i.e.* less energy can couple to the resonator as the CPW is moved further away from the resonator. By combining Eq. (4.26) for the average number of photons in a resonator with Eq. (2.9) for the power dependent losses $Q_i \propto \langle n \rangle^\alpha$ (for $\langle n \rangle \gg 1$), we can therefore write that

$$Q_i \propto \left(\frac{Q^2}{Q_c} \right)^\alpha . \tag{6.1}$$

Recalling that $Q = Q_i Q_c / (Q_i + Q_c)$ from Eq. (4.21) we get

$$Q_i \propto Q_c^\alpha \left(\frac{Q_i}{(Q_i + Q_c)} \right)^{2\alpha} , \tag{6.2}$$

then rearranging gives

$$Q_i^{1-2\alpha} \propto \frac{Q_c^\alpha}{(Q_i + Q_c)^{2\alpha}} . \tag{6.3}$$

Now we consider two limits of the above equation. The first is when $Q_i \ll Q_c$; Eq. (6.3) simplifies to $Q_i \propto Q_c^{-\alpha/(1-2\alpha)}$. Inserting our calculated value of $\alpha = 0.07$ from the fit to the data shown in Fig. 6.2 at 30 mK gives $Q_i \propto Q_c^{-0.08}$. The second limit is when $Q_i \gg Q_c$ which simplifies to $Q_i \propto Q_c^{\alpha} = Q_c^{0.07}$. This is in good qualitative agreement with the Fig. 6.4(b) which shows Q_i plotted as a function of Q_c. The gradients in the two aforementioned limits are both much less than one as predicted by Eq. (6.3). This shows that as the coupling quality factor is changed, which is also dependent on the loop-CPW distance, we change the internal quality factor, which is dependent on the average number of photons stored in the resonator.

6.2 Scanning

This section shows some of the scanning results that were taken using the NSMM. We present AFM scans of sample topography that make use of the tuning fork and the feedback control using a PID controller, as well as microwave scans taken with the use of a PDH loop. We present microwave scans at high powers that demonstrate 'classical' NSMM and at low powers that demonstrate the first NSMM scanning results in the single photon regime. These scans were taken using different probes from Table 6.1 and will be specified when discussing each scan.

We first show some early results from the NSMM using a sample consisting of a thin layer of Nb on a Si substrate. We then show scans of the sample described in Section 5.4. This latter sample consists of an Al interdigitated capacitor patterned onto a Si substrate. The scans will show three metallic squares (2×2 µm^2 in size) placed adjacent to two larger metallic structures that form an interdigitated capacitor. Each metal finger of the capacitor has a width of 1 µm with spacing between the fingers of 1 µm.

6.2.1 Preliminary Scans

Shown in Fig. 6.5 are some early scans using Probe 3 inside the NSMM. Note that this is a different probe than was used for previous measurements (see Table 6.1). The sample under investigation is a thin layer of Nb on a Si substrate. The Nb

layer was known to be 140 nm thick, meaning that this would be a useful sample to use to calibrate the z-piezo tubes in AFM. The AFM response is shown in Fig. 6.5(a). The colour bar scale of this image is the feedback signal of the tuning fork whilst acting to maintain a constant tip-to-sample distance. The scans show the Nb film on the Si substrate in an AFM image and a microwave scan showing the resonator frequency shift response of Probe 3. This initial AFM scan shows a measured film height of ∼70 nm (see Fig. 6.6), as this scan was taken prior to calibrating the AFM. For later scans, we adjusted the calibration of the z-piezo tubes by a factor of two to achieve an accurate measure of the topography of a sample. We can also calibrate the piezo-tubes that control the fine and coarse xy positioning. For fine positioning, the process is similar to the z calibration in that we scan a feature of known dimensions and account for any differences with a calibration factor. For coarse xy calibration, an AFM scan is performed on a sample of known dimensions, the tip is lifted and moved in either x or y by a known number of steps. Then another AFM scan is performed and the change in distance between the two scans can be used to calculate the step size of the coarse piezo-steppers.

The microwave scan (Fig. 6.5(b)) is a promising initial result as it shows that the NSMM shows a contrast down at relatively low power levels, in this case when

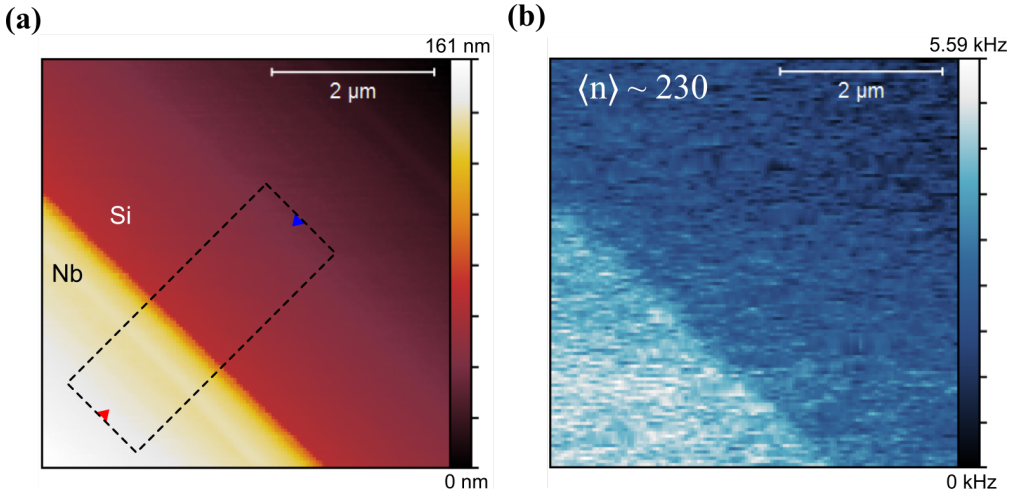

Figure 6.5: Early scans using Probe 3 in the NSMM of a thin Nb film on a Si substrate sample. **(a)** AFM response and **(b)** microwave frequency shift at $\langle n \rangle \sim 230$. These scans were taken at $T = 30$ mK.

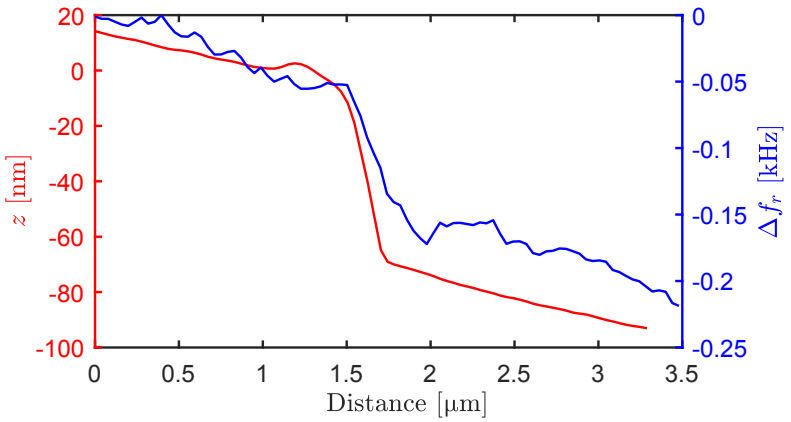

Figure 6.6: Line traces averaged over 30 lines from scans taken using Probe 3. Data is from the dashed box region shown in Fig. 6.5(a) for both the AFM response and microwave frequency shift response.

$\langle n \rangle \sim 230$. The AFM component is used to maintain a constant tip-to-sample distance, meaning that the contrast in the microwave scan arises from the change in dielectric properties between the metal and the dielectric substrate.

We can further analyse the preliminary scans by taking averaged line traces across the dashed box region that is shown in Fig. 6.5(a). This was done for 30 lines on the AFM scan (left red axis) and on the microwave response scan (right blue axis). Both results are shown in Fig. 6.6. Each of the line traces shows the tilt of the sample platform, which becomes a limiting factor for the maximum achievable scan window before the piezo-tube for fine xy scanning control reach a maximum or minimum point. If there were not a tilt we would observe line traces that are horizontal to the abscissa (except at the step between materials). Looking at the red AFM trace we can see a 'bump' at the top edge of the Nb film on the sample. This is an example of an artefact due to the size of the AFM tip. As this bump appears in both the forward and backward direction of scanning, it is likely due to the Nb on the sample peeling back at the edges. This structure is then smeared out by the large tip radius compared to the size of the feature. Looking to the microwave line trace we see that, overall, this signal is noisier. This is to be expected, especially at relatively low microwave powers. We also note that from Table 6.1, Probe 3 has a small frequency shift per unit distance of approach. Hence the actual microwave tip is not close to the surface or that the resonator is

poorly coupled. As for the noise, this can be a result of the mechanical noise, the intrinsic noise of the resonator itself or the white noise in the cryogenic microwave amplifiers. This can also be due to the frequency shift being small and so the microwave signal is overall smaller too. The noise processes that affect the NSMM are discussed later in Section 6.3 and give a more in-depth discussion on the noise processes affecting the microwave output signal at low powers.

6.2.2 Scanning in the Single Photon Regime

Probe 16 was used for the following AFM and low-power scan results. A different sample was also used than the one described in the previous section. A now calibrated AFM scan was taken using the new probe and is shown in Fig. 6.7 which shows the corner of an interdigitated capacitor section of a qubit with adjacent metallic pads. The colour bar scale indicates the relative heights of the features of the sample, with zero being set to the lowest point. When scanning, we measure a voltage signal from the piezo-tube which can then be converted to a distance with a known calibration factor (see Section 5.2.1) allowing us to scan the topography of a sample surface. The finger width of the inter-digitated capacitor was designed to be 1 µm but this width appears to be larger in Fig. 6.7, similarily the finger spacing was designed to be 1 µm but appears smaller in the AFM scan. This is likely due to the size of the AFM tip. A large tip compared to a sample's feature size will add artefacts to the scan image and make features appear wider or more smeared out than they acually are, as discussed in the preliminary scans data and

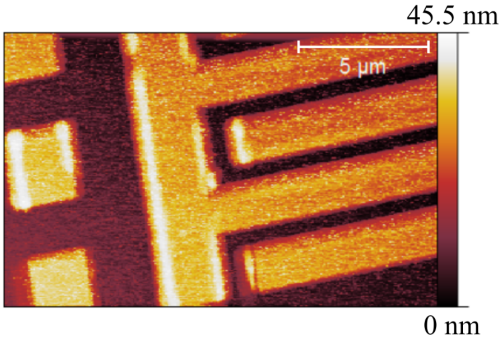

Figure 6.7: AFM scan, from the tuning fork response, of the topography of an interdigitated capacitor with adjacent metallic pads using Probe 16 at 30 mK.

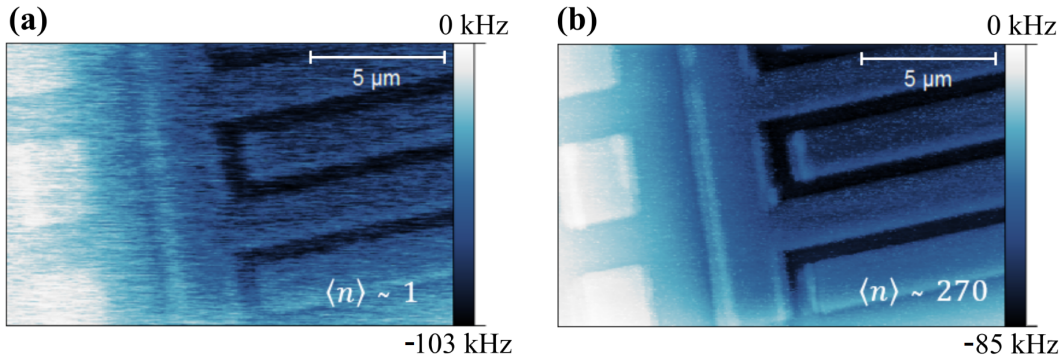

Figure 6.8: Microwave response scan due to the resonant frequency shift of resonator Probe 16 at **(a)** the single photon regime ($\langle n \rangle \sim 1$) and **(b)** at a higher power ($\langle n \rangle \sim 270$). Both scans were taken at 30 mK. For the scans, zero frequency shift of the resonator is defined to be when the tip is far away from the sample.

in Chapter 3. Figure 6.7 has been post-processed by subtracting a mean plane fit to compensate for any tilts in the scan.

Figure 6.8 show scans of the same region as shown in the previous AFM. These scans were done with the microwave response from the PDH loop feedback. When scanning we measure a voltage signal from the resonator. It is possible to convert this signal from a voltage to a frequency shift of the resonator by using a conversion factor from the VCO in the signal generator that is used in the microwave set up (see Section 5.3.3). The microwave scan shown in Fig. 6.8(a) is taken at ultra-low powers such that the average photon occupancy of the resonator $\langle n \rangle \sim 1$. Remarkably, even at these ultra-low power levels, up to 10^9 times lower than in conventional NSMMs (the lowest reported power levels in the literature are down to about -20 dBm [68]) a clear contrast can be resolved in the single photon regime NSMM image. A similar scan taken at higher powers ($\langle n \rangle \sim 270$) is shown in Fig. 6.8(b). As expected, the scan taken in the single photon regime is noisier than the high power scan of the same region. This microwave image is less noisy compared to the preliminary scan shown in Fig. 6.5. Referring back to Table 6.1 shows that Probe 16 has a larger frequency responsivity than the probe used for the preliminary scans and so has a much cleaner signal at ~ 270 photons.

The tip-to-sample distance is kept constant by the AFM feedback from the tuning fork so the contrast shown in the microwave scans is therefore mainly due to changes in capacitance between the metallic tip and the sample. The contrast

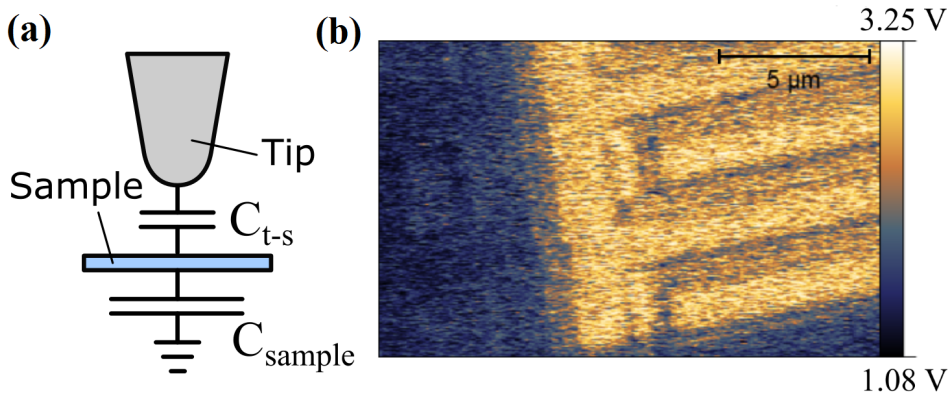

Figure 6.9: The PDH 'error' signal demodulated at the tuning fork frequency (30 kHz), this is proportional to df_r/dz. Taken at 30 mK with $\langle n \rangle \sim 270$.

can be due to a change in the dielectric constant of the underlying sample, as is seen by the contrast of darker areas between the fingers (when the tip is above Si) and the brighter regions on the fingers of the interdigitated capacitor (when the tip is above Al). The smaller metallic squares in both scans in Fig. 6.8 are brighter than the larger metallic structures. This is because a smaller structure has a weaker capacitive coupling to the ground compared to larger ones. This means that a smaller metallic structure adds a smaller capacitive contribution to the tip and produces a smaller shift in the resonant frequency of the NSMM probe.

The contrast formation mechanism in the high and low power microwave scans originates from the capacitance network forming between the tip, the sample features and ground as illustrated in Fig. 6.9(a). The contrast formation mechanism can be demonstrated experimentally and is shown in Fig. 6.9(b) showing the response of the resonator at $\langle n \rangle \sim 270$, demodulated at the measured tuning fork frequency of 30 kHz. The same scan was performed at $\langle n \rangle \sim 1$, however, the SNR of this scan was less than 1. The reduced contrast for the smaller metallic pads implies that the size of the tip dominates the capacitance, whereas the larger metallic structures have a larger self-capacitance C_{sample}, resulting in the response being dominated by the time-dependent tip-sample capacitance $C_{\text{t-s}}$. In other words, the contrast in Fig. 6.9 originates from the change in microwave resonance frequency as the tip oscillates at the tuning-fork frequency close to the sample surface. The demodulated signal is the PDH loop 'error' signal which is not tracked by the PID

(with a bandwidth limited to $\sim$ 10 kHz). For variations smaller than the resonance linewidth, the 'error' signal becomes directly proportional to the linearised phase response around f_r and thus the demodulated signal is proportional to df_r/dz.

6.2.3 Signal-to-Noise

Microwave scans like the ones shown in Fig. 6.8 were performed for several different average photon numbers. From these multiple scans we calculated the SNR for each scan and then plotted this as a function of the average photon number, the result of which is shown in Fig. 6.10. To evaluate the SNR we calculate the difference between the average response on an area above a metallic region and an area of the dielectric substrate (between the metallic structures). We then divide this signal by the noise which is estimated using the root mean square variation over the same areas. This was done for five different scans at differing powers. As would be expected, the SNR is lower for scans that are close to the single photon limit than for scans at higher powers. This is in agreement with the previous conclusion that, except for the scans taken at very low average photon numbers, the noise is dominated by mechanical noise which is independent of the applied microwave power (see Section 6.3).

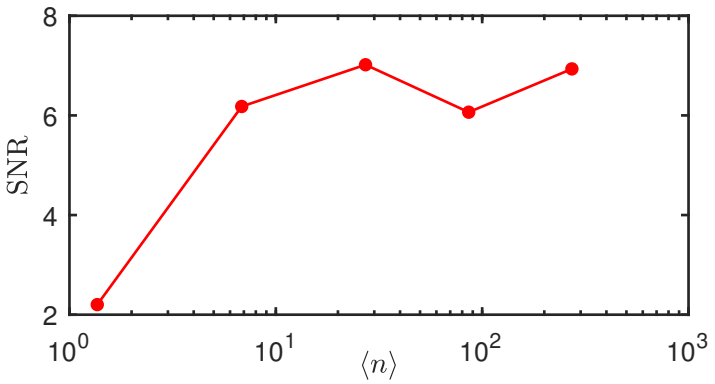

Figure 6.10: The signal-to-noise ratio (SNR) obtained from multiple scans as a function of the average photon number occupying the resonator $\langle n \rangle$.

6.3 NSMM Performance and Limitations

The following results in this section are pertinent to the whole of the NSMM *i.e.* the response from the tuning fork as well as the microwave response from the superconducting resonator. All of these measurements were taken using Probe 16 (refer to Table 6.1). The data shown in this section shows measurements of the frequency shift of the probe as a function of temperature, the mechanical noise measured from the tuning fork and the noise intrinsic to resonator that was measured using the PDH loop, described in Section 5.3.3. The noise measurements in particular are presented in the form of power spectral densities (PSD), frequency noise plots $S_y(f)$, and Allan variance plots $\sigma_y^2(\tau)$, where τ is the measurement time for experiments that measured resonant frequency fluctuations of the microwave resonator probe.

These noise measurements and analysis techniques are useful because they reveal further information into the mechanical stability of the NSMM and what noise processes are limiting the system. For example, a PSD plot can give information on the effectiveness of the mechanical suspension on reducing the effect of external sources of mechanical vibrations, particularly that of the frequency of the pulse tube that is on top of the dilution refrigerator (seen as a peak on the PSD). Frequency noise plots show clearly the levels of white and flicker frequency $(1/f)$ noise and which process is dominant in the measurements. However, frequency noise charts can be calculated using different algorithms. This means they can give inconsistent information on the same set of data. This is where Allan variance analysis becomes useful. The Allan variance does not suffer from these inconsistencies and, as well as highlighting white and flicker frequency noise processes, it is also able to show additional noise sources such as frequency drift. More information and detail of these analysis techniques can be found in Section 2.4.

6.3.1 Temperature Dependence of the Probe

Scans such as Fig. 6.8(a) from Section 6.2.2 show that we achieved scanning in the single photon regime. One would expect that at these power levels to be able to coherently couple to material TLS defects. Especially so given that

estimations for material TLS defect densities on naturally oxidised aluminium are $\sim$ 1 TLS per µm^3 within a 100 kHz bandwidth around the resonance frequency [38,123]. For a scan size of 10×17 µm^2, this means that one would expect to at least observe a small number of material TLS defects.

If we recall that in order to achieve coherent coupling to an individual material TLS defect with a resonator probe, we must satisfy two major requirements. These are (i) low power such that $\langle n \rangle \sim 1$, which was achieved in these scans, and (ii) low temperatures such that the material TLS defects are mostly in their ground states. This led to an investigation into the temperature dependence of the single photon Q-factor. Referring back to temperatures shown in Fig. 6.2 we can calculate the expected change in $Q_i(T)$ as a function of temperature and compare it against what is actually measured. Recalling from Eq. (2.9) that the thermal saturation of material TLS defects in a resonator for small and fixed photon numbers goes as $Q_i(T) \propto \tanh(\hbar\omega/k_B T)$ and using the temperatures in Fig. 6.2 at $\langle n \rangle \sim 1$, we can calculate the theoretical change in $Q_i(T)$ for the highest and lowest temperatures with $\omega = 2\pi \cdot 6$ GHz by writing

$$\frac{Q_i(T = 30 \text{ mK})}{Q_i(T = 650 \text{ mK})} = 4.5, \tag{6.4}$$

the expected change in Q_i. However, we measure a ratio of ~ 1.5. This is notably smaller than the expected theoretical value, indicating that the material TLS defect bath and the resonator are not entirely thermalised with respect to the mixing chamber of the cryostat.

Separate independent measurements further corroborate this idea. By measuring the frequency shift of the resonator as a function of temperature we can see if the response is as expected. As the resonator is cooled, we would expect to see a minimum in the temperature dependence at $T = \hbar\omega/2k_B$, which in this case corresponds to a temperature of $\sim$ 140 mK [41], followed by an increase in Δf_r as $T \to 0$. The results for this measurement are shown in Fig. 6.11. The red trace is for the case when the resonator is in the NSMM enclosure and the blue trace is during a well-shielded separate cool-down of the same probe, which showed the expected temperature dependence. Here, saturation occurs at $\sim$ 50 mK, the typical temperature achieved in this type of measurement. It must be noted that

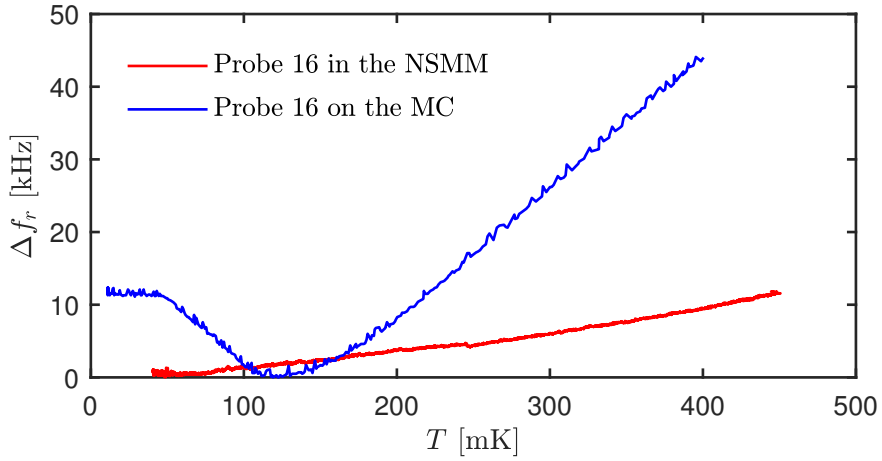

Figure 6.11: The frequency shift of the superconducting resonator probe as a function of temperature. The measured traces are for the cases where *red:* with the resonator inside the NSMM and *blue:* with the resonator directly bolted to the mixing chamber plate and in 'dark' conditions. Note the temperature is measured at the mixing chamber (MC) plate for both cases.

the temperature scale that is shown in Fig. 6.11 is the temperature as measured at the mixing chamber of the DR. These two traces do not match, adding more substantial evidence to the idea that the material TLS defect bath and the resonator are not properly thermalised. The blue trace shows the expected behaviour with a minimum at around 140 mK. The red traces show no such minimum and has a different gradient than the blue curve (for temperatures above 140 mK). This suggests that the resonator has a temperature well above what is actually measured. This is likely due to the holes in higher temperature plates of the cryostat that are needed for the kevlar thread to feed-through the cryostat for the suspension system meaning that the NSMM enclosure is not entirely dark and high-frequency infrared photons heat the poorly thermalised resonator on the tuning fork as well as the sample. This explains why no material TLS defects were seen in the ultra-low power scans, as the sample is as poorly thermalised as the resonator probe. This means that additional engineering of the NSMM enclosure, suspension feed-throughs, and thermal anchoring of the probe and sample is needed to ensure increased thermalisation.

6.3.2 Mechanical Power Spectral Densities

The NSMM itself is designed to be operated at cryogenic temperatures and so must be inside a dilution refrigerator system. This inevitably provides design challenges that need to be overcome. One such challenge is to minimise external mechanical vibrations but in particular the effect of the pulse tube, which has a piston frequency of ∼1.4 Hz. The solution that has been implemented is to suspend the microscope from three copper-beryllium (CuBe) springs to dampen the effect of the pulse tube. This essentially acts as a mechanical low-pass filter that is designed to have a cut off frequency lower than that of the pulse tube piston frequency. A diagram of the suspension system can be found in Fig. 5.1.

To determine the mechanical stability of the suspension system for the NSMM we measure the power spectral density (PSD) of the fluctuation in the centre frequency of the resonator Δf_r. This was measured using the SPM controller software. These measurements were done using Probe 16 for three different parameter combinations of tip-to-sample distances and average photon numbers. These were when:

- The tip was in contact with the surface and operating within the single photon regime *i.e.* ($z = 0$ nm, $\langle n \rangle \sim 1$)
- The tip was in contact with the sample surface and at high photon numbers *i.e.* higher powers ($z = 0$ nm, $\langle n \rangle \sim 10^3$)
- The tip was pulled back from the sample surface and at high photon numbers *i.e.* higher powers ($z = 5$ nm, $\langle n \rangle \sim 10^3$)

For clarity, we define $z = 0$ as the reference point where the AFM tip of our NSMM is in contact with the sample surface. This is *not* to say that there is exactly zero distance between the the tip and the sample.

These measurements are shown in Fig. 6.12. The peak at 1.4 Hz - as well as higher-order harmonics - are due to the dilution refrigerator pulse tube on the two high power PSD traces. In the higher power regime ($\langle n \rangle \sim 10^3$), while in contact with the surface, the frequency fluctuations of the microwave resonator Δf_r, are limited by the mechanical noise of the system, which translates to frequency noise

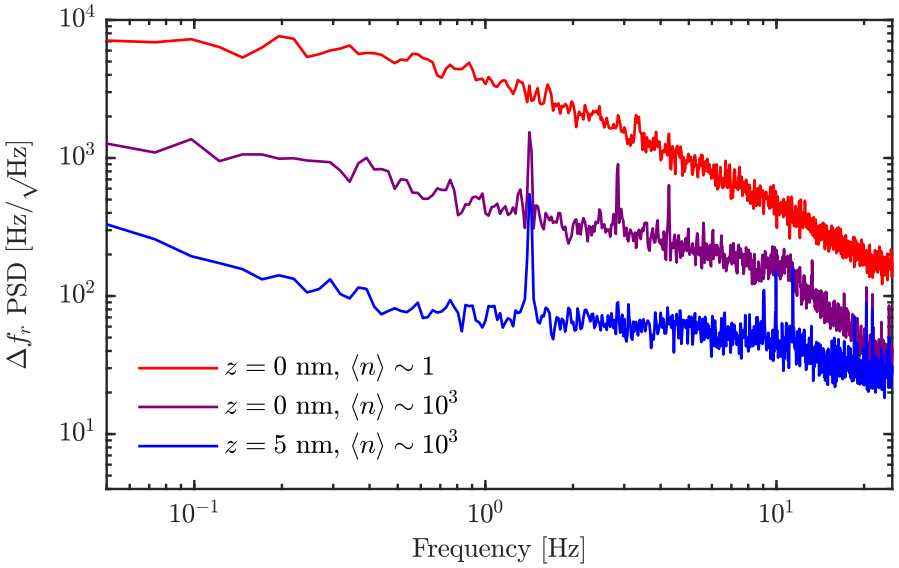

Figure 6.12: PSD of the microwave frequency shift Δf_r, from the superconducting resonator on Probe 16. The peak at 1.4 Hz is the pulse tube. *Red line:* When the tip is in 'contact' with the sample surface ($z = 0$ nm) at low power ($\langle n \rangle \sim 1$). *Purple line:* When the tip is in contact at high power. *Blue line:* When the tip is retracted ($z = 5$ nm) from the surface at high power. The kink in the data above $\sim 10^1$ Hz is the roll-off of the PID bandwidth in the PDH loop.

through the fluctuations in tip-to-sample capacitance. When the NSMM probe is in contact with the sample, the peak amplitude of 1.5 kHz/$\sqrt{\text{Hz}}$ at 1.4 Hz corresponds to a tuning fork amplitude dither of 1.8 nm, this is lower than, or comparable to, other cryogenic SPM systems [124–126]. This is calculated using the frequency to distance conversion factor found from the inset of Fig. 6.3 which was 0.84 kHz/nm. Lifting the tip by 5 nm reduces the sensitivity of the resonator to mechanical noise, the corresponding reduction of the PSD indicates that the mechanical noise limits the frequency read-out accuracy of the microwave resonator at high powers. However, in the single photon limit, the noise level is much higher and the peaks due to the pulse tube are washed out. Here the dominating noise process at the time-scales shown in Fig. 6.12 is the white noise (due to the HEMT amplifiers and the loss in the cables leading to them) of the measurement set-up. The roll-off of data above 10 Hz is due to the bandwidth of the PID controller in the PDH loop set-up.

This data was taken using the scanner software that controls the feedback for

the tuning fork. Although useful information can be gathered from Fig. 6.12, it is not entirely clear what other noise processes - such as the intrinsic $1/f$ noise due to material TLS defects - may be affecting the NSMM. To find this out, we employ more sophisticated techniques and analysis methods for measuring noise and the results are discussed in the following section.

6.3.3 Resonator Frequency Noise and Allan Variances

To experimentally measure the noise of superconducting resonators, a PDH loop set-up is used. This is outlined in more detail in Section 5.3.3. The PDH loop is used to track the fluctuations in the resonator's resonant frequency Δf_r. These fluctuations were measured over long time periods, approximately 10^3 s. This is so that noise processes that may occur over longer time periods can be measured and analysed. It is worth noting that the noise measurements that are presented here all exclude mechanical vibrational noise, as the tip was moved far away from the sample surface when performing these measurements.

The frequency noise spectrum $S_y(f)$ at a given frequency can be plotted as a function of the average photon number. This data is shown in Fig. 6.13(a) for $S_y(f = 1\text{ Hz})$ with a fit to this data. We choose 1 Hz as this simplifies the analysis for calculating the amplitude of the $1/f$ frequency noise, reducing the spectrum to $S_y(f = 1\text{ Hz}) = A$, where A is the amplitude of the $1/f$ frequency noise. The fit in Fig. 6.13(a) is to Eq. (2.10), which states that $A \propto \langle n \rangle^{-1/2}$. This fit yields $A = 5.1 \times 10^{-15}$. From this analysis, it is possible to calculate the $1/f$ intrinsic noise level of the resonator due to material TLS defects. For $\langle n \rangle \sim 1$ (at $f = 1$ Hz) the noise level was estimated through extrapolation to be $\sim 430\ \text{Hz}/\sqrt{\text{Hz}}$. This is comparable to the mechanical noise found in the previous section. As mentioned, this was calculated by extrapolating the data in Fig. 6.13(a) to the single photon regime. Experimentally speaking, it is difficult to maintain the PDH lock at such low powers because the $1/f$ noise was masked by the white noise at these low powers levels. Hence, we measured to as low a power as possible (corresponding to $\langle n \rangle \sim 6$), applied the fit to the data and then extrapolated.

Shown in Fig. 6.13(b-e) are the calculated Allan variance $\sigma_y^2(\tau)$, and the full frequency noise spectrum $S_y(f)$, of the lowest and highest power measurements

	$\langle n \rangle \sim 6$	$\langle n \rangle \sim 250$
$h_0 \times 10^{16}$	60.5	2.6
$h_{-1} \times 10^{16}$	1.3	0.4

Table 6.2: The amplitude for white (h_0) and $1/f$ (h_{-1}) noise levels as calculated from the data and fits shown in Fig. 6.13, using Allan variance analysis.

shown in Fig. 6.13(a). We discuss each plot in more detail and show how the individual noise processes were calculated. The theory that was discussed in Section 2.4 is useful for understanding the data that is presented in these plots.

Figure 6.13(b) shows the calculated Allan variance for the lowest power measurement that corresponds to $\langle n \rangle \sim 6$. At a glance, the data (red circles) shows a high level of white noise with a small upturn at longer time scales. We can fit this data to the power laws that can be used to describe these noise processes. By fitting to

$$\sigma_y^2(\tau) = \frac{h_0}{2\tau} + 2\ln(2)h_{-1}, \tag{6.5}$$

where h_0 and h_{-1} are defined back in Table 2.1, it is possible to extract the constituent noise processes that make up the whole noise spectrum. These components are then plotted on top of the Allan variance plot (black dashed lines). These lines show clearly the white noise level, particularly at shorter time scales, in Fig. 6.13(b) and the $1/f$ level. The extracted values of these noise amplitudes are summarised in Table 6.2. The white noise is proportional to $1/\tau$ and the flicker frequency noise is a constant on the Allan variance. However at the longest time scales in the measurement (> 300 s) there is a small but noticeable upswing in Fig. 6.13(b). This indicates the onset of random walk frequency noise. This noise process was not fitted to because there is simply far too few data points to get a meaningful value for this particular noise level. If the resonator were to be measured for longer periods of time, this would improve the statistics by having more points to fit to. However, increasing measurement times by one or two orders of magnitude for these measurements quickly becomes impractical in a realistic laboratory setting.

These fits to the noise level amplitudes can be easily translated such that they

can show the same noise levels but on a frequency noise spectrum. This is what has been done in Fig. 6.13(c). This plot shows that the calculated values of h_0 for the white noise level and h_{-1} for the $1/f$ noise (with their numerical values in Table 6.2). Looking at the white noise level, it is clear that the calculated noise amplitude does not match exactly with the data in this plot. However, this can be explained by the aforementioned upswing in random walk frequency noise that is more obvious in the Allan variance plot of Fig. 6.13(b) than in Fig. 6.13(c). Again, if measurement times were practically able to go on for one or two orders of magnitude longer, then this level would likely improve to match the data. The data also does not exactly match the fit to the calculated $1/f$ noise level in Fig. 6.13(c) either. This can also be attributed to relatively short measurement time, meaning that the $1/f$ noise has 'not had the time' to be the dominant noise process before other noise processes start to dominate the overall noise spectrum.

Shown in Fig. 6.13(d) is another Allan variance plot but for the highest measured power for the data shown in Fig. 6.13(a). This power level corresponds to an average photon number $\langle n \rangle \sim 250$. The noise amplitudes for white and $1/f$ noise were calculated for this data set and are also shown in Table 6.2. As would be expected, by increasing the power, the overall noise amplitudes have been reduced. The values in Table 6.2 show approximately an order of magnitude smaller noise amplitude for photon numbers of $\langle n \rangle \sim 250$ compared to lower photon numbers of $\langle n \rangle \sim 6$. Looking at Fig. 6.13(d), we see again that there is no clear $1/f$ level. Again, at longer time scales the data starts to increase upwards, due to random walk frequency noise becoming dominant. Also noticeable in Fig. 6.13(d) is a smoothed out 'bump' region around $\tau = 10$ s. This could be some other noise process that does not follow a simple power law rule but perhaps some noise process that is Lorentzian in nature [47].

Plotting the noise amplitudes over a frequency noise spectrum has been done for this data set as well and is shown in Fig. 6.13(e). Like Fig. 6.13(c), the white noise level does not quite match the data but can be explained by other dominant noise processes that are unable to be accounted for in the fit. What is interesting from this plot is that there is a more distinctive $1/f$ noise level in the data. Although, it does not have the exact $1/f$ gradient, likely due to other more dominant noise processes.

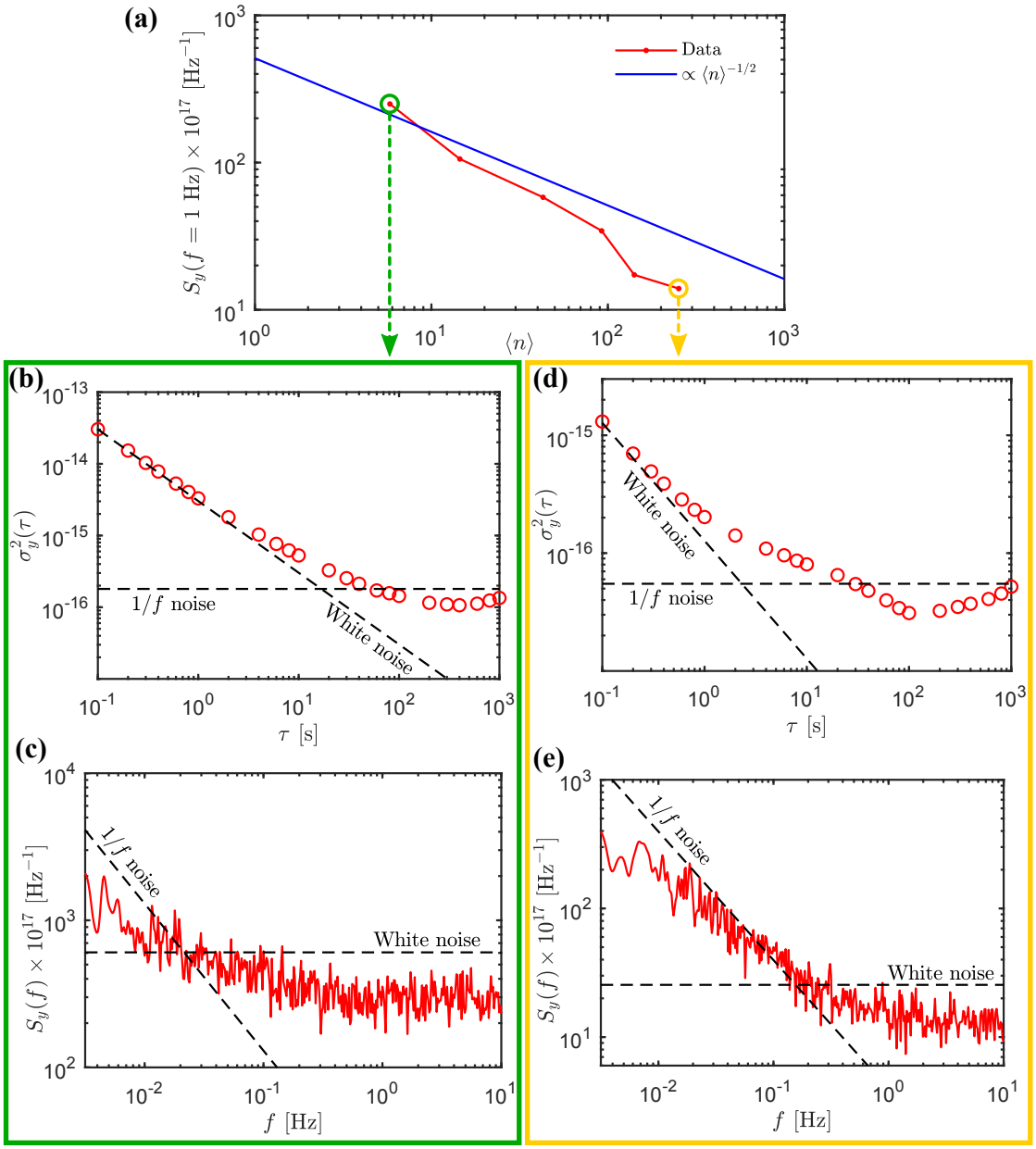

Figure 6.13: All these noise measurements were taken with Probe 16 whilst in the NSMM and far from the sample surface. They were calculated from the resonator frequency fluctuations over a long duration. **(a)** Plot of frequency noise at 1 Hz of 6 separate microwave scans as a function of the average photon number. The red line is data and the blue line is a fit to $S_y(f = 1\ \mathrm{Hz}) = A/\langle n \rangle^{1/2}$ where $A = 5.1 \times 10^{-15}$. **(b)** Allan variance $\sigma_y^2(\tau)$, measured at low power where $\langle n \rangle \sim 6$ (corresponding to the highlighted green data point of (a)). The dashed lines show the noise processes that were fitted to using Eq. (6.5). **(c)** The frequency noise spectrum $S_y(f)$, at $\langle n \rangle \sim 6$. The dashed lines show the noise processes as calculated from the corresponding Allan variance. **(d)** The Allan variance as calculated in (b) but at $\langle n \rangle \sim 250$ (corresponding to the highlighted yellow data point in (a)). **(e)** The frequency noise spectrum as calculated in (c) but at $\langle n \rangle \sim 250$. The dashed lines indicate the noise levels calculated from the corresponding Allan variance.

Chapter 7

Conclusions and Outlook

In this chapter, we present a summary of the main results and we discuss their significance and their contributions to the field of scanning probe microscopy and quantum technologies research. We then outline how the work can be taken further with recommendations on how to improve the experiment. We also discuss possible future applications of an NSMM that operates in the quantum regime.

The most significant result demonstrated in this thesis is that, for the first time, a microwave scan in the single photon regime was obtained. By using a superconducting resonator with a resonant frequency of 6 GHz as the NSMM probe, integrated with a quartz tuning fork for precise distance control, and suspending the NSMM in a DR operating at 30 mK. Dielectric contrast with an SNR of approximately 2 was achieved whilst scanning over a transmon qubit array sample. This is a promising result in developing scanning microscopy tools that can be used for measuring and coherently coupling to quantum systems and quantum devices. We have measured Q-factors of the order $Q_i \sim 10^5$. This is the highest measured Q_i for a resonant probe in an NSMM [57, 72, 75, 122].

We characterised the noise performance of the NSMM in detail, which allowed us to determine the mechanical noise levels, in particular at the frequency of the DR pulse tube. From these measurements, the peak amplitude dither of the tuning fork was calculated to be 1.8 nm which is a relatively small value when comparing to similar microscopes in the literature. For example, similar dry dilution refrigerator SPM experiments quote values of 15 nm [124], 0.7 µm [125] and 0.8 nm [126]. These values are comparable or much greater than the value measured in our NSMM.

By characterising the intrinsic frequency noise we found that the stability of the resonant NSMM probe due to TLS defects in the single photon regime was comparable to the magnitude of the mechanical noise. However, in the single photon regime, the limiting factor to the measured SNR was determined to be

the losses between the NSMM probe and the readout HEMT amplifier. Thus the most important alterations would be to reduce these losses while keeping a flexible microwave link to the suspended NSMM or introduce a parametric amplifier.

The NSMM has produced many interesting results and the first single photon regime scan using microwave radiation. Given this, there are still changes that could be made to the microscope to improve upon the design. For example, one major improvement would be to increase the thermalisation of the superconducting resonator probe so that it can reach temperatures of 10 mK. This can be done by bonding a wire to the resonator that connects to a well-thermalised part of the NSMM casing. Another improvement would be to move the springs that are used for the NSMM suspension from the 50 K plate to the 10 mK plate of the BlueFors dilution refrigerator. This will remove the need for the feed-through caps at the 800 mK plate and the Kevlar thread that goes through each stage of the cryostat, thus eliminating the heating effect from higher temperature photons.

The suspension itself could also be improved to minimise to effects of the pulse tube. Although the CuBe springs mechanically damp the NSMM, the system is not critically damped. By introducing Eddy current dampers [119] it would become possible to have a tunable suspension system through the use of a solenoid so that critical damping can be achieved. This would reduce the maximum peak amplitude of dither from the tuning fork. If all these improvements can be realised, the noise performance in the single photon regime would be limited by the intrinsic resonator frequency noise.

To conclude, the NSMM in the quantum regime shows great promise for the development of scanning probe microscopy systems that can coherently couple to quantum systems. Although design improvements can be made, the single photon scans presented here represent a significant milestone for the microwave characterisation of quantum technologies and devices.

Appendix A

Physics of NSMM-TLS Simulations

The simulations shown in Section 3.4.3 make use of "QuTip: Quantum Optics Toolbox", an open-source Python library for simulating the dynamics of quantum systems. This library comes pre-built will efficient solvers for calculating the dynamics of an NSMM-TLS interaction. This appendix discusses how the electric field is approximated that is required to compute the coupling strength g and also the calculations that the QuTip handles for calculating the power spectrum of the NSMM-TLS interaction.

Calculating the Coupling Strength

To fully model the NSMM-TLS interaction shown in Fig. 3.9, we need to have an understanding of how to model the coupling strength g, between the cavity (resonator) and a two-level system. The coupling factor in Jaynes-Cummings Hamiltonian in the RWA approximation (Eq. (3.14)) is dependent on the distance to the TLS and is given by

$$g(\mathbf{r}) = \frac{e}{\hbar\pi}\mathbf{E}(\mathbf{r}) \cdot \mathbf{d}, \tag{A.1}$$

where $\mathbf{E}$ is the electric field at the TLS and $\mathbf{d}$ is the electric dipole moment of the TLS and $\mathbf{r}$ is the tip-to-TLS vector. The form of $\mathbf{E}$ can not be analytically calculated. However, assuming the tip is a charged sphere, the electric field can be approximated by summing the contributions from each point charge on that sphere [59, 69]. This yields

$$\mathbf{E}(\mathbf{r}) = \frac{2r_{\text{tip}}V_0(\varepsilon_r - 1)}{(\varepsilon_r + 1)^2} \sum_{n=1}^{\infty} t_n \frac{r\hat{\mathbf{r}} + (h_\varepsilon + a_n r_{\text{tip}})\hat{\mathbf{z}}}{\left(r^2 + (h_\varepsilon + a_n r_{\text{tip}})^2\right)^{3/2}} \tag{A.2}$$

for the electric field in cylindrical polar co-ordinates. Here, the recursive coefficients in the summation are defined as $a_1 = (r_{\text{tip}} + h_0)/r_{\text{tip}}$, $a_n = a_1 - 1/(a_1 + a_{n-1})$ and $t_1 = 1$, $t_n = t_{n-1}/(a_1 + a_{n-1})$. The parameters h_ε, h_0 and r_{tip} are defined back in Fig. 3.9. V_0 is the voltage at the tip, for the case of an individual microwave photon, $V_0 = \sqrt{2\hbar\omega_0/C}$ where C is the total resonator probe capacitance. For the recursive calculations, we summed from $n = 1, 2, 3, \cdots 20$. This was found to be enough to calculate a convergent solution for the electric field about the tip.

Calculating the Power Spectrum

In order to produce a 2D map of an expected microwave scan of a TLS coupling to our resonator probe, we need to calculate the power spectrum $S(\omega)$ of the resonator probe as it couples to a TLS and the surrounding environment. We then can calculate the frequency shift $\Delta\omega = \omega - \omega_r$ of the resonance frequency of the probe. To do this, we use QuTip to evaluate

$$S(\omega) = \frac{1}{2\pi}\int_{-\infty}^{\infty} e^{i\omega\tau}\langle\hat{a}^\dagger(\tau + t)\hat{a}(t)\rangle d\tau, \tag{A.3}$$

where $\langle\hat{a}^\dagger(\tau + t)\hat{a}(t)\rangle$ is the two-time correlation function and $\hat{a}^\dagger$ and $\hat{a}$ are the creation and annihilation operators, respectively. The two-time correlation function and can be simplified using the relation [45]

$$\langle\hat{a}^\dagger(\tau + t)\hat{a}(t)\rangle = \text{Tr}\{\hat{a}^\dagger e^{\mathbf{L}\tau}\hat{a}\rho\}. \tag{A.4}$$

This simplification is utilised by QuTip. This equation introduces the density of states of the system ρ, and the Liouvillian operator $\mathbf{L}$. The time-evolution of the density matrix is described by the so-called Linblad Master Equation of the form $\dot{\rho} = \mathbf{L}\rho$, the full form of which can be expressed as

$$\dot{\rho} = -\frac{i}{\hbar}[\hat{H}, \rho] + \sum_{k=1}^{3}\left(\hat{C}_k\rho\hat{C}_k^\dagger - \tfrac{1}{2}\left(\hat{C}_k^\dagger\hat{C}_k\rho + \rho\hat{C}_k\hat{C}_k^\dagger\right)\right). \tag{A.5}$$

Here, $\hat{H}$ is the Jaynes-Cummings Hamiltonian (Eq. (3.14)) for the interaction between the resonator probe and the TLS. This Hamiltonian assumes that the RWA

is valid. The operators $\hat{C}_k$ are the so-called Lindblad operators and correspond to, in this case, three degrees of dissipation in the cavity-TLS system to the environment. They are defined as

- $\hat{C}_1 = \sqrt{\gamma_1}\hat{\sigma}^-$ where $\gamma_1 = 1/T_1$ is the relaxation from the excited state to the ground state of the TLS.
- $\hat{C}_2 = \sqrt{\frac{\gamma_\phi}{2}}\hat{\sigma}_z$ where $\gamma_\phi = 1/T_2 - 1/2T_1$ and T_2 is an exponential decay time of the pure dephasing of the TLS.
- $\hat{C}_3 = \sqrt{\kappa}\hat{a}$ where the cavity is losing energy at a rate $\kappa = \omega_r/Q$ leading to the destruction of photons in the resonator.

Equation (A.5) assumes that the interaction is Markovian (meaning a stochastic process where the current state is *only* dependent on the previous state) and temporally homogeneous.

It is generally difficult to model the dissipation of quantum systems with the environment. This equation, given some aforementioned assumptions, is able to model the interaction of the cavity-TLS system with the environment (through three dissipative channels), that cause decoherence of this quantum system.

Appendix B

PDH Error Signal Derivation

The details of the derivation of the PDH error signal ε, that were started in Chapter 5 are worked through here. The transmitted signal V_T, going through the resonator is described in Eq. (5.5). The signal is then passed through a power diode which has the effect of self mixing the signal and producing the transmitted power $P_T = V_T^2 = V_T V_T^*$ which leads to

$$\begin{aligned} P_T = V_0^2 \Big(& S_{21}(\omega_c) J_0(\beta) e^{i\omega_c t} + S_{21}(\omega_c + \omega_m) J_1(\beta) e^{i(\omega_c+\omega_m)t} \\ & - S_{21}(\omega_c - \omega_m) J_1(\beta) e^{i(\omega_c-\omega_m)t} \Big) \times \Big(S_{21}^*(\omega_c) J_0(\beta) e^{-i\omega_c t} + \\ & S_{21}^*(\omega_c + \omega_m) J_1(\beta) e^{-i(\omega_c+\omega_m)t} - S_{21}^*(\omega_c - \omega_m) J_1(\beta) e^{-i(\omega_c-\omega_m)t} \Big) . \end{aligned} \tag{B.1}$$

This is of the form $(a+b+c)^2 = a^2 + b^2 + c^2 + a^*b + ab^* + b^*c + bc^* + a^*c + ac^*$. Here the squared terms cancel one another out. The remaining terms leave only harmonics of the modulation angular frequency ω_m. Here we are only interested in the first order harmonics $\pm\omega_m$ (as a band pass filter removes the higher harmonics) and so terms for $\pm 2\omega_m$ or higher are neglected. This then simplifies to

$$\begin{aligned} P_T = & J_0(\beta) J_1(\beta) V_0^2 \times \\ & \Big(S_{21}(\omega_c) S_{21}^*(\omega_c + \omega_m) e^{-i\omega_m t} + S_{21}^*(\omega_c) S_{21}(\omega_c + \omega_m) e^{i\omega_m t} \\ & - S_{21}(\omega_c) S_{21}^*(\omega_c - \omega_m) e^{-i\omega_m t} - S_{21}^*(\omega_c) S_{21}(\omega_c - \omega_m) e^{i\omega_m t} \Big). \end{aligned} \tag{B.2}$$

This equation can be expanded by using the relation $e^{i\theta} = \cos\theta + i\sin\theta$ which gives

$$
\begin{aligned}
P_T = {} & J_0(\beta)J_1(\beta)V_0^2\times \\
& \Big(S_{21}(\omega_c)S_{21}^*(\omega_c+\omega_m)\cos(\omega_m t) + iS_{21}(\omega_c)S_{21}^*(\omega_c+\omega_m)\sin(\omega_m t) \\
& +S_{21}^*(\omega_c)S_{21}(\omega_c+\omega_m)\cos(\omega_m t) + iS_{21}^*(\omega_c)S_{21}(\omega_c+\omega_m)\sin(\omega_m t) \\
& -S_{21}(\omega_c)S_{21}^*(\omega_c-\omega_m)\cos(\omega_m t) - iS_{21}(\omega_c)S_{21}^*(\omega_c-\omega_m)\sin(\omega_m t) \\
& -S_{21}^*(\omega_c)S_{21}(\omega_c-\omega_m)\cos(\omega_m t) - iS_{21}^*(\omega_c)S_{21}(\omega_c-\omega_m)\sin(\omega_m t)\Big).
\end{aligned}
\tag{B.3}
$$

Now the real and imaginary parts of the S_{21} parameters can be evaluated. Doing so cancels out the cosine terms, leaving us with

$$
\begin{aligned}
P_T = {} & J_0(\beta)J_1(\beta)V_0^2\sin(\omega_m t)\times \\
& \Big(\mathrm{Re}S_{21}(\omega_c)\mathrm{Im}S_{21}(\omega_c+\omega_m) - \mathrm{Im}S_{21}(\omega_c)\mathrm{Re}S_{21}(\omega_c+\omega_m) \\
& +\mathrm{Re}S_{21}(\omega_c)\mathrm{Im}S_{21}(\omega_c-\omega_m) - \mathrm{Im}S_{21}(\omega_c)\mathrm{Re}S_{21}(\omega_c-\omega_m) \\
& +\mathrm{Re}S_{21}(\omega_c)\mathrm{Im}S_{21}(\omega_c+\omega_m) - \mathrm{Im}S_{21}(\omega_c)\mathrm{Re}S_{21}(\omega_c+\omega_m) \\
& +\mathrm{Re}S_{21}(\omega_c)\mathrm{Im}S_{21}(\omega_c-\omega_m) - \mathrm{Im}S_{21}(\omega_c)\mathrm{Re}S_{21}(\omega_c-\omega_m)\Big)
\end{aligned}
\tag{B.4}
$$

then simplifying this gives

$$
\begin{aligned}
P_T = {} & 2J_0(\beta)J_1(\beta)V_0^2\sin(\omega_m t)\times \\
& \Big(\mathrm{Re}S_{21}(\omega_c)\Big[\mathrm{Im}S_{21}(\omega_c+\omega_m) + \mathrm{Im}S_{21}(\omega_c+\omega_m)\Big] \\
& -\mathrm{Im}S_{21}(\omega_c)\Big[\mathrm{Re}S_{21}(\omega_c+\omega_m) + \mathrm{Re}S_{21}(\omega_c+\omega_m)\Big]\Big).
\end{aligned}
\tag{B.5}
$$

Passing this signal through a lock-in amplifier that has a reference signal with a frequency equal to ω_m removes the sine term leaving the final resulting signal stated back in Chapter 5 of

$$
\begin{aligned}
\varepsilon \propto {} & 2J_0(\beta)J_1(\beta)V_0^2\Big(\mathrm{Re}S_{21}(\omega_c)\Big[\mathrm{Im}S_{21}(\omega_c+\omega_m) + \mathrm{Im}S_{21}(\omega_c-\omega_m)\Big] \\
& -\mathrm{Im}S_{21}(\omega_c)\Big[\mathrm{Re}S_{21}(\omega_c+\omega_m) + \mathrm{Re}S_{21}(\omega_c-\omega_m)\Big]\Big).
\end{aligned}
\tag{B.6}
$$

References

[1] R. Bedington, J. M. Arrazola, and A. Ling, "Progress in satellite quantum key distribution," *npj Quantum Inf.*, vol. 3, p. 30, dec 2017.

[2] V. I. Yudin and A. V. Taichenachev, "About the possibility of cosmological gravimetry using high-precision atomic clocks in nonmetric theories of gravitation," in *AIP Conf. Proc.*, vol. 2098, p. 020017, AIP Publishing LLC, apr 2019.

[3] A. McGurn, "Quantum computers," *Springer Ser. Opt. Sci.*, vol. 213, pp. 491–544, 2018.

[4] P. W. Shor, "Polynomial-time algorithms for prime factorization and discrete logarithms on a quantum computer," *SIAM J. Comput.*, vol. 26, pp. 1484–1509, aug 1997.

[5] M. Carrel-Billiard, D. Garrison, and C. Dukatz, "Think Beyond Ones and Zeros Quantum Computing. Now.," tech. rep., Accenture, 2017.

[6] M. W. Johnson, M. H. Amin, S. Gildert, T. Lanting, F. Hamze, N. Dickson, R. Harris, A. J. Berkley, J. Johansson, P. Bunyk, E. M. Chapple, C. Enderud, J. P. Hilton, K. Karimi, E. Ladizinsky, N. Ladizinsky, T. Oh, I. Perminov, C. Rich, M. C. Thom, E. Tolkacheva, C. J. Truncik, S. Uchaikin, J. Wang, B. Wilson, and G. Rose, "Quantum annealing with manufactured spins," *Nature*, vol. 473, pp. 194–198, may 2011.

[7] Julian Kelly, "A Preview of Bristlecone, Google's New Quantum Processor," 2018.

[8] D. Castelvecchi, "IBM's quantum cloud computer goes commercial," *Nature*, vol. 543, p. 159, mar 2017.

[9] J. S. Otterbach, R. Manenti, N. Alidoust, A. Bestwick, M. Block, B. Bloom, S. Caldwell, N. Didier, E. S. Fried, S. Hong, P. Karalekas, C. B. Osborn, A. Papageorge, E. C. Peterson, G. Prawiroatmodjo, N. Rubin, C. A. Ryan, D. Scarabelli, M. Scheer, E. A. Sete, P. Sivarajah, R. S. Smith, A. Staley, N. Tezak, W. J. Zeng, A. Hudson, B. R. Johnson, M. Reagor, M. P. da Silva, and C. Rigetti, "Unsupervised Machine Learning on a Hybrid Quantum Computer," 2017.

[10] D. P. DiVincenzo, "The physical implementation of quantum computation," *Fortschritte der Phys.*, vol. 48, pp. 771–783, feb 2000.

[11] G. Ithier, E. Collin, P. Joyez, P. J. Meeson, D. Vion, D. Esteve, F. Chiarello, A. Shnirman, Y. Makhlin, J. Schriefl, and G. Schön, "Decoherence in a superconducting quantum bit circuit," *Phys. Rev. B - Condens. Matter Mater. Phys.*, vol. 72, p. 134519, oct 2005.

[12] J. M. Martinis, K. B. Cooper, R. McDermott, M. Steffen, M. Ansmann, K. D. Osborn, K. Cicak, S. Oh, D. P. Pappas, R. W. Simmonds, and C. C. Yu, "Decoherence in Josephson qubits from dielectric Loss," *Phys. Rev. Lett.*, vol. 95, no. 21, 2005.

[13] E. Paladino, Y. Galperin, G. Falci, and B. L. Altshuler, "1/ f noise: Implications for solid-state quantum information," *Rev. Mod. Phys.*, vol. 86, pp. 361–418, apr 2014.

[14] J. Hoffmann, "Nearfield scanning microwave microscopes," in *CPEM Dig. (Conference Precis. Electromagn. Meas.*, pp. 218–219, IEEE, aug 2014.

[15] S. M. Anlage, V. V. Talanov, and A. R. Schwartz, "Principles of near-field microwave microscopy," in *Scanning Probe Microsc.*, vol. 2, ch. I.7, pp. 215–253, New York, NY: Springer New York, 2007.

[16] R. Kalra, A. Laucht, J. P. Dehollain, D. Bar, S. Freer, S. Simmons, J. T. Muhonen, and A. Morello, "Vibration-induced electrical noise in a cryogen-free dilution refrigerator: Characterization, mitigation, and impact on qubit coherence," *Rev. Sci. Instrum.*, vol. 87, no. 7, 2016.

[17] S. E. De Graaf, A. V. Danilov, and S. E. Kubatkin, "Coherent interaction with two-level fluctuators using near field scanning microwave microscopy," *Sci. Rep.*, vol. 5, no. 17176, 2015.

[18] G. Wendin and V. S. Shumeiko, "Superconducting Quantum Circuits, Qubits and Computing," *ArXiv*, vol. 3, 2005.

[19] S. E. de Graaf, *Fractal superconducting resonators for the interrogation of two-level systems.* PhD thesis, Chalmers University of Technology, Gothenburg, 2014.

[20] J. C. Gallop, *Introduction to Superconductivity.* McGraw-Hill, 2nd ed., 2018.

[21] O. Klein, "Theory of Superconductivity," *Nature*, vol. 169, no. 4301, pp. 578–579, 1952.

[22] B. D. Josephson, "Possible new effects in superconductive tunnelling," *Phys. Lett.*, vol. 1, no. 7, pp. 251–253, 1962.

[23] J. Q. You and F. Nori, "Superconducting circuits and quantum information," *Phys. Today*, vol. 58, pp. 42–47, nov 2005.

[24] J. G. Webster, E. Il'ichev, and G. Oelsner, "Superconducting Qubits," *Wiley Encycl. Electr. Electron. Eng.*, pp. 1–13, may 2018.

[25] P. Krantz, M. Kjaergaard, F. Yan, T. P. Orlando, S. Gustavsson, and W. D. Oliver, "A quantum engineer's guide to superconducting qubits," *Appl. Phys. Rev.*, vol. 6, p. 021318, apr 2019.

[26] Y. Nakamura, Y. A. Pashkin, and J. S. Tsai, "Coherent control of macroscopic quantum states in a single-Cooper-pair box," *Nature*, vol. 398, pp. 786–788, apr 1999.

[27] J. Koch, T. M. Yu, J. Gambetta, A. A. Houck, D. I. Schuster, J. Majer, A. Blais, M. H. Devoret, S. M. Girvin, and R. J. Schoelkopf, "Charge-insensitive qubit design derived from the Cooper pair box," *Phys. Rev. A - At. Mol. Opt. Phys.*, vol. 76, p. 042319, oct 2007.

[28] P. Krantz, *Investigation of Transmon Qubit Designs*. PhD thesis, Chalmers University of Technology, 2010.

[29] C. Müller, J. H. Cole, and J. Lisenfeld, "Towards understanding two-level-systems in amorphous solids - Insights from quantum circuits," *ArXiv*, may 2017.

[30] W. A. Phillips, "Two-level states in glasses," *Reports Prog. Phys.*, vol. 50, pp. 1657–1708, dec 1987.

[31] P. W. Anderson, B. I. Halperin, and C. M. Varma, "Anomalous low-temperature thermal properties of glasses and spin glasses," *Philos. Mag.*, vol. 25, pp. 1–9, jan 1972.

[32] K. S. Gilkoy and W. A. Phillips, "An asymmetric double-well potential model for structural relaxation processes in amorphous materials," *Philos. Mag. B Phys. Condens. Matter; Stat. Mech. Electron. Opt. Magn. Prop.*, vol. 43, pp. 735–746, may 1981.

[33] J. Lisenfeld, G. J. Grabovskij, C. Müller, J. H. Cole, G. Weiss, and A. V. Ustinov, "Observation of directly interacting coherent two-level systems in an amorphous material," *Nat. Commun.*, vol. 6, p. 6182, 2015.

[34] L. Faoro and L. B. Ioffe, "Interacting tunneling model for two-level systems in amorphous materials and its predictions for their dephasing and noise in superconducting microresonators," *Phys. Rev. B - Condens. Matter Mater. Phys.*, vol. 91, p. 014201, jan 2015.

[35] K. B. Cooper, M. Steffen, R. McDermott, R. W. Simmonds, S. Oh, D. A. Hite, D. P. Pappas, and J. M. Martinis, "Observation of Quantum Oscillations between a Josephson Phase Qubit and a Microscopic Resonator Using Fast Readout," *Phys. Rev. Lett.*, vol. 93, p. 180401, oct 2004.

[36] Y. Shalibo, Y. Rofe, D. Shwa, F. Zeides, M. Neeley, J. M. Martinis, and N. Katz, "Lifetime and coherence of two-level defects in a Josephson junction," *Phys. Rev. Lett.*, vol. 105, p. 177001, oct 2010.

[37] J. Burnett, L. Faoro, I. Wisby, V. L. Gurtovoi, A. V. Chernykh, G. M. Mikhailov, V. A. Tulin, R. Shaikhaidarov, V. Antonov, P. J. Meeson, A. Y. Tzalenchuk, and T. Lindström, "Evidence for interacting two-level systems from the 1/f noise of a superconducting resonator," *Nat. Commun.*, vol. 5, p. 4119, dec 2014.

[38] J. Burnett, L. Faoro, and T. Lindström, "Analysis of high quality superconducting resonators: Consequences for TLS properties in amorphous oxides," *Supercond. Sci. Technol.*, vol. 29, pp. 1–8, apr 2016.

[39] J. Goetz, F. Deppe, M. Haeberlein, F. Wulschner, C. W. Zollitsch, S. Meier, M. Fischer, P. Eder, E. Xie, K. G. Fedorov, E. P. Menzel, A. Marx, and R. Gross, "Loss mechanisms in superconducting thin film microwave resonators," *J. Appl. Phys.*, vol. 119, p. 015304, jan 2016.

[40] S. E. De Graaf, L. Faoro, J. Burnett, A. A. Adamyan, A. Y. Tzalenchuk, S. E. Kubatkin, T. Lindström, and A. V. Danilov, "Suppression of low-frequency charge noise in superconducting resonators by surface spin desorption," *Nat. Commun.*, vol. 9, p. 1143, dec 2018.

[41] T. Lindström, J. E. Healey, M. S. Colclough, C. M. Muirhead, and A. Y. Tzalenchuk, "Properties of superconducting planar resonators at millikelvin temperatures," *Phys. Rev. B - Condens. Matter Mater. Phys.*, vol. 80, p. 132501, oct 2009.

[42] C. Deng, M. Otto, and A. Lupascu, "Characterization of low-temperature microwave loss of thin aluminum oxide formed by plasma oxidation," *Appl. Phys. Lett.*, vol. 104, p. 043506, jan 2014.

[43] J. Burnett, A. Bengtsson, D. Niepce, and J. Bylander, "Noise and loss of superconducting aluminium resonators at single photon energies," *J. Phys. Conf. Ser.*, vol. 969, p. 012131, mar 2018.

[44] M. J. Stoutimore, M. S. Khalil, C. J. Lobb, and K. D. Osborn, "A Josephson junction defect spectrometer for measuring two-level systems," *Appl. Phys. Lett.*, vol. 101, p. 062602, aug 2012.

[45] T. Lindström, C. H. Webster, J. E. Healey, M. S. Colclough, C. M. Muirhead, and A. Y. Tzalenchuk, "Circuit QED with a flux qubit strongly coupled to a coplanar transmission line resonator," *Supercond. Sci. Technol.*, vol. 20, no. 8, pp. 814–821, 2007.

[46] S. Schlör, J. Lisenfeld, C. Müller, A. Bilmes, A. Schneider, D. P. Pappas, A. V. Ustinov, and M. Weides, "Correlating Decoherence in Transmon Qubits: Low Frequency Noise by Single Fluctuators," *Phys. Rev. Lett.*, vol. 123, jan 2019.

[47] J. Burnett, A. Bengtsson, M. Scigliuzzo, D. Niepce, M. Kudra, P. Delsing, and J. Bylander, "Decoherence benchmarking of superconducting qubits," *npj Quantum Inf.*, vol. 5, jan 2019.

[48] D. W. Allan, "Should the Classical Variance Be Used As a Basic Measure in Standards Metrology?," *IEEE Trans. Instrum. Meas.*, vol. IM-36, pp. 646–654, jun 1987.

[49] D. Reymann and T. Witt, "Using power spectra and Allan variances to characterise the noise of Zener-diode voltage standards," *IEE Proc. - Sci. Meas. Technol.*, vol. 147, pp. 177–182, jul 2000.

[50] S. P. Giblin and G. Lorusso, "Exploring a new ammeter traceability route for ionisation chamber measurements," *Rev. Sci. Instrum.*, vol. 90, p. 014705, jan 2019.

[51] T. Lindström, J. Burnett, M. Oxborrow, and A. Y. Tzalenchuk, "Pound-locking for characterization of superconducting microresonators," *Rev. Sci. Instrum.*, vol. 82, no. 10, p. 104706, 2011.

[52] E. Rubiola, *Phase noise and frequency stability in oscillators*, vol. 9780521886. Cambridge University Press, 2008.

[53] E. Synge, " XXXVIII. A suggested method for extending microscopic resolution into the ultra-microscopic region ," *London, Edinburgh, Dublin Philos. Mag. J. Sci.*, vol. 6, no. 35, pp. 356–362, 1928.

[54] J. A. O'Keefe, "Resolving Power of Visible Light," *J. Opt. Soc. Am.*, vol. 46, p. 359, may 1956.

[55] E. A. Ash and G. Nicholls, "Super-resolution aperture scanning microscope," *Nature*, vol. 237, no. 5357, pp. 510–512, 1972.

[56] C. P. Vlahacos, D. E. Steinhauer, S. K. Dutta, B. J. Feenstra, S. M. Anlage, and F. C. Wellstood, "Quantitative topographic imaging using a near-field scanning microwave microscope," *Appl. Phys. Lett.*, vol. 72, no. 14, pp. 1778–1780, 1998.

[57] A. Gregory, L. Hao, N. Klein, J. Gallop, C. Mattevi, O. Shaforost, K. Lees, and B. Clarke, "Spatially resolved electrical characterisation of graphene layers by an evanescent field microwave microscope," *Phys. E Low-Dimensional Syst. Nanostructures*, vol. 56, pp. 431–434, 2014.

[58] D. W. Van Der Weide, "Localized picosecond resolution with a near-field microwave/scanning-force microscope," *Appl. Phys. Lett.*, vol. 70, pp. 677–679, jun 1997.

[59] C. Gao and X. D. Xiang, "Quantitative microwave near-field microscopy of dielectric properties," *Rev. Sci. Instrum.*, vol. 69, no. 11, pp. 3846–3851, 1998.

[60] S. C. Lee, C. P. Vlahacos, B. J. Feenstra, A. Schwartz, D. E. Steinhauer, F. C. Wellstood, and S. M. Anlage, "Magnetic permeability imaging of metals with a scanning near-field microwave microscope," *Appl. Phys. Lett.*, vol. 77, pp. 4404–4406, dec 2000.

[61] R. E. Glover and M. Tinkham, "Transmission of Superconducting Films at Millimeter-Microwave and Far Infrared Frequencies," *Phys. Rev.*, vol. 104, no. 3, pp. 844–845, 1956.

[62] L. H. Palmer and M. Tinkham, "Far-Infrared Absorption in Thin Superconducting Lead Films," *Phys. Rev.*, vol. 165, no. 2, 1968.

[63] A. F. Lann, M. Abu-Teir, M. Golosovsky, D. Davidov, A. Goldgirsch, and V. Beilin, "Magnetic-field-modulated microwave reflectivity of high- Tcsuperconductors studied by near-field mm-wave microscopy," *Appl. Phys. Lett.*, vol. 75, pp. 1766–1768, sep 1999.

[64] A. Imtiaz, T. M. Wallis, S. H. Lim, H. Tanbakuchi, H. P. Huber, A. Hornung, P. Hinterdorfer, J. Smoliner, F. Kienberger, and P. Kabos, "Frequency-selective contrast on variably doped p-type silicon with a scanning microwave microscope," *J. Appl. Phys.*, vol. 111, no. 9, p. 093727, 2012.

[65] H. P. Huber, M. Moertelmaier, T. M. Wallis, C. J. Chiang, M. Hochleitner, A. Imtiaz, Y. J. Oh, K. Schilcher, M. Dieudonne, J. Smoliner, P. Hinterdorfer, S. J. Rosner, H. Tanbakuchi, P. Kabos, and F. Kienberger, "Calibrated nanoscale capacitance measurements using a scanning microwave microscope," *Rev. Sci. Instrum.*, vol. 81, no. 11, p. 113701, 2010.

[66] X. Wu and O. M. Ramahi, "Near-field scanning microwave microscopy for detection of subsurface biological anomalies," in *IEEE Antennas Propag. Soc. AP-S Int. Symp.*, vol. 3, pp. 2444–2447, IEEE, 2004.

[67] S. Kim, Y. Jang, S. Kim, T. D. Kim, H. Melikyan, A. Babajanyan, K. Lee, and B. Friedman, "Detection of DNA-hybridization using a near-field scanning microwave microscope," *J. Nanosci. Nanotechnol.*, vol. 11, pp. 4222–4226, may 2011.

[68] X. Wu, Z. Hao, D. Wu, L. Zheng, Z. Jiang, V. Ganesan, Y. Wang, and K. Lai, "Quantitative measurements of nanoscale permittivity and conductivity using tuning-fork-based microwave impedance microscopy," *Rev. Sci. Instrum.*, vol. 89, p. 043704, apr 2018.

[69] S. E. De Graaf, A. V. Danilov, A. Adamyan, and S. E. Kubatkin, "A near-field scanning microwave microscope based on a superconducting resonator for low power measurements," *Rev. Sci. Instrum.*, vol. 84, no. 2, p. 023706, 2013.

[70] I. Takeuchi, T. Wei, F. Duewer, Y. K. Yoo, X. D. Xiang, V. Talyansky, S. P. Pai, G. J. Chen, and T. Venkatesan, "Low temperature scanning-tip microwave near-field microscopy of YBa2Cu3O7-x films," *Appl. Phys. Lett.*, vol. 71, no. 14, pp. 2026–2028, 1997.

[71] W. Kundhikanjana, K. Lai, M. A. Kelly, and Z. X. Shen, "Cryogenic microwave imaging of metal-insulator transition in doped silicon," *Rev. Sci. Instrum.*, vol. 82, no. 3, p. 033705, 2011.

[72] H. Takahashi, Y. Imai, and A. Maeda, "Low-temperature-compatible tunneling-current-assisted scanning microwave microscope utilizing a rigid coaxial resonator," *Rev. Sci. Instrum.*, vol. 87, p. 063706, jun 2016.

[73] Y. Shperber, N. Vardi, E. Persky, S. Wissberg, M. E. Huber, and B. Kalisky, "Scanning SQUID microscopy in a cryogen-free cooler," *Rev. Sci. Instrum.*, vol. 90, p. 053702, may 2019.

[74] Y. J. Song, A. F. Otte, V. Shvarts, Z. Zhao, Y. Kuk, S. R. Blankenship, A. Band, F. M. Hess, and J. A. Stroscio, "Invited Review Article: A 10 mK

scanning probe microscopy facility," *Rev. Sci. Instrum.*, vol. 81, p. 121101, dec 2010.

[75] A. Hovsepyan, H. Lee, T. Sargsyan, H. Melikyan, Y. Yoon, A. Babajanyan, B. Friedman, and K. Lee, "Characterization of Alq3 thin films by a near-field microwave microprobe," *Ultramicroscopy*, vol. 108, pp. 1058–1061, sep 2008.

[76] J. C. Weber, J. B. Schlager, N. A. Sanford, A. Imtiaz, T. M. Wallis, L. M. Mansfield, K. J. Coakley, K. A. Bertness, P. Kabos, and V. M. Bright, "A near-field scanning microwave microscope for characterization of inhomogeneous photovoltaics," *Rev. Sci. Instrum.*, vol. 83, p. 083702, aug 2012.

[77] A. Imtiaz, T. M. Wallis, and P. Kabos, "Near-field scanning microwave microscopy: An emerging research tool for nanoscale metrology," *IEEE Microw. Mag.*, vol. 15, no. 1, pp. 52–64, 2014.

[78] M. J. Yoo, T. A. Fulton, H. F. Hess, R. L. Willett, L. N. Dunkleberger, R. J. Chichester, L. N. Pfeiffer, and K. W. West, "Scanning single-electron transistor microscopy: Imaging individual charges," *Science (80-.).*, vol. 276, pp. 579–582, apr 1997.

[79] G. J. Sloggett, N. G. Barton, and S. J. Spencer, "Fringing fields in disc capacitors," *J. Phys. A. Math. Gen.*, vol. 19, pp. 2725–2736, oct 1986.

[80] C. Gao, F. Duewer, and X. D. Xiang, "Quantitative microwave evanescent microscopy," *Appl. Phys. Lett.*, vol. 75, pp. 3005–3007, nov 1999.

[81] S. Hudlet, M. Saint Jean, C. Guthmann, and J. Berger, "Evaluation of the capacitive force between an atomic force microscopy tip and a metallic surface," *Eur. Phys. J. B*, vol. 2, pp. 5–10, apr 1998.

[82] P. Kruse, *Scanning Probe Microscopy: The Lab on a Tip*, vol. 135. Heidelberg: Springer, 1 ed., 2004.

[83] B. T. Rosner and D. W. Van Der Weide, "High-frequency near-field microscopy," *Rev. Sci. Instrum.*, vol. 73, p. 2505, jun 2002.

[84] K. Karraï and R. D. Grober, "Piezo-electric tuning fork tip-sample distance control for near field optical microscopes," *Ultramicroscopy*, vol. 61, pp. 197–205, apr 1995.

[85] J. Senzier, P. S. Luo, and H. Courtois, "Combined scanning force microscopy and scanning tunneling spectroscopy of an electronic nanocircuit at very low temperature," *Appl. Phys. Lett.*, vol. 90, p. 043114, jan 2007.

[86] J.-M. Friedt and É. Carry, "Introduction to the quartz tuning fork," *Am. J. Phys.*, vol. 75, no. 5, pp. 415–422, 2007.

[87] R. D. Grober, J. Acimovic, J. Schuck, D. Hessman, P. J. Kindlemann, J. Hespanha, A. S. Morse, K. Karrai, I. Tiemann, and S. Manus, "Fundamental limits to force detection using quartz tuning forks," *Rev. Sci. Instrum.*, vol. 71, no. 7, pp. 2776–2780, 2000.

[88] K. Karrai, "Lecture notes on shear and friction force detection with quartz tuning forks," in *Proc.'Ecole Themat. CNRS'on Near-f. Opt. (La Londe les Maures, Fr.*, no. March, (La Londe les Maures, France), pp. 00–03, 2000.

[89] R. Ferguson, "Integrated circuits and microprocessors," in *Endeavour* (D. G. Fink and D. Christiansen, eds.), vol. 11, ch. 8, p. 106, McGraw-Hill Book Company, 3rd ed., 1987.

[90] F. Persson, *Fast dynamics and measurements of single-charge devices*. PhD thesis, Chalmers University of Technology, 2010.

[91] A. Blais, R. S. Huang, A. Wallraff, S. M. Girvin, and R. J. Schoelkopf, "Cavity quantum electrodynamics for superconducting electrical circuits: An architecture for quantum computation," *Phys. Rev. A - At. Mol. Opt. Phys.*, vol. 69, p. 062320, jun 2004.

[92] M. Boissonneault, J. M. Gambetta, and A. Blais, "Nonlinear dispersive regime of cavity QED: The dressed dephasing model," *Phys. Rev. A - At. Mol. Opt. Phys.*, vol. 77, no. 6, 2008.

[93] J. R. Johansson and P. D. Nation, "QuTiP: A framework for the dynamics of open quantum systems using SciPy and Cython," *Proc. 11th Python Sci. Conf.*, no. Scipy, pp. 56–61, 2012.

[94] J. R. Johansson, P. D. Nation, and F. Nori, "QuTiP 2: A Python framework for the dynamics of open quantum systems," *Comput. Phys. Commun.*, vol. 184, pp. 1234–1240, apr 2013.

[95] T. Lindström, C. H. Webster, J. E. Healey, M. S. Colclough, C. M. Muirhead, and A. Y. Tzalenchuk, "Numerical simulations of a flux qubit coupled to a high quality resonator," *J. Phys. Conf. Ser.*, vol. 97, p. 012319, feb 2008.

[96] B. A. Mazin, *Microwave Kinetic Inductance Detectors*. PhD thesis, California Institute of Technology, 2004.

[97] P. K. Day, H. G. LeDuc, B. A. Mazin, A. Vayonakis, and J. Zmuidzinas, "A broadband superconducting detector suitable for use in large arrays," *Nature*, vol. 425, pp. 817–821, oct 2003.

[98] A. A. Houck, H. E. Türeci, and J. Koch, "On-chip quantum simulation with superconducting circuits," *Nat. Phys.*, vol. 8, no. 4, pp. 292–299, 2012.

[99] M. Göppl, A. Fragner, M. Baur, R. Bianchetti, S. Filipp, J. M. Fink, P. J. Leek, G. Puebla, L. Steffen, and A. Wallraff, "Coplanar waveguide resonators for circuit quantum electrodynamics," *J. Appl. Phys.*, vol. 104, p. 113904, dec 2008.

[100] A. Wallraff, D. I. Schuster, A. Blais, L. Frunzio, R. S. Huang, J. Majer, S. Kumar, S. M. Girvin, and R. J. Schoelkopf, "Strong coupling of a single photon to a superconducting qubit using circuit quantum electrodynamics," *Nature*, vol. 431, pp. 162–167, sep 2004.

[101] M. Baur, A. Fedorov, L. Steffen, S. Filipp, M. P. Da Silva, and A. Wallraff, "Benchmarking a quantum teleportation protocol in superconducting circuits using tomography and an entanglement witness," *Phys. Rev. Lett.*, vol. 108, p. 040502, jan 2012.

[102] J. Majer, J. M. Chow, J. M. Gambetta, J. Koch, B. R. Johnson, J. A. Schreier, L. Frunzio, D. I. Schuster, A. A. Houck, A. Wallraff, A. Blais, M. H. Devoret, S. M. Girvin, and R. J. Schoelkopf, "Coupling superconducting qubits via a cavity bus," *Nature*, vol. 449, pp. 443–447, sep 2007.

[103] A. Wallraff, D. I. Schuster, A. Blais, L. Frunzio, J. Majer, M. H. Devoret, S. M. Girvin, and R. J. Schoelkopf, "Approaching unit visibility for control of a superconducting qubit with dispersive readout," *Phys. Rev. Lett.*, vol. 95, p. 060501, aug 2005.

[104] J. Zmuidzinas, "Superconducting Microresonators: Physics and Applications," *Annu. Rev. Condens. Matter Phys.*, vol. 3, no. 1, pp. 169–214, 2012.

[105] J. M. Sage, V. Bolkhovsky, W. D. Oliver, B. Turek, and P. B. Welander, "Study of loss in superconducting coplanar waveguide resonators," *J. Appl. Phys.*, vol. 109, no. 6, pp. 2286–102507, 2011.

[106] David Pozar, *Microwave engennering.* John Wiley & Sons, 4 ed., 1385.

[107] D. Kajfez and P. Guillon, *Dielectric Resonators*, vol. 10. SciTec, second ed., 1939.

[108] M. S. Khalil, M. J. Stoutimore, F. C. Wellstood, and K. D. Osborn, "An analysis method for asymmetric resonator transmission applied to superconducting devices," *J. Appl. Phys.*, vol. 111, no. 5, 2012.

[109] R. Barends, *Photon-detecting superconducting resonators.* PhD thesis, Delft University of Technology, 2009.

[110] A. Megrant, C. Neill, R. Barends, B. Chiaro, Y. Chen, L. Feigl, J. Kelly, E. Lucero, P. J. J. O. Malley, D. Sank, A. Vainsencher, J. Wenner, T. C. White, Y. Yin, J. Zhao, J. M. Martinis, and A. N. Cleland, "Planar Superconducting Resonators with Internal Quality Factors above One Million," *ArXiv*, vol. 100, no. 113510, pp. 1–4, 2012.

[111] J. Burnett, T. Lindström, M. Oxborrow, Y. Harada, Y. Sekine, P. Meeson, and A. Y. Tzalenchuk, "Slow noise processes in superconducting resonators," *Phys. Rev. B - Condens. Matter Mater. Phys.*, vol. 87, p. 140501, apr 2013.

[112] J. Wenner, R. Barends, R. C. Bialczak, Y. Chen, J. Kelly, E. Lucero, M. Mariantoni, A. Megrant, P. J. O'Malley, D. Sank, A. Vainsencher, H. Wang, T. C. White, Y. Yin, J. Zhao, A. N. Cleland, and J. M. Martinis, "Surface loss simulations of superconducting coplanar waveguide resonators," *Appl. Phys. Lett.*, vol. 99, p. 113513, sep 2011.

[113] S. Matityahu, A. Shnirman, G. Schön, and M. Schechter, "Decoherence of a quantum two-level system by spectral diffusion," *Phys. Rev. B*, vol. 93, no. 13, p. 134208, 2016.

[114] I. Wisby, *Hybrid rare-earth ion superconductor systems for quantum information processing.* PhD thesis, Royal Holloway University of London, 2017.

[115] J. Bardeen, "Two-fluid model of superconductivity," *Phys. Rev. Lett.*, vol. 1, pp. 399–400, dec 1958.

[116] K. Yoshida, K. Watanabe, T. Kisu, and K. Enpuku, "Evaluation of Magnetic Penetration Depth and Surface Resistance of Superconducting Thin Films using Coplanar Waveguides," *IEEE Trans. Appl. Supercond.*, vol. 5, pp. 1979–1982, jun 1995.

[117] S. E. De Graaf, A. V. Danilov, A. Adamyan, T. Bauch, and S. E. Kubatkin, "Magnetic field resilient superconducting fractal resonators for coupling to free spins," *J. Appl. Phys.*, vol. 112, p. 123905, dec 2012.

[118] A. Adamyan, *Slow propagation line-based superconducting devices for quantum technology.* PhD thesis, Chalmers University of Technology, 2016.

[119] G. Donoso, C. L. Ladera, and P. Martín, "Damped fall of magnets inside a conducting pipe," *Am. J. Phys.*, vol. 79, pp. 193–200, feb 2011.

[120] E. D. Black, "An introduction to Pound–Drever–Hall laser frequency stabilization," *Am. J. Phys.*, vol. 69, no. 1, pp. 79–87, 2001.

[121] T. Hönigl-Decrinis, *Quantum Optics on Artificial Quantum Media - Research - Royal Holloway, University of London*. PhD thesis, Royal Holloway, University of London, 2018.

[122] B. A. Bagdad and C. Lozano, "Near-field scanning microwave microscope platform based on a coaxial cavity resonator for the characterization of semiconductor structures," *Solid. State. Electron.*, vol. 159, pp. 150–156, sep 2019.

[123] P. V. Klimov, J. Kelly, Z. Chen, M. Neeley, A. Megrant, B. Burkett, R. Barends, K. Arya, B. Chiaro, Y. Chen, A. Dunsworth, A. Fowler, B. Foxen, C. Gidney, M. Giustina, R. Graff, T. Huang, E. Jeffrey, E. Lucero, J. Y. Mutus, O. Naaman, C. Neill, C. Quintana, P. Roushan, D. Sank, A. Vainsencher, J. Wenner, T. C. White, S. Boixo, R. Babbush, V. N. Smelyanskiy, H. Neven, and J. M. Martinis, "Fluctuations of Energy-Relaxation Times in Superconducting Qubits," *Phys. Rev. Lett.*, vol. 121, p. 090502, aug 2018.

[124] L. Bishop-Van Horn, Z. Cui, J. R. Kirtley, and K. A. Moler, "Cryogen-free variable temperature scanning SQUID microscope," *Rev. Sci. Instrum.*, vol. 90, p. 063705, jun 2019.

[125] A. M. Den Haan, G. H. Wijts, F. Galli, O. Usenko, G. J. Van Baarle, D. J. Van Der Zalm, and T. H. Oosterkamp, "Atomic resolution scanning tunneling microscopy in a cryogen free dilution refrigerator at 15 mK," *Rev. Sci. Instrum.*, vol. 85, p. 035112, mar 2014.

[126] M. Pelliccione, A. Sciambi, J. Bartel, A. J. Keller, and D. Goldhaber-Gordon, "Design of a scanning gate microscope for mesoscopic electron systems in a cryogen-free dilution refrigerator," *Rev. Sci. Instrum.*, vol. 84, p. 033703, mar 2013.